Durham University

Durham E-Theses

Polychromatic measurement of the wavefront for high-contrast imaging with an MKID-based Pyramid Wavefront Sensor.

MAGNIEZ, AURELIE

How to cite:

MAGNIEZ, AURELIE (2024) *Polychromatic measurement of the wavefront for high-contrast imaging with an MKID-based Pyramid Wavefront Sensor.* , Durham theses, Durham University. Available at Durham E-Theses Online: http://etheses.dur.ac.uk/15462/

Use policy

The full-text may be used and/or reproduced, and given to third parties in any format or medium, without prior permission or charge, for personal research or study, educational, or not-for-profit purposes provided that:

- a full bibliographic reference is made to the original source
- a link is made to the metadata record in Durham E-Theses
- the full-text is not changed in any way

The full-text must not be sold in any format or medium without the formal permission of the copyright holders.

Please consult the full Durham E-Theses policy for further details.

Academic Support Office, The Palatine Centre, Durham University, Stockton Road, Durham, DH1 3LE
e-mail: e-theses.admin@durham.ac.uk Tel: +44 0191 334 6107
http://etheses.dur.ac.uk

Polychromatic measurement of the wavefront for high-contrast imaging with an MKID-based Pyramid Wavefront Sensor

Aurélie Magniez

A thesis presented for the degree of

Doctor of Philosophy

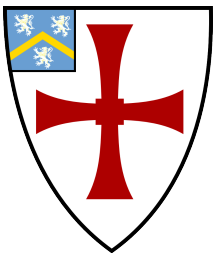

Centre for Advanced Instrumentation

The University of Durham

United Kingdom

3rd July 2024

Supervisors: Kieran O'Brien and Tim Morris

Polychromatic measurement of the wavefront for high-contrast imaging with an MKID-based Pyramid Wavefront Sensor

Aurélie Magniez

Abstract

The Pyramid Wavefront Sensor (PWFS) is widely recognised as providing the best closed-loop performance for high contrast single conjugate adaptive optics (AO) systems, with many current and future AO systems selecting the PWFS as their primary natural guide star wavefront sensor. However, it is limited by its non-linear behaviour. Existing CCD/CMOS detector technology is well suited to PWFS operation, providing near-zero read noise detectors with frame rates of 1 - 3 kHz at either visible or near-infrared wavelengths. However, there is little scope for significant improvement in these detector technologies to further enhance PWFS AO performance and address non-linearities. In this thesis, we propose the use of a microwave kinetic inductance detector (MKID) array as an alternative PWFS detector technology and describe the benefits this can bring to future AO system performance.

An MKID array is a superconducting detector with unique properties compared to CCD/CMOS detectors that provide a measure of the position, arrival time and energy of each photon incident on the array. Sorting the photons into wavebands allows us to measure the wavefront at multiple wavelengths simultaneously, providing additional information to overcome the limitations of the PWFS. In addition, photon counting becomes possible and new methods of reconstruction using temporal information can be explored.

This thesis explore modelling methods and simulation results. It addresses the complexities of modelling PWFS systems that incorporate an MKID array, analysing wavefront at multiple wavelengths simultaneously, and proposing innovative strategies to mitigate non-linearities. As MKID technology is still in the development phase, it is important to understand its potential benefits for AO to guide the future development of arrays.

ACKNOWLEDGEMENTS

I would like to thank my supervisors, Kieran and Tim, for their support throughout these years. For those many meetings, virtual and real, all those scientific exchanges. Over four years, I had the opportunity to present my work at many conferences, meet many interesting people, and learn a lot about how to be a better researcher. So thank you for giving me this opportunity.

I would also like to thank my less official supervisors Lisa and Charlotte. Lisa, thank you very much for all those hours you sat with me, patiently explaining how to simulate AO, you saved me from many despairs. Charlotte, thank you for helping me to push my knowledge and simulation to another level and I look forward to continuing our collaboration.

I would like to thank all the CfAI members, especially the PhD crew for all the discussions, lunches, and pub trips. The pandemic has made socializing difficult, but I am glad that things are still happening.

Une pensée également pour ma famille et mes amis outre-manche. Particulièrement, mes parents qui m'ont toujours supportée même s'il n'a pas été toujours facile de me laisser partir. Malgré la distance, je pense a vous tous, vous me manquez.

At last, but not least, Duncan. Throughout this PhD, there has been a lot of unexpected (a pandemic is not something I saw coming). But the most amazing surprise was to meet you. We went through lockdowns and trips, laughing and tears together. So many moments that are dear to me (including a certain hike in the lake district), the pinnacle being at the end of October. What I am trying to say is that nothing would have been the same without you, and I owe you at least my sanity (but in truth a lot more). So, thank you. Thank you for having been by my side in the last 4 years, thank you for having supported me in every meaning of the word, and I can not wait to spend the rest of my adventures with you, my very dear husband.

This works has been funded by the Science and Technology Facilities Council (grant reference: ST/S001360/1)

Contents

DECLARATION

The work in this thesis is based on research carried out at the Centre for Advanced Instrumentation, Department of Physics, University of Durham, England. No part of this thesis has been submitted elsewhere for any other degree or qualification, and it is the sole work of the author unless referenced to the contrary in the text.

Some of the work presented in this thesis has been published in journals and conference proceedings - the relevant publications are listed below.

Publications

Magniez, A., Bardou, L., Morris, T. J., O'Brien, K. MKID: an energy sensitive superconducting detector for the next generation of XAO systems. in Adaptive Optics Systems VIII (eds. Schmidt, D., Schreiber, L. , Vernet, E.) 94 (SPIE, 2022). doi:10.1117/12.2627026.

Copyright © 2023 by Aurélie Magniez.

"*The copyright of this thesis rests with the author. No quotation from it should be published without the author's prior written consent and information derived from it should be acknowledged*".

List of Figures

List of Tables

NOMENCLATURE

AO adaptive optics

DM deformable mirror

ELT extremely large telescope

EMCCD electron-multiplying charged coupled device

KL Karhunen-Loeve

NCPA non common path aberration

MEC MKID exoplanet camera

MKID Microwave Kinetic Inductance Detector

PCS Planetary Camera and Spectrograph

PSF Point Spread Function

PWFS Pyramid wavefront sensor

QE Quantum efficiency

RTC real time control system

RMS root mean square

SHWFS Shack-Hartmann wavefront sensor

SNR signal to noise ratio

WFE Wavefront error

WFS wavefront sensor

XAO eXtreme Adaptive Optics

CHAPTER 1

INTRODUCTION

1.1 Context

The exploration of exoplanets, planets beyond our Solar System, provides crucial insights into the diversity of planetary systems in the Universe. Direct imaging is a technique used for detecting exoplanets, allowing for their direct observation in orbit around host stars (Seager and Dotson, 2010). This technique also enables the measurement of exoplanet spectra.

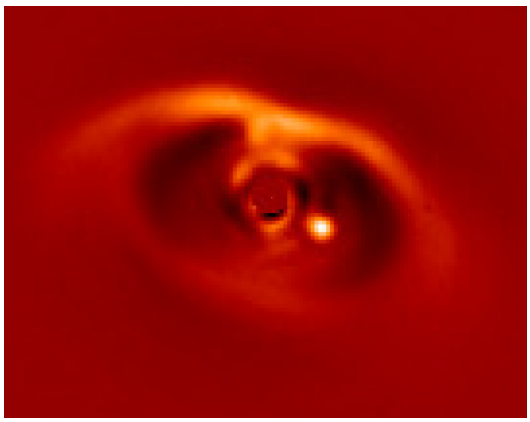

Figure 1.1: Image showing the planet inside the gap of the disk around PDS 70 taken with IRDIS (sub-system of VLT/SPHERE). From Müller et al. (2018).

Direct imaging offers advantages over other detection techniques by allowing astronomers to study the atmospheres, compositions, and physical characteristics of exoplanets more directly through the spectra. Direct imaging provides a clearer understanding of the individual properties of exoplanets, unlike indirect methods that

derive the presence of exoplanets from radial velocity. Instruments like SPHERE on the Very Large Telescope are capable of producing remarkable images of exoplanets and protoplanetary disks, as demonstrated in Figure 1.1.

When directly imaging exoplanets, two main challenges are encountered: angular resolution and distinguishing the host star from the planet. To increase angular resolution, it is necessary to build larger telescopes. An example is the ELT, a 39-metre-diameter telescope in the Atacama Desert in Chile (see Figure 1.2).

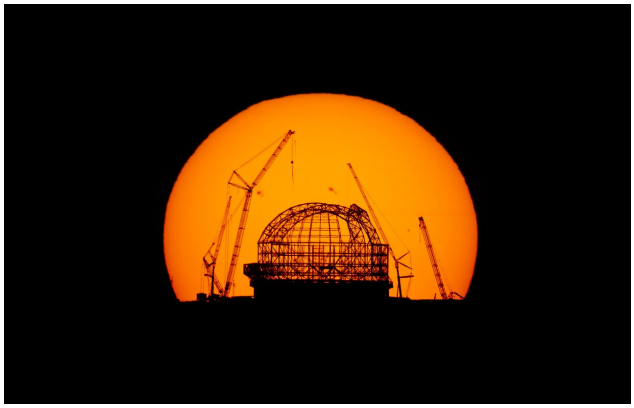

Figure 1.2: Construction of the ELT, photo released 4$^{\text{th}}$ September 2023. Credit: E. Garcés/ESO.

The ELT introduces new instruments, including the Planetary Camera and Spectrograph (PCS), designed for exoplanet imaging and spectroscopy. Figure 1.3 shows the expected targets for this instrument, which will require improved angular resolution and contrast compared to existing capabilities such as those of SPHERE (Beuzit et al., 2019).

However, ground-based telescopes face challenges from atmospheric perturbations degrading imaging performance. To achieve high contrast imaging at high angular resolution, ELT instruments require the best possible performance of adaptive optics. Adaptive optics is a technique used to compensate for atmospheric perturbations by inserting an adaptive element, usually a deformable mirror, into the optical path. This adapting element compensates for wavefront deformations and improves image quality. This is achieved by using a wavefront sensor (WFS), which measures the atmospheric perturbations and tracks them over time.

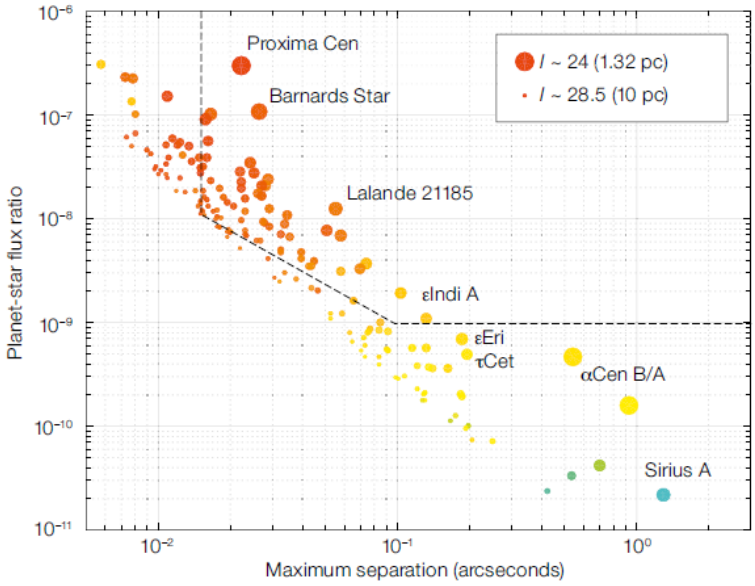

Figure 1.3: Angular separation and I-band flux ratio between hypothetical exoearths (Earth-size and insolation, one per star) and parent stars within 10 pc (from the Hipparcos catalogue) observable from Cerro Armazones. The symbol size indicates the planet's apparent brightness, and the colours indicate the stellar spectral type (red: M-stars, yellow: solar-type stars). The dotted lines indicate the approximate contrast boundaries for PCS. From Kasper et al. (2021).

1.2 Concept: Hyperspectral Pyramid Wavefront Sensor

The Pyramid Wavefront Sensor (PWFS) (Ragazzoni, 1996) is widely recognised as providing the best closed-loop performance for high-contrast single conjugate adaptive optics (AO) systems, with many current and future AO systems selecting the PWFS as their primary natural guide star wavefront sensor (Esposito et al., 2010; Vidal et al., 2022; Schwartz et al., 2020). However, it is limited by its non-linear behaviour (Korkiakoski et al., 2008; Ragazzoni et al., 2002). The non-linearities of the wavefront sensors reduce their sensitivity, resulting in a decrease in performance. Existing CCD/CMOS detector technology is well suited to PWFS operation, providing near-zero read noise detectors with frame rates of 1 - 3 kHz at either visible or near-infrared wavelengths. However, there is little scope for significant improvement in these detector technologies to further enhance PWFS AO perform-

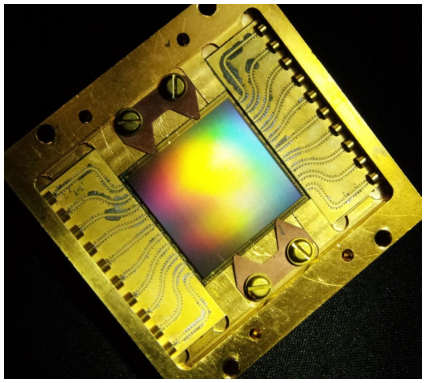

Figure 1.4: Image of a 20,440 pixel PtSi MKID device designed for MEC. From Walter et al. (2020)

ance and address non-linearities. In this thesis, we propose and investigate the use of a microwave kinetic inductance detector (MKID) (Day et al., 2003) array, shown in Figure 1.4, as an alternative PWFS detector technology.

An MKID array is a superconducting detector with unique properties compared to CCD/CMOS detectors that provide a measure of the position, arrival time and energy of each photon incident on the array. Sorting the photons into wavebands allows us to measure the wavefront at multiple wavelengths simultaneously, providing additional information to overcome the limitations of the PWFS. In addition, photon counting becomes possible and new methods of reconstruction using temporal information can be explored. The manufacturing of MKID is flexible, allowing the user to enforce some of its different properties such as speed, energy measurement accuracy or the shape of the array according to the requirements.

The AO community has yet to extensively explore the temporal and chromatic aspects of MKID arrays. This study focuses solely on the chromatic aspect, leaving the temporal aspect for future research. A multitude of factors influence the selection of a wavefront sensing wavelength. In terms of AO performance, there is a trade-off between enhanced signal-to-noise ratio (favouring shorter wavelengths) and enhanced robustness to non-linearities (favouring longer wavelengths). A hyperspectral PWFS provides information about the chromatic dependence of the wavefront measurement, which can be employed to enhance the correction. This

could permit, for instance, the direct measurement and compensation of non-linearities at short wavelengths, capitalising on the higher signal-to-noise ratio that is possible on astronomical targets in the visible spectrum. Finally, the PWFS is subject to chromatic dispersion at the pupil plane due to the presence of a glass prism constraining the sensed waveband. The use of a hyperspectral wavefront sensor would therefore expand the overall sensed waveband by compensating for this dispersion.

To our knowledge, only two AO systems, using two PWFS each, are designed to measure atmospheric perturbations at different wavelengths. By measuring the wavefront at multiple wavelength, AO systems add flexibility to their systems, whether it is about the science case or increase the sensitivity of the wavefront sensor. However, even these systems are limited to only two wavelengths.

Morzinski et al. (2020) presented a system for measuring atmospheric perturbations at a specific wavelength, or between two wavelengths, depending on the observation conditions. Pinna et al. (2014) demonstrate a method for measuring atmospheric perturbations at two different wavelengths together, but with different sampling frequencies, one of which is dedicated to measuring the average of the phase profile over the telescope pupil of the incoming light (or piston). However, simultaneous measurements of atmospheric perturbations at different wavelengths, or hyperspectral wavefront sensing, have not yet been investigated.

It is possible to design a hyperspectral wavefront sensor without an energy-sensitive detector. However, the complexity required for such a system would make it difficult to set up and limit the number of chromatic measurements. The use of an MKID array enables the accumulation of advantages provided by a polychromatic measurement with a PWFS.

As the MKID technology is still in development, it is imperative to fully understand the potential benefits for AO and provide technical requirements that can inform and guide device development. Limitations, such as the saturation effect observed

on an MKID is a concern when observing a bright star. The other aspect to look at is the energy resolution defining how finely photons can be sorted into wavebands. The exploitation of the wavelength information provided by MKID requires a detailed characterisation of its effect on the behaviour of the PWFS. Moreover, it is crucial to identify the aspects of the PWFS that can be improved through the integration of MKID technology. These studies aim to address two pivotal questions, steering the advancement of MKID for AO development:

- How can we use an MKID to improve the performance of the PWFS and address its non-linearities?
- What are the requirements for future MKID arrays to achieve these performance levels over existing detectors?

1.3 Summary

Chapter 2 of this thesis provides the necessary background to understand the concepts used throughout this research. It covers image formation in a telescope and the impact of atmospheric perturbations on imaging quality. It then delves into the AO system, explaining the mechanisms that lead to compensation for atmospheric perturbations. Finally, it describes the two key elements of this concept: PWFS and MKIDs.

To answer the two questions, the first step is to model the MKID-based PWFS system described in Chapter 3. We achieve this by adapting two existing monochromatic PWFS models to enable a polychromatic measurement of simulated atmospheric perturbations. These models are then integrated into an AO end-to-end simulation, and the performance of the wavefront sensor is analysed. In addition, we look at how to measure a major source of non-linearity in the PWFS: optical gain, using a previously tested approach to study those gains.

In Chapter 4, we use these models to study the influence of wavelength on the behaviour of the PWFS in order to understand where the use of an MKID might be most efficient. For each behaviour studied, we begin by comparing monochromatic cases, examining three aspects: measurement saturation, optical gains, and photon noise. This analysis allows us to identify the most suitable wavelength for the observation conditions, as well as the various trade-offs that limit PWFS performance. And is completed with a discussion on the integration of an MKID array in an XAO system with a particular focus on the photon flux and the potential saturation of the detector, as well as the photon distribution.

Chapter 5 introduces a method to mitigate the optical gains issue that affects the performance of the PWFS. This approach exploits the chromatic dimension introduced by an energy-sensitive detector in the measurement of the wavefront sensor. While existing methods exist to address this problem, they often require additional hardware, resulting in signal loss or requiring supplementary operations during on-sky observations. In contrast, the proposed approach not only tracks PWFS nonlinearities directly within the measurements but also offers unprecedented speed in tracking atmospheric conditions. This aspect has remained relatively unexplored due to the current limitations of existing techniques.

In Chapter 6, we summarize the key results and findings from this research and highlight several future research and development directions.

CHAPTER 2

ADAPTIVE OPTICS FOR GROUND TELESCOPES

To understand the benefits of integrating an MKID-based PWFS into an adaptive optics (AO) system, it is necessary to first understand how telescopes benefit from adaptive optics (AO) systems.

This chapter begins by describing image formation in a telescope and how atmospheric turbulence degrades ground-based telescope imaging. We then explain how adaptive optics systems work and how their components interact to reconstruct the wavefront. As a key component of the AO system, we then introduce the wavefront sensor (WFS) studied in this work: the pyramid wavefront sensor. Finally, we present MKIDs and their current and potential performance as AO detectors.

2.1 Telescope imaging and atmospheric turbulence

Astronomical observations from the ground are degraded by atmospheric turbulence. To comprehend the necessity of adaptive optics, it is important to first understand the effects of atmospheric perturbations on the behaviour of light in a telescope without wavefront correction. This section describes the impact of atmospheric perturbations on the behaviour of light in a telescope.

2.1.1 Angular resolution

When a telescope collects photons, diffraction is introduced by the surface that limits the entrance, called the pupil. The PSF is the impulse response (the image of a point) of an instrument and depends on the shape of the pupil. Specifically, it is the squared modulus of the Fourier transform $\mathcal{F}$ of the binary function $\mathbb{I}_p$, which determines whether a point is inside or outside the pupil.

$$\mathbb{I}_p(x,y) = \begin{cases} 1 & \text{in the pupil} \\ 0 & \text{outside the pupil} \end{cases} \tag{2.1}$$

and

$$\text{PSF}(x',y') = |\mathcal{F}(\mathbb{I}_p(x,y))^2|, \tag{2.2}$$

where (x,y) are the coordinates in the pupil plane of the telescope and (x',y') are the coordinates in the focal plane of the telescope.

The pupil shape for telescopes is typically defined by the primary mirror and its shape can be characterised by a disc of diameter D. The central area is frequently obscured by the secondary mirror, which is held in place by spiders. Consequently, the pupil shape of a telescope often exhibits a secondary obturation and some arms. If these features are not taken into account, the PSF is then an Airy disc, shown Figure 2.1(a), whose first minimum is produced on a circle of angular radius:

$$\theta_{Airy} \approx 1.22 \times \frac{\lambda}{D} \tag{2.3}$$

where λ is the wavelength of observation.

The image I_O of an object O is the convolution with the PSF:

$$I_O = \text{PSF} \star O \tag{2.4}$$

where $\star$ is the convolution product.

Angular resolution is defined as the distance between two point sources such that the maximum values of their corresponding PSFs fall within the first cancellation of each other, i.e. θ_{Airy}. The angular resolution of the telescope is limited only by its size. However, in reality, for a ground-based telescope, the atmosphere distorts the PSF and the resulting angular resolution is much lower.

2.1.2 Atmospheric turbulence and statistic

The properties of turbulence described here are detailed in the review by Roddier (1999), which summarises the work done on turbulence, in particular by Kolmogorov (1941) for its statistical properties and Tatarskii (1971) for the implications for wave propagation. In this introduction, I present only those properties that are relevant to the understanding of the rest of the work.

From the point of view of the astronomer, atmospheric turbulence causes a local and random fluctuation in the refractive index of air n. Studies of the statistical properties of turbulence (Kolmogorov, 1941) led to the expression of the three-dimensional spectral density of index fluctuations, known as the Kolmogorov spectrum:

$$\mathcal{W}(\vec{f}) = 0.33(2\pi)^{-2/3} \times C_N^2 \times f^{-11/3}, \tag{2.5}$$

where f is the norm of the spatial frequency vector $\vec{f}$. This spectrum can be used to write the refractive index structure function D_n, which gives the variance of the index difference between a point in space $\boldsymbol{r}$ and a neighbouring point $\boldsymbol{r} + \boldsymbol{\rho}$.

$$D_n(\boldsymbol{\rho}) = \left\langle |n(\boldsymbol{r}) - n(\boldsymbol{r} + \boldsymbol{\rho})|^2 \right\rangle = C_N^2 \rho^{2/3}, \tag{2.6}$$

where $\langle . \rangle$ denotes an average. The refractive index structure constant, C_N^2, characterises the strength of the turbulence. A higher value of C_N^2 indicates a greater variance of the refractive index between two nearby points. This equation is valid

when the turbulence is between two scales l_0 and L_0, called the inner and outer scales of turbulence, of the order of centimetres and tens of metres respectively (Roddier, 1981; Ziad et al., 2004) .

To understand the effect of refractive index variations on telescope imaging, we need to consider the behaviour of light. Light can be described as a wave, with the electromagnetic field represented by the symbol Ψ. Ψ is defined by its amplitude, $\boldsymbol{A}$, and its phase, ϕ.

$$\Psi = \boldsymbol{A}e^{i\phi} \tag{2.7}$$

The wavefront is the surface where all points have the same phase. When a wave is emitted by an astronomical object, the wavefront arriving near Earth is flat due to the distant source. However, as the light passes through the atmosphere, fluctuations in the refractive index cause relative delays or advances in the propagated wavefront, which depend on the path taken through the atmosphere. At the telescope, the wavefront can be expressed as an optical path difference δ to give its deviation from a plane wavefront. The optical path difference is related to the phase as follows:

$$\phi = \frac{2\pi}{\lambda}\delta. \tag{2.8}$$

From Equation 2.6, the refractive index structure function can be used to derive the phase structure function to describe the statistical properties of the phase:

$$D_\phi(\boldsymbol{\rho}) = \left\langle |\phi(\boldsymbol{r}) - \phi(\boldsymbol{r}+\boldsymbol{\rho})|^2 \right\rangle = 6.88 \times \left(\frac{\rho}{r_0}\right)^{2/3}, \tag{2.9}$$

where r_0 is the Fried parameter defined as (Fried, 1966):

$$r_0 = \left[0.423\left(\frac{2\pi}{\lambda}\right)(\cos\zeta)^{-1}\int C_N^2(h)dh\right]^{-3/5} \tag{2.10}$$

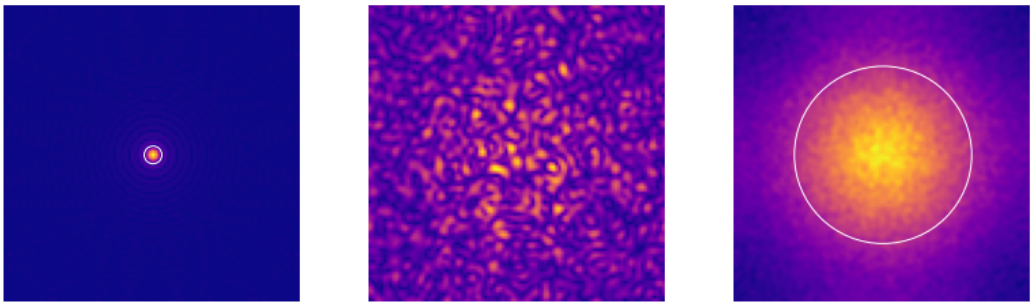

(a) PSF of a perfect telescope unaffected by atmospheric turbulence.

(b) Simulated PSF perturbed over a short exposure time

(c) Long exposure PSF, average of 500 short exposures.

Figure 2.1: Simulated PSF for different conditions. The white circles represent on the left panel (λ/D) and on the right panel (λ/r_0).

which depends on the zenith angle ζ and the turbulence strength for different altitudes h. r_0 is defined as the equivalent diameter of the telescope for the same angular resolution. More specifically, r_0 is defined as the diameter of a pupil within which the root mean square (RMS) phase error is approximately 1 rad for a given wavelength (Fried, 1965; Noll, 1976). Thus, small values of r_0 correspond to stronger turbulence. Equation 2.10 shows that r_0 is wavelength dependent. r0 is typically defined at 500 nm.

Considering atmospheric turbulence, the expression for the PSF of the telescope then becomes :

$$\mathrm{PSF}(x', y') = |\mathcal{F}(\mathbb{I}_p(x, y) \times \Psi(x, y))^2| \tag{2.11}$$

As the wavefront is no longer flat, the light rays deviate from their trajectory and interfere with each other, resulting in speckles in the instantaneous PSF, as illustrated in Figure 2.1(b). These speckles fluctuate over time and when averaged, such as during a long exposure, they result in a spot with a width of λ/r_0, as illustrated in Figure 2.1(c). The strength of turbulence is commonly characterised by the parameter r_0, where larger values indicate weaker turbulence. By taking a long exposure image, we converge on a new image spot with a characteristic angular size called seeing denoted θ_s, see Figure 2.1(c), which is much larger than the PSF

due to the diffraction of the telescope and is synonymous with a loss of part of the resolving power of the telescope. The seeing is related to Fried's parameter :

$$\theta_s \propto \frac{\lambda}{r_0} \tag{2.12}$$

The role of adaptive optics (AO) is therefore to correct the turbulence to bring the resolution of the telescope closer to the diffracted limited angular resolution.

2.1.3 Phase modal decomposition

To investigate the wavefront at the aperture of a telescope and to address various analytical and numerical challenges in adaptive optics, it is advantageous to use a modal decomposition of the wavefront. The phase ϕ of the electromagnetic field Ψ_p within the entrance pupil is contained in a vector space whose dimension depends on the number of points in the pupil that facilitate the phase description. Similar to any vector space, it is possible to establish bases that can describe any specific phase. An orthonormal basis, consisting of modes ϕ_μ, is defined, which allows for the decomposition of a phase ϕ onto the ϕ_μ basis :

$$\phi = \sum_{\mu=1}^{\infty} c_\mu \phi_\mu \tag{2.13}$$

with c_μ the coefficients of the modal decomposition.

A carefully selected basis facilitates rapid convergence for typical wavefronts and efficient representation of the wavefront, enabling the use of a finite number of modes. An orthonormal basis can also define the variance of the phase ϕ, expressed as

$$\sigma_\phi^2 = \sum_{\mu=1}^{\infty} c_\mu^2 \tag{2.14}$$

This section describes two notable orthonormal bases: the Zernike polynomial base and the atmospheric KL base.

2.1.3.1 Zernike

Zernike polynomials form an orthonormal basis on a disc of unit radius proposed by Zernike (1934). They are expressed in polar coordinates as follows:

$$Z_n^m(r,\theta) = \sqrt{n+1} \times R_n^m(r) \times \begin{cases} \sqrt{2}\cos(m\theta) \\ \sqrt{2}\sin(m\theta) \\ 1 \qquad\qquad \text{if } m = 0 \end{cases} \tag{2.15}$$

with

$$R_n^m(r) = \sum_{s=0}^{(\eta-m)/2} \frac{(-1)^s (n-s)!}{s![(\eta+m)/2-s]![(\eta-m)/2-s]!} \tag{2.16}$$

where r is the radial coordinate, which has a value between 0 and 1, and θ is the angular coordinate, which has a value between 0 and 2π.

The indices η correspond to radial orders and m to azimuthal orders. m and η are integers such that $m \leq \eta$ and $(\eta - |m|)$ is even. Equation 2.15 shows that when $m \neq 0$ there are two polynomials corresponding to each pair of indices m and η: one with a cosine term and the other with a sine term. To differentiate between them, some conventions denote polynomials containing sine as $-m$. Figure 2.2 displays the first 14 polynomials. All of these modes are defined to have a mean of zero, except for the Z_0^0 mode which represents the piston mode. It is important to note that as the radial order increases, Zernike polynomials contain higher spatial frequencies.

However, there are some drawbacks associated with the use of this basis. For instance, in the case of non-perfectly circular and complete pupils (central obstructions, large spiders, etc.) this basis is no longer orthonormal. Additionally, higher-order radial modes quickly exhibit a power concentration at the edges of the pupil because $R_\eta^m(\theta = 1) = 1$, for any m and η. Throughout this thesis, we therefore use another basis that is better suited for our system.

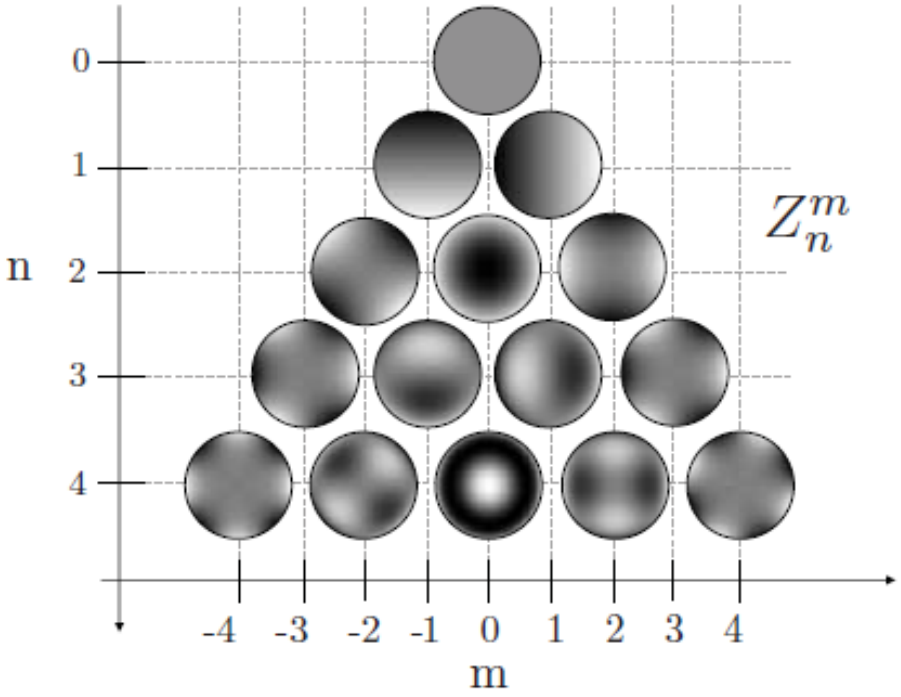

Figure 2.2: Representation of the first 14 Zernike polynomials. The radial degrees n and azimuthal degrees m are given on the edges of the figure, and the sign - denotes polynomials containing a sine in the equation 2.15. Credit: Chambouleyron (2021)

2.1.3.2 Karhunen-Loeve (KL)

The KL basis is a type of basis that overcomes the limitations of the Zernike polynomial basis mentioned previously. It is constructed from the spatial covariance matrix of the turbulent phase in the telescope pupil. The covariance matrix is calculated for two points $\boldsymbol{r}$ and $\boldsymbol{r'}$ in the phase as follows:

$$\mathrm{Cov}(\boldsymbol{r}, \boldsymbol{r'}) = \langle \mathbb{I}_p(\boldsymbol{r})\phi(\boldsymbol{r})\mathbb{I}_p(\boldsymbol{r'})\phi(\boldsymbol{r'})\rangle \tag{2.17}$$

The basis for the KL mode is constructed by calculating the eigenmodes of this matrix. Additionally, this basis is orthonormal for the pupil considered and has a smoothed power at the edges. Finally, this basis is better ordered in terms of frequency, making it a preferred choice for the developments that follow. The main disadvantage of this basis is that it cannot be expressed analytically because it

depends on the shape of the pupil.

2.2 Adaptive optics

The principle of AO was developed in the 1950s to compensate for atmospheric perturbations and improve the angular resolution of ground-based telescopes (Babcock, 1953). Currently, 8-metre class telescopes are equipped with AO systems (Sauvage et al., 2016; Plantet et al., 2018), and the next generation of extremely large telescopes is developing such systems (Bonnet et al., 2018).

This section describes adaptive optics and lists the necessary concepts to understand the rest of this work.

2.2.1 AO loop

As previously stated, the purpose of an adaptive optics system is to correct for atmospheric turbulence and restore the angular resolution of the telescope. This is accomplished through the use of three essential components.

$$\phi_{atm} + \phi_{DM} = 0 \tag{2.18}$$

Wavefront sensor: The WFS is a sensor that measure the phase aberration. The two most common sensors are the Shack-Hartmann wavefront sensor (SHWFS) (Platt and Shack, 2001) and the PWFS (Ragazzoni, 1996). As the PWFS is at the core of this thesis and will be detailed in the next section.

Real time control system: The real time control system (RTC) computes the commands to send to the deformable mirror (DM) based on the measurement obtained from the WFS to adjust its shape according to the new input wavefront measurement.

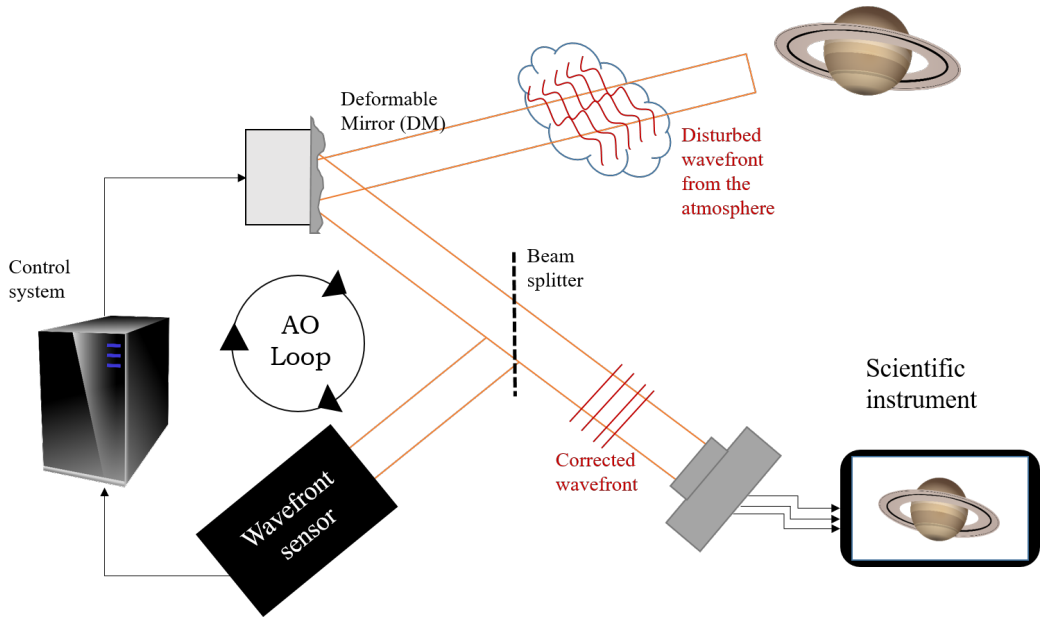

Figure 2.3: Diagram of the AO loop.

The diagram in Figure 2.3 illustrates how these different systems interact: the light entering the telescope reaches the DM and is then split into two beams. One beam is for the sciences, where the instrument for astrophysical measurements is located. The second beam is sent into the AO loop. In this route, the light from a guide star is analysed by the WFS to obtain the phase at the entrance pupil of the telescope to control the DM. In order to obtain accurate measurements, the WFS needs a certain number of photons. Therefore, the guide star must have adequate luminosity, and it is essential to optimize the number of photons detected in the AO loop. As shown in Figure 2.3, the WFS is positioned after the DM and sees the residual phases, i.e. the turbulent phases corrected by the DM. In this manner, the AO system operates in a closed loop.

2.2.2 Wavefront reconstruction

Wavefront reconstruction is the process of using the measurements taken by the wavefront sensor and converting them into commands for the DM to update its shape. This process consists of two phases: the calibration phase, which saves the WFS response of given wavefront shapes, and the operation phase, during which

the AO loop is closed to correct for atmospheric aberration over time.

2.2.2.1 Calibration phase

The calibration phase of the WFS consists in the generation of an interaction matrix, which is the translation matrix between the signal extracted from the WFS and the DM basis. The DM basis consists of a series of shapes or modes that the DM can adopt, depending on the number of actuators. It is a decomposition of the DM phase screen ϕ_{DM} analogous to the modal decomposition presented in section 2.1.3. The calibration phase thus consists of collecting the WFS response for each mode ϕ_μ applied to the DM without any atmospheric perturbation. The interaction matrix $\mathcal{IM}$ is an N×M matrix where N is the number of WFS measurements and M the number of modes that the DM can produce. $\mathcal{IM}$ is defined as

$$\mathcal{IM} = \begin{pmatrix} \vec{s}(\phi_0) \\ \vdots \\ \vec{s}(\phi_\mu) \\ \vdots \\ \vec{s}(\phi_M) \end{pmatrix} \tag{2.19}$$

where $\vec{s}(\phi_\mu)$ is the signal of the WFS when the mode ϕ_μ is applied to the DM.

We consider $\vec{c}(\phi)$ to be the vector of coefficients (c_μ from equation 2.13) applied to the modal basis to form the phase screen shape ϕ. The RTC computes this vector to obtain ϕ_{DM} during operation. During calibration, the value of $\vec{c}(\phi)$ is given and $\vec{s}(\phi)$ is measured. During operation, $\vec{s}(\phi)$ is measured to calculate $\vec{c}(\phi)$. The final result of the calibration is a matrix that performs the inverse of the interaction matrix, known as the control matrix $\mathcal{CM}$. $\mathcal{CM}$ is the pseudo-inverse of $\mathcal{IM}$ and is typically computed using the Moore-Penrose algorithm (Penrose, 1956), denoted †, and defined as

$$\mathcal{CM} = \mathcal{IM}^{\dagger} \tag{2.20}$$

and

$$\vec{c}(\phi) = \vec{s}(\phi) \times \mathcal{CM} \tag{2.21}$$

2.2.2.2 Operation phase

During operation, the wavefront is reconstructed using the equation 2.21. As we are in a closed loop, the command sent to the DM is computed using the following integrator :

$$\vec{c}(\phi_{DM})[i] = \vec{c}(\phi_{DM})[i-1] + g \times \vec{c}(\phi_{atm})[i] \tag{2.22}$$

where $\vec{c}(\phi_{DM})$ is the vector of coefficient, or command, sent to the DM and $\vec{c}(\phi_{atm})$ is the vector of coefficient calculated from the measure of ϕ_{atm} by the WFS. g is the loop gain and has a direct impact on the AO loop temporal behaviour. A small g corresponds to a slow loop and may struggle to keep up with the evolution of atmospheric perturbations. However, if g is too large, the effect of noise on the loop increases. It is important to note that there are many other reconstructors available as well. Kulcsár et al. (2006) provide an example of a reconstructor that can enhance performance by taking temporal aspects into account. But since the temporal behaviour is not the focus of the work presented here, it has not been further analysed.

2.2.3 Performance metrics

When running an AO system, it is important to be able to evaluate its performance. We present here two metrics that are commonly used in the AO community.

2.2.3.1 Wavefront error (WFE)

We define the residual phase screen by

$$\phi_{res} = \phi_{atm} + \phi_{DM} \tag{2.23}$$

By quantifying the aberration in the residual phase screen, we can determine the image quality in the focal plane. This metric, the residual wavefront error σ_ϕ, is usually defined as the RMS variance of ϕ_{res} averaged over the aperture.

$$\sigma_\phi = \sqrt{\langle(\phi_{res} - \langle\phi_{res}\rangle)^2\rangle} \tag{2.24}$$

where $\langle . \rangle$ denotes an average, in this case over a time period. The mean of the phase is subtracted as it does impact the image quality. The commonly used unit for wavefront error is nm RMS. The flatter the wavefront, the smaller the WFE, and the better the image quality.

2.2.3.2 Strehl Ratio

The Strehl ratio quantifies the difference between a PSF with atmospheric perturbation and the PSF limited by diffraction. It is calculated as the ratio between the peak intensity of the perturbed PSF and the diffraction-limited PSF.

$$SR = \frac{PSF_{atm}(\theta = 0)}{PSF_{Airy}(\theta = 0)} \tag{2.25}$$

The correction performance is best when $SR = 1$.

The Strehl ratio may be related to the wavefront error by the Mahajan formula (Mahajan, 1982), for small wavefront error:

$$SR = \exp(-\sigma_\phi^2) \tag{2.26}$$

2.2.4 Error budget

There are several sources of error in an AO system. To characterise them, an error budget is made. It consists of a decomposition of the WFE into several independent error terms which are added quadratically to determine σ_ϕ^2.

$$\sigma_\phi^2 = \sum_{error sources}^{\varepsilon} \sigma_\varepsilon^2 \tag{2.27}$$

where ε denotes the error type. In this section, a list of the main components and their origins is presented.

2.2.4.1 Aliasing error

The aliasing error $\sigma_{aliasing}^2$ is due to the high spatial frequencies that cannot be correctly measured by the wavefront analyzer are interpreted as low spatial frequencies by the phenomenon known as aliasing. These false low frequencies are then injected into the system during phase reconstruction by the DM. However, the error term of aliasing has a small contribution to σ_ϕ^2 compared to the rest of the error terms (Agapito and Pinna, 2019).

2.2.4.2 Temporal error

The temporal error $\sigma_{temporal}^2$ is linked both to the loop rate and to the time delay with which the correction is applied to the DM for a wavefront measurement. This error is therefore intrinsically linked to the RTC's performance and the control laws chosen, but also to the observation conditions via the wind speed (Gendron and Lena, 1994).

2.2.4.3 Fitting error

The fitting error $\sigma^2_{fitting}$ is the result of the limited spatial resolution of the deformable mirror. Any wavefront can be projected as two components: onto the modes controlled by the DM, ϕ_{DM} and onto its orthogonal space, $\phi_{\perp DM}$:

$$\phi = \phi_{DM} + \phi_{\perp DM}, \tag{2.28}$$

where $\phi_{\perp DM}$ contains all the spatial frequencies, or modes, higher than the ones contained by the modal basis ofDM. The corrective effect of DM is always restricted to the ϕ_{DM} component alone and all spatial frequencies above this limit will not be corrected by the AO loop.

2.2.4.4 Noise error

The measurement of the wavefront by the WFS is subject to random variations in addition to the expected signal. This noise is considered to have two origins. Firstly, the nature of photons induces a Poisson distribution on the number of photons arriving in a surface element over a certain period. Secondly, most detectors have Gaussian electronic noise on the measurement of the value of each pixel (known as read-out noise). However, the properties of MKID mean that the readout noise is null. For the rest of the thesis, we will therefore have:

$$\sigma^2_{noise} = \sigma^2_{photon} \tag{2.29}$$

2.2.4.5 Non-common path aberrations

In a telescope equipped with an AO system, the light path is divided into two paths: the AO loop path and the science path. The wavefront measured by the AO loop is received from the beamsplitter. However, there are typically optics between the beamsplitter and the scientific instrument that introduce aberrations not detected

by the wavefront sensor (WFS). The non common path aberration (NCPA) are defined as:

$$\phi_{NCPA} = \phi_{res} - \phi_{sci} \tag{2.30}$$

where ϕ_{sci} is the wavefront phase screen seen by the scientific instrument.

These aberrations are static or quasi-static in time and can fluctuate with temperature, long-term mechanical deformation, or the position of moving optics. Once NCPA have been calibrated, usually using phase diversity techniques (Gonsalves, 1982), the loop control is modified so that ϕ_{res} tends to ϕ_{NCPA}. However, imperfect characterisation or a component orthogonal to the DM space in NCPA can add error term ϕ_{NCPA} to our error budget.

2.2.5 eXtreme Adaptive Optics (XAO) and Exoplanet imaging

All the numbers and statements in this section are sourced from (Guyon, 2018).

Detecting exoplanets directly is a complex task due to two main difficulties:

- The angular distances between stars and their planets are very small, requiring a telescope with high separating power. To increase the angular resolution, larger telescopes are built.
- The contrast between the luminosity of the star and that of the planet is extremely low, typically in the order of 10^{-4} to 10^{-10}. Even observations at high angular resolutions are unable to separate the signal of the planet from the photon noise of its host star.

To improve the later point, we need better AO coupled with the use of coronographs to mask the host star signals. Any residual phase affects the focal plane and greatly reduces the contrast between the planet and the star. XAO systems are used to achieve the required performance.

AO systems can be classified into different types. The AO configuration presented in this section, with one DM, one WFS and one guide star is known as *single conjugate adaptive optics (SCAO)*. XAO is an AO system with an SCAO configuration but with performance pushed to its limits. An XAO system has a minimum frame rate of 1 kHz and typically corrects >1000 aberration modes achieving Strehl ratios of about 0.9. From the error budget shown in equation 2.27, it is possible to identify the technological barriers to the ultimate performance of XAO systems. Fitting, aliasing, and temporal errors are driven by technological limitations that directly impact the performance of the AO system when overcome.

Due to its high sensitivity, the pyramid wavefront sensor (PWFS) is often chosen for XAO systems (Vidal et al., 2022; Ahn et al., 2021).

2.3 Pyramid wavefront sensor

First proposed in 1996 by R. Ragazzoni (Ragazzoni, 1996), the PWFS has already demonstrated impressive performance Esposito et al. (2010). We describe in this section its principal components and its principle of operation. We also discuss its limitations.

2.3.1 Principle of operation

The Pyramid wavefront sensor (PWFS) is a WFS belonging to the category of the Fourier-type WFS (Fauvarque et al., 2016). This means it has an optical element, here a pyramidal prism, that acts on the PSF in the focal plane and the signal extracted is from an image plane. Practically, we can describe the PWFS in three components shown in Figure 2.4

- An incoming perturbated wavefront going through a pupil and is focused by a lens at the top of a pyramidal prism

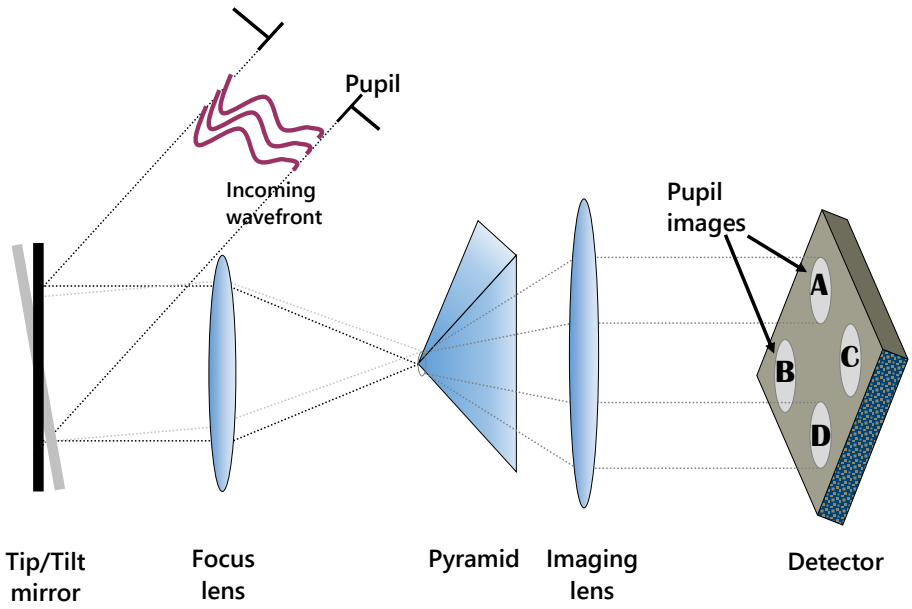

Figure 2.4: Scheme of the optical setup of a PWFS. The circular modulation path is shown in the dashed line.

- The prism, made up of 4 faces, divides the beam into 4 beams. It is to be noted that the number of faces has no real impact on the performance (Fauvarque et al., 2017). However, since 4-face prisms are the most widely used, this number will be used as a standard.

- A relay lens then collimates the beams to form four pupil images on the detector surface. The concept of this thesis is to use an MKID array as PWFS detector here.

The WFS signal extracted from the WFS is the intensity gradient between the pixels in the same location in the four pupil images. This signal is proportional to the phase gradient at that location and is commonly referred to as slope vector (or slopes), noted $\vec{s}$, see Equation 2.19. It is obtained by calculating the gradient along the x and y axes for each pixel and measuring the tilt value of the wavefront on that pixel. The definition of the slope vector ($\vec{s} = [\vec{s}_x, \vec{s}_y]$) had been introduced

by Ragazzoni (1996).

$$\vec{s}_x = \sum_{p}^{pupil} \frac{(I_p^A + I_p^C) - (I_p^B + I_p^D)}{I_p^A + I_p^B + I_p^C + I_p^D} \tag{2.31}$$

$$\vec{s}_y = \sum_{p}^{pupil} \frac{(I_p^A + I_p^B) - (I_p^C + I_p^D)}{I_p^A + I_p^B + I_p^C + I_p^D} \tag{2.32}$$

where $I_p^{A,B,C,D}$ are the intensities of the pixels on the detector planes as illustrated figure 2.5 and p denotes an individual pixel in the detector array.

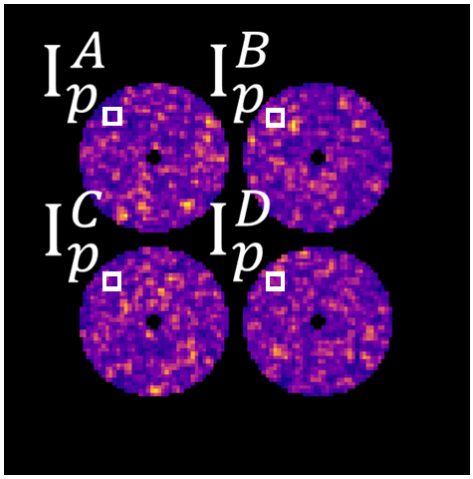

Figure 2.5: Simulated example of a PWFS detector plane. $I_p^{A,B,C,D}$ are the intensities of a pixel on the pupil imaging corresponding to the same pixel in the pupil plane

2.3.2 Limits of the PWFS and existing solutions

The PWFS is interesting for astronomers due to its high sensitivity. However, it is limited by various non-linear behaviours such as measurement saturation and optical gain, as well as physical limits such as chromatic dispersion.

2.3.2.1 Sensitivity / dynamic range and modulation

The high sensitivity of the PWFS comes at the expense of its dynamic range. Figure 2.6 illustrates this phenomenon. The top two rows of the figure show that the tip-

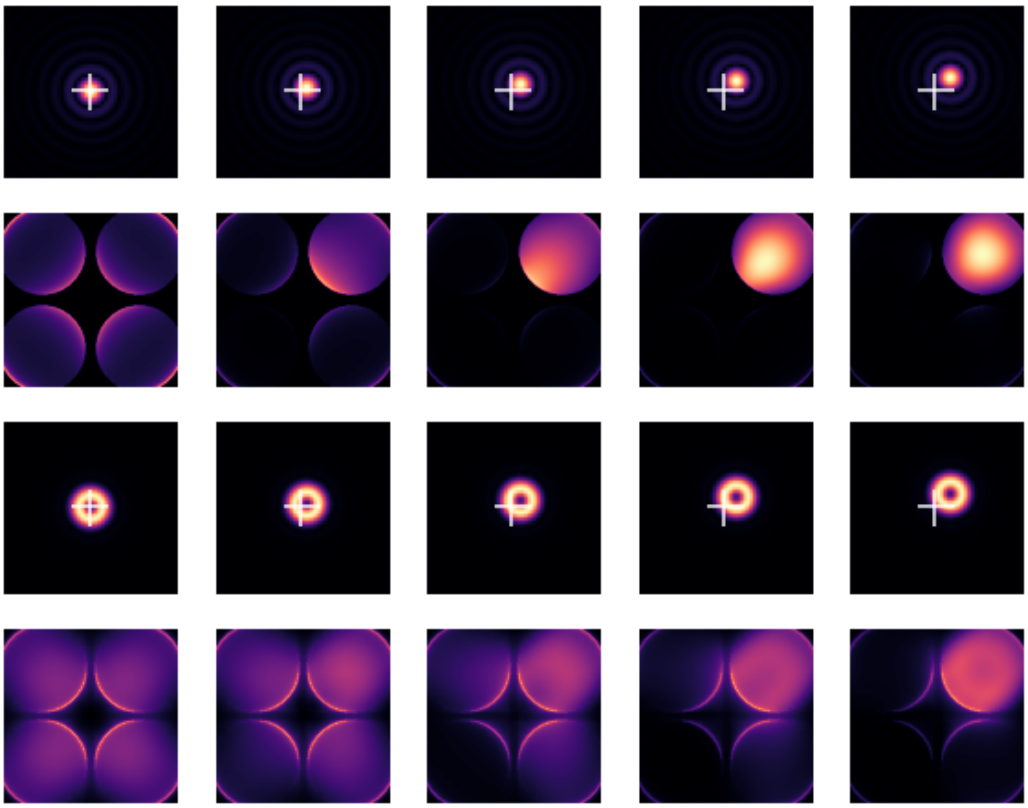

Figure 2.6: Simulated focal planes (row 1 and 3) and detector planes (row 2 and 4) of a PWFS with increasing tip-tilt aberration with modulation of the PSF (row 3 and 4) and without modulation (row 1 and 2). Each column has the same amplitude of aberration. The cross in the focal plane images represents the tip of the pyramid.

tilt aberration is quickly detected by examining the intensity gradient between the four pupil images. However, if the aberration becomes too great, three of the four pupil images will not receive any light. This results in a similar gradient between the last two columns, making it impossible to distinguish the measured amplitude aberration.

To balance this, modulation of the PSF is introduced by a modulator at the tip of the pyramidal prism, as shown in figure 2.4. The two bottom rows of Figure 2.6 show the same tip-til aberration in the presence of modulation. As shown on the detector planes, the light illuminates all four pupil images, even in the last column. However, this comes as a cost of the sensitivity as the gradient is less strong than in the two top rows. This is the sensitivity/dynamic range trade-off.

2.3.2.2 Optical Dispersion and double pyramid designs

The pyramidal prisms used within the PWFS introduce unavoidable chromatic dispersion at the pupil. A double pyramid configuration using multiple glasses can reduce the amount of chromatic pupil dispersion Tozzi et al. (2008), but it is difficult to reduce chromatic pupil dispersion to zero over a wide waveband. There have been no detailed studies investigating the impact of wide spectral bandpass PWFS performance, however, Schwartz et al. (2020) shows that the HARMONI PWFS performance degrades when the pupil is offset by 0.2 PWFS pixels. Magniez et al. (2022) demonstrates that the HARMONI pyramid design achieves a level of residual pupil dispersion well below the 0.1 pixels across a wavelength range of 0.7 to 2.2 μm. However, when operating at central wavelengths of less than 0.8 μm, the bandpass of the HARMONI PWFS design where chromatic pupil dispersion can be ignored can be restricted to a few tens of nanometers bandpasses only.

2.3.2.3 Optical gains and compensation

PWFS suffers from non-linearity introduced by the difference in response between calibration and observation conditions. This nonlinearity is characterised by a spatial frequency-dependent sensitivity loss, commonly referred to as optical gains. If we consider $\vec{c}$ the real modal decomposition of the input phase screen, $\vec{og}$ the optical gains and $\vec{c}_{wfs}$ the modal decomposition measured by the wavefront sensor then:

$$\vec{c} = \vec{og} \times \vec{c}_{wfs}. \tag{2.33}$$

There are several methods for measuring optical gains Deo (2019); Chambouleyron et al. (2020), but they require knowledge of the loop behaviour depending on atmospheric conditions. As a significant portion of this work focuses on optical gain compensation, further details will be provided section 3.3.

2.4 Microwave Kinetic Inductance Detector, a superconducting detector for AO

The requirements for an AO detector are chosen to minimise the impact on the various components of the error budget:

- Fitting error: increase the resolution to meet the DM resolution
- Temporal error: the detector requires a fast readout
- Noise: The readout noise must be minimised, and photon detection should be optimised.

Currently, the detectors are performing well in meeting the requirement for an 8-meter telescope (Gach et al., 2014; Hardy et al., 2020) and the design of the detector for the PCS instrument is in progress (Owton et al., 2023). But their contribution is only to minimize the error contribution of the WFS to the AO loop. An MKID array goes beyond this by providing additional chromatic and temporal information, enabling us to develop new reconstruction techniques.

This section introduces MKIDs, how they work, how they are likely to evolve in the future, and present a comparison to current detectors.

2.4.1 Principle of operation

A MKID is a superconducting detector with the capability to provide a measure of energy and arrival time for an incident photon. As described in Day et al. (2003); Mazin et al. (2012, 2019), each MKID is an inductor-capacitor resonator where the superconducting light-sensitive element is the inductor. Incident photons modify the inductance of the superconducting element. To sense the change in inductance, a probe microwave signal is sent into the resonator. The change in inductance induces a change in the phase of the microwave signal in the form of a pulse,

see Figure2.7. The amplitude of this pulse is proportional to the energy of the photon. Because its superconducting properties mean that the energy required for detection is much lower than the energy of a photon, a MKID detects incoming photons without false counting. It is therefore considered to have zero readout noise. It should be noted, however, that there is a time following the detection of a photon during which the reception of another photon can lead to saturation. When this happens, the photons are typically ignored.

Unlike other energy-sensitive detector technologies (see O'Connor et al. (2019) for a review), MKIDs can be multiplexed into large arrays (McHugh et al., 2012) by designing each MKID to resonate at a different frequency. The individual resonant frequencies are then monitored simultaneously using a frequency-domain multiplexing scheme (McHugh et al., 2012). MKID pixels are typically sampled at 1 MHz, providing a photon arrival time accuracy of $\sim$1 μs. The output of the MKID array is then a list of photons for which we have a position, an energy measurement and an arrival time. From this list, we build a frame with greater flexibility in the reconstruction of an image, where one could for example impose a fixed signal to noise ratio (SNR) per frame at the expense of a variable frame rate.

2.4.2 Current development status

The first MKID-based instrument for optical/IR astronomy was ARCONS at the Palomar Observatory in 2010 (Mazin et al., 2013). It contained a 2024-pixel MKID array, which had an energy resolution of $\sim$5 and operated in the range 400-1200 nm with a detector Quantum efficiency (QE) of $\sim$0.2. The energy resolution is defined as the ratio between the width at half maximum (FWHM) of the detection pulse and the position of the pulse, E, often expressed as a percentage. Formally :

$$R_E = \frac{FWHM}{E} \tag{2.34}$$

Since this first demonstration, larger arrays have been made leading to the 20,440-

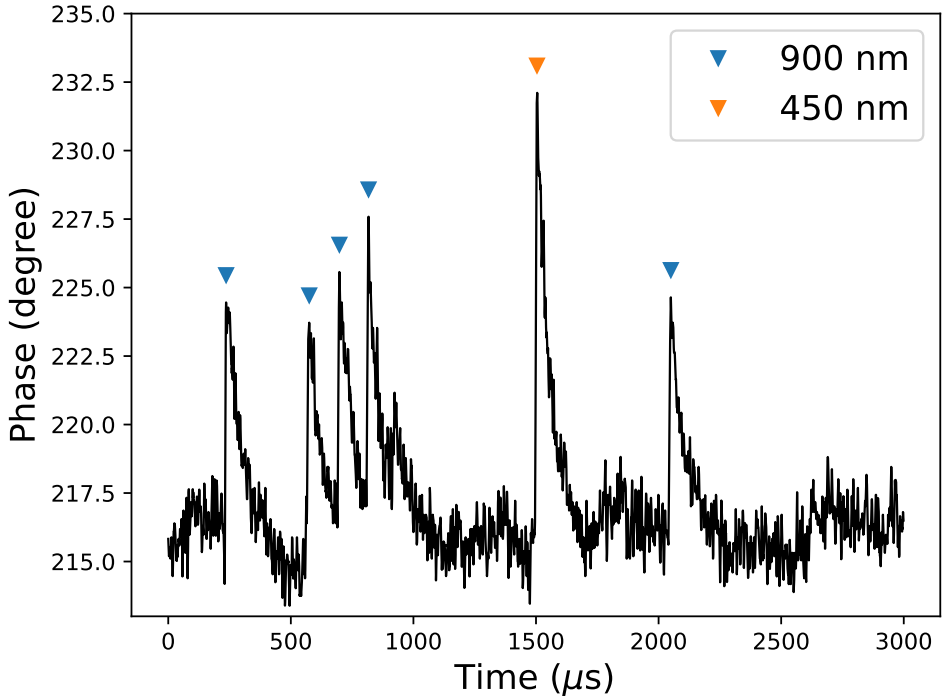

Figure 2.7: Example of output MKID data stream showing the characteristic resonator phase change against time for detection of 6 different photons over 3 milliseconds at wavelengths of 450 nm and 900 nm.

pixel array in the MEC instrument (Walter et al., 2020). Further advances in energy resolution and QE have been demonstrated at the single-pixel level and are currently being incorporated into the designs for arrays (Zobrist et al., 2022).

The highest measured energy resolution of a single MKID pixel is 52 at 402 nm de Visser et al. (2021). While this still requires to be built into a large array, existing kilopixel-scale MKID arrays such as MEC can effectively discern up to 9 wavebands between 400 and 1700 nm, as shown in Fig. 2.8. The effective frame rate enabled by an MKID array exceeds those of existing EMCCD or avalanche photodiodes arrays (also known as Saphira detectors) currently used for AO. Figure 2.7 shows the output data stream from an MKID when several photons are incident on the detector over a 3 millisecond period. In high flux conditions, the arrival of two or more photons on the same pixel leads to a phenomenon where a second photon arrives before the resonator phase has returned to its equilibrium state (or

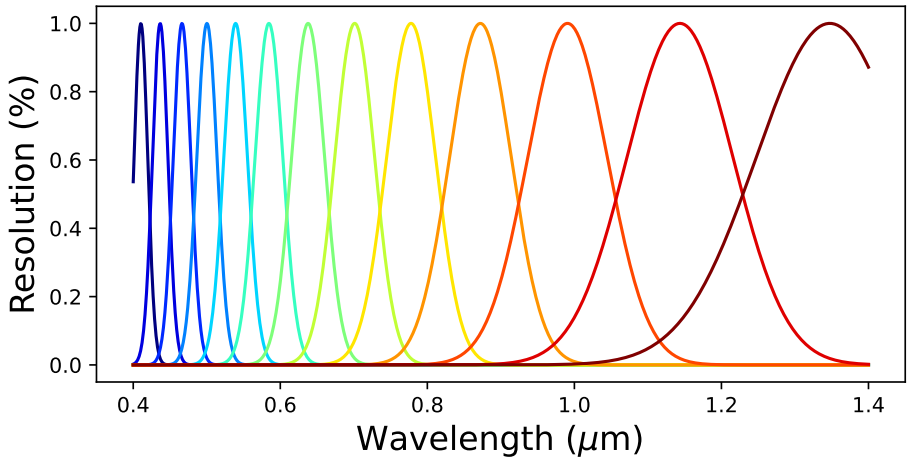

Figure 2.8: Energy resolution distribution of a MEC-like MKID array with an energy resolution of 7 at 1.1 μm

recombination time). This makes it more difficult to determine the pulse height and may even appear as a single higher energy photon if two photons arrive within the rise time of the pulse. The likelihood of this occurring can be reduced through a combination of instrument design (e.g. oversampling), array design (e.g. faster recombination timescales), or read-out design (e.g. more complex pulse detection algorithms), but in practice, any pulse overlap may decrease the accuracy of the measurement of incident photon energy.

The MEC MKID array has a similar number of pixels to existing AO detectors used on 8 meter class AO instruments. Scaling MKID array technology to sizes required for future instruments on ELT-scale telescopes, such as PCS, requires development, but we note that MKID array pixel geometries are not limited to square arrays. For instance, a circular array can be manufactured to match the shape of the PWFS pupil, thus reducing the required number of pixels further.

2.4.3 MKID for XAO

In Tab. 2.1 we show the AO-relevant characteristics for current detectors and compare these to the MEC array. We also show potential characteristics of a

future MKID array for a PCS-like instrument assuming a pupil sampling of 210 pixels. We have defined the number of pixels as the minimum needed to sample the four illuminated circular pupils. Unlike existing WFS detectors, MKID arrays can provide high QE across the full visible and NIR spectral range simultaneously, with a demonstrated QE of over 80 per cent between 400 and 1550 μm Kouwenhoven et al. (2022). We note that when using an EMCCD in high-gain but not photon-counting mode, as is the case in AO, the electron multiplication causes an excess of noise equivalent to a 50% reduction in quantum efficiency Robbins and Hadwen (2003) that is not the case for the photon-counting MKID.

Table 2.1: Comparison between the detectors EMCCD Feautrier et al. (2010) and Saphira Feautrier and Gach (2022) commonly used in astronomical AO systems, the current MKID array used in MEC and the expected achieved performances for an ELT-scale instrument PWFS MKID array. The spectral bin of an MKID design for a PWFS has yet to be determined

	Saphira	EMCCD	MEC	PWFS MKID
Pixel count	81920	57600	20440	>140000
Read noise (e^-)	0.6	0.5	0	0
Sampling (kHz)	3.5	2	1000	1000
Pixel size (μm)	24	24	150	150
QE	0.8	0.9	0.3	0.8
Wave. range	IR	Vis	IR+Vis	IR+Vis
Spectral bins	1	1	9	?

CHAPTER 3

HYPERSPECTRAL WAVEFRONT SENSING SIMULATION

Several AO end-to-end simulations have been developed (Conan and Correia, 2014; Ltaief et al., 2016), but none have been used to incorporate the unique properties that MKID detectors could bring to the system as wavefront sensor detectors. This chapter focuses on the modelling of a MKID-based PWFS, with particular emphasis on the implementation of energy sensitivity. The approach involves introducing a traditional diffractive monochromatic PWFS model at a specific wavelength and a more computationally efficient but approximate convolutional model, which are then extended to multiple wavelengths, forming distinct chromatic PWFS_λ channels of the MKID-based PWFS system.

To evaluate the performance of the wavefront sensor, integration into an end-to-end simulation is critical. The `soapy` simulation developed at Durham University (Reeves, 2016), in which we integrate our PWFS model is first described. The second section provides details of both a diffractive PWFS model and a convolutional model, elaborating on the aspects brought by the use of an MKID. Finally, we discuss the computation of the optical gains curves, detailing 3 different methods.

3.1 End-to-end AO simulation

This section describes the end-to-end Monte Carlo simulation used in this thesis. Soapy is an object-oriented simulation written in Python. After describing the different modules of Soapy, we detail the list of the parameters used for the simulation.

3.1.1 The end-to-end simulation modules

Here we describe the Soapy modules used to simulate the system calibration stage and the AO correction loop. Figure 3.1 describes the different steps in the simulation. Soapy takes as input a parameter file containing the physical and computation parameters of the simulation.

Simulation The simulation module is the top-level object that manages all the other modules used within the simulation and defines how modules are linked together. It provides the main user control and data interface for the simulation. The simulation module also contains routines for system calibration and controlling the AO loop and saves output data (such as WFS measurements, DM commands and the short or long-exposure PSF) as FITS files (Wells, D.C et al., 1981).

Atmosphere The atmosphere module generates an atmospheric phase screen according to the Kolmogorov statistics. It consists of generating turbulence-induced phase aberrations, modelled as a random process with a defined power spectrum, described in section 2.1.2, which are commonly generated on a discrete two-dimensional grid. The process involves filtering white Gaussian noise with the square root of the power spectrum, in the frequency domain and then transforming the filtered spectrum to the spatial domain using the Fast Fourier Transform (Cooley and Tukey, 1965). This results in a representation of a two-dimensional phase screen, ϕ_{atm},

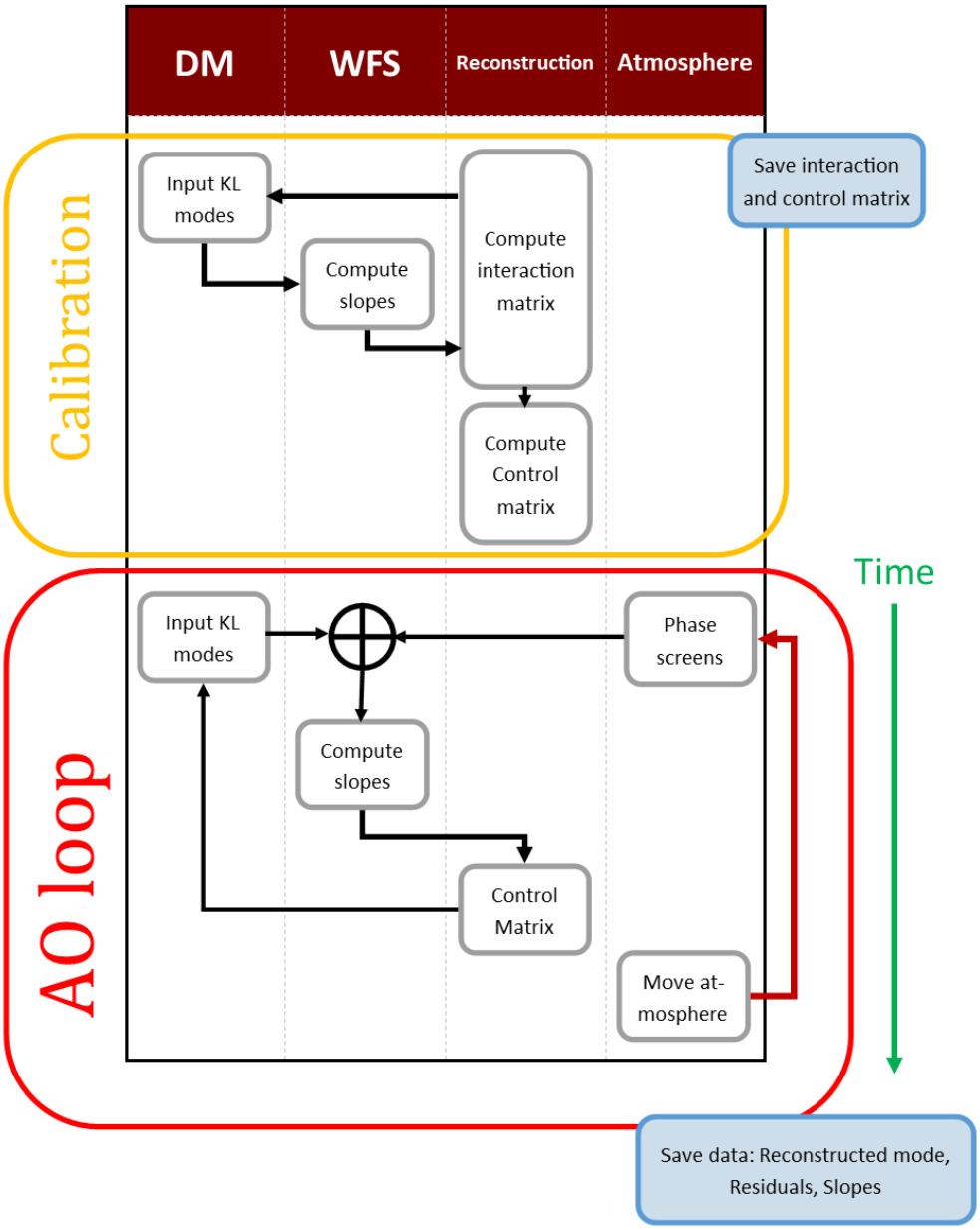

Figure 3.1: Diagram describing the Soapy simulation. Each column describes the key modules of the simulation. The grey square represents the main functions and the blue the data saved by the simulation. The arrows show the interactions between the different modules

characterised by its strength r_0. The detail of the process is described in Schmidt (2010). An example of an atmospheric phase screen can be found Figure 3.2.

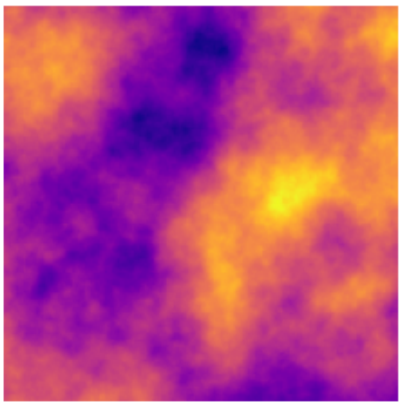

Figure 3.2: Example of an atmospheric phase screen generated by the atmosphere module of Soapy.

Deformable mirror This module simulates the wavefront correction introduced by the DM. These are either expressed as a linear combination of orthogonal circular/annular modes (including the Zernike and KL modal bases), a linear sum of actuator influence functions, or as a 2-dimensional order-N polynomial interpolated phase surface. In this thesis, only the linear combination of modal bases is considered. During simulation, the input to the DM module is a vector of modal coefficients describing the amplitude of each DM mode. Configuration of this module requires the definition of the selected modal base using a file containing a 2-dimensional phase shape for each mode to be controlled. We generated our KL modal basis with `OOPAO`, a Python simulation derived from `OOMAO` (Conan and Correia (2014)).

Wavefront sensor The WFS module takes a phase screen as an input (eg. residuals after correction or modal basis of the DM depending on the stage of the simulation) and returns a vector of wavefront measurements, called "slopes". The parameters chosen for this module are wavelength, number of pixels in the pupil images and amplitude of modulation. Soapy contains several wavefront sensor models such as the Shack-Hartmann wavefront sensor or the PWFS. The latter, being an important part of this work is fully described in the next section. To model a hyperspectral PWFS, Soapy simultaneously runs several instances of a

PWFS, each representing the different PWFS$_\lambda$ channels at a different wavelength of the MKID-based PWFS. This provides a model of the MKID-based PWFS but consider an infinite energy resolution and no saturation effects due to the arrival of two photons in a short delay.

Reconstruction The purpose of the reconstruction module is to translate the measurements made by the WFS into the modal basis used by the deformable mirror, whilst also applying any control law that is needed to ensure the stability of the AO loop when correction is applied. The reconstruction method uses a proportional-integral controller as described in equation 2.22. The reconstruction module contains functions to compute the interaction matrix of the system as well as the control matrix (Moore Penrose pseudo-inverse of the interaction matrix (Campbell and Meyer, 1991)) using the `numpy` module (Numpy Community, 2020).

3.1.2 Simulation parameters

In Table 4.1 we list the different parameters used in the simulation. We give their units and their symbols as well as a short description.

Table 3.1: Table of parameters used for the PWFS models

Name	Symbol	Unit	Description
Wavelength	λ	nm	Wavelength at which a PWFS$_\lambda$ channel operates.
Telescope diameter	D	m	Diameter of the telescope on which the AO system operates.
Modulation radius	r_m	arcsec	Modulation radius of the PSF.

PWFS subapertures	n_s	pixel	Number of pixels across one pupil image on the detector plane.
Pupil separation	n_{ps}	pixel	Number of pixels that separate edges of the pupil images on the detector.
Detector size	S_d	pixel	Width of the detector in pixels. The detector is considered square.
Pupil sampling	N	pixel	Sampling of the input pupil of the wavefront sensor module.

3.2 MKID-based pyramid wavefront sensor model

In line with the overall aim of this thesis, the model presented here was designed to simulate the wavelength-sensitivity of a PWFS that made use of an MKID detector. To do so, we model our system as a multi-colour PWFS from which every PWFS$_\lambda$ channel represents the behaviour of a monochromatic PWFS operating at a given wavelength simultaneously observing the same wavefront aberration with the same PSF modulation applied. We present two models that could be used to model a PWFS$_\lambda$ channel: the diffractive model, integrated into the Soapy simulation (Magniez et al., 2022), and the convolutional model (Fauvarque et al., 2019).

While the diffractive model provides a physically accurate description of light propagation in the PWFS, the convolutional model is an approximation of the diffractive model, using a single convolution operation to efficiently describe the linear behaviour of a PWFS. The choice between these models depends on the required level of accuracy for a particular application and the computational resources available.

After describing both models, we discuss the impact of the wavelength on the

PWFS behaviour and how to integrate them into an end-to-end simulation.

3.2.1 Diffractive PWFS model

We describe how the diffractive model is implemented by considering the electric field of the three principal planes in the PWFS: the pupil plane Ψ_p, the focal plane where the pyramid mask electric field Ψ_{pyr} is applied to the modulated PSF, and then the detector plane Ψ_d from which we deduce the intensities on the detector and calculate the PWFS slopes.

3.2.1.1 Pupil plane

The pupil plane holds all the information of the wavefront entering the PWFS. It is the first stage of our PWFS model. The input phase can either describe the DM shapes used for the calibration, uncorrected atmospheric turbulence, or the residuals after AO correction. Within the PWFS module, the input pupil plane is where we introduce the tip-tilt phase induced by the high-speed modulation mirror. The electromagnetic field Ψ_p in the pupil plane for an input phase screen ϕ is described by

$$\Psi_p(\phi) = \mathbb{I}_p \exp(i(\phi + \phi_{mod})) \quad \text{where} \quad \phi = \phi_{atm} + \phi_{DM} \tag{3.1}$$

where

ϕ_{atm} is the atmospheric perturbation phase screen generated by Soapy. During the calibration ϕ_{atm} is set to 0.

ϕ_{DM} is the DM shape phase screen computed by the reconstruction module to compensate for the atmospheric perturbations. In a perfect AO system $\phi_{atm} = -\phi_{DM}$

$\mathbb{I}_p$ is the pupil mask. The incoming phase screen is filtered by the aperture of the telescope. During this work, we consider a circular mask with a central obstruction. This is a classic mask for an 8-meter telescope such as the Very Large Telescope. The central obstruction is set to 1.1 m and no spiders of the telescope are considered to avoid any differential piston effect (Bertrou-Cantou et al., 2022).

ϕ_{mod} modulation phase. The modulation of the PSF is introduced by a tip-tilt mirror which is modelled by the superposition of a tilted phase on the phase at the input pupil.

Typically, the modulation path of the PSF follows a continuous circle around the tip of the pyramid with a fixed angular offset. A full modulation occurs once per WFS exposure. To emulate this within the simulation, Eq. 3.1 is computed multiple times, each time with a new Ψ_p to generate a discrete number of points on the circular path, as shown in Figure 3.3. For each modulation point, the full propagation sequence from the input phase to the detector plane must be calculated. This means that the speed of the simulation scales linearly with the number of modulation points needed to simulate the circular path.

To reduce the computation time of the simulation, we do not consider the evolution of the atmospheric phase during a modulation step. This assumption means we consider the completion of the modulation instantaneous. This approximation may not be valid for long exposure wavefront sensors, or AO systems that operate in high-wind speed conditions. When considering the photon counting of an MKID, this approximation must be removed and each modulation step must be simulated considering the turbulence displacement.

3.2.1.2 Focal plane

The next principal plane in the system is the focal plane which is placed at the tip of the pyramid. The plane is composed of 2 elements: the modulated PSF and the

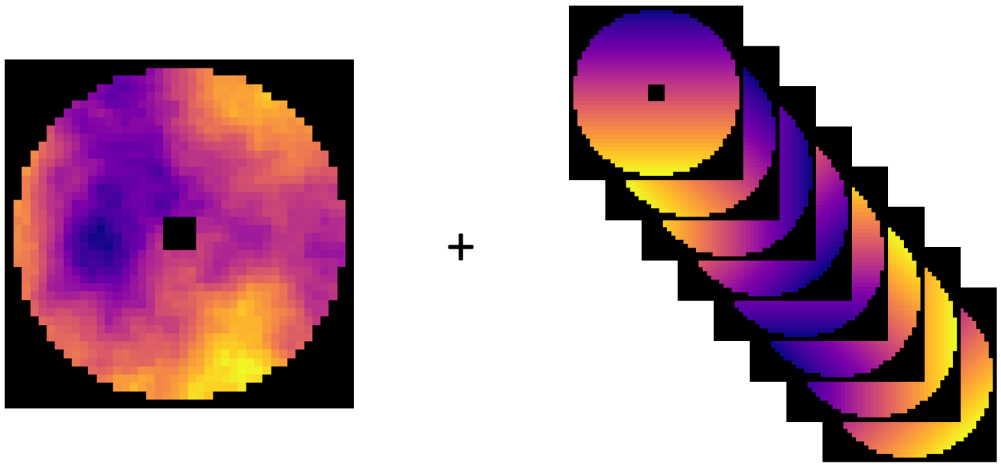

Figure 3.3: Illustration of the pupil masked phase screens used within the diffractive PWFS model. Left: an example of an atmosphere-perturbed wavefront phase screen. Right: several tip-tilt phase screens are required to represent an eight-step modulation.

pyramid phase screen.

Modulated PSF The modulated PSF is computed as the Fourier transform of the electric field of the pupil plane Ψ_p. In the same way that the pupil plane is decomposed in each modulation step, the modulated PSF is calculated for each modulation step, as shown in Figure 3.4.

Pyramid mask The four-sided pyramid mask electric field Ψ_{pyr} is then applied to the modulated PSF using a simple multiplication. The pyramid used here is a 4-faced prism with a tip angle ϑ and a tilt angle Θ for each face Ω (see Figure 3.5(a)). If we consider ω the absolute value of the tip and tilt of 4 faces of the pyramid:

- Ω_A: $\vartheta = \omega$, $\Theta = -\omega$
- Ω_B: $\vartheta = \omega$, $\Theta = \omega$
- Ω_C: $\vartheta = -\omega$, $\Theta = -\omega$
- Ω_D: $\vartheta = -\omega$, $\Theta = \omega$

To generate the pyramid phase profile, we start by defining a quadrant operator $\mathbb{I}_\Omega$

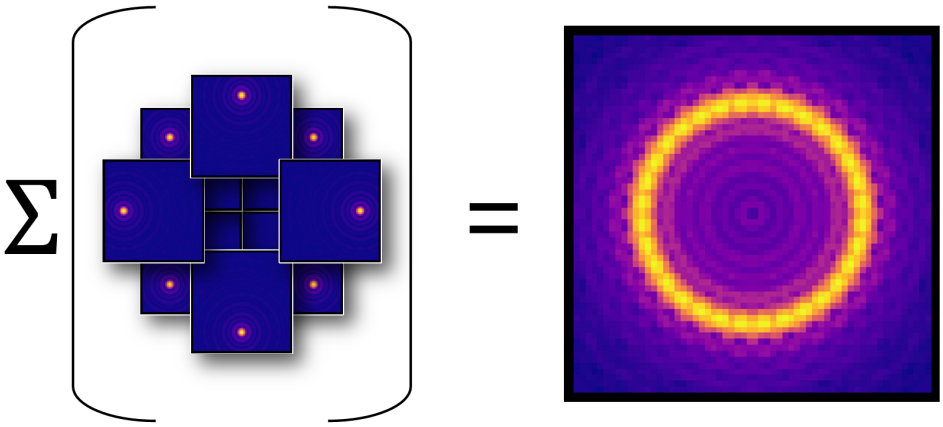

Figure 3.4: Modulated PSF of a flat wavefront. The plot on the left represents the sum of all the PSF at each step of the modulation using the Fourier transform of Ψ_p.

that selects a single pyramid face over which we create a tilted phase. By defining ϕ_Ω the phase associated with the tilted phase aberration, we define the pyramid mask phase screen ϕ_{pyr} as

$$\phi_{pyr} = \sum_{i=A,B,C,D} \mathbb{I}_{\Omega_i} \phi_{\Omega_i} \tag{3.2}$$

Figure 3.5(b) shows an example of a pyramid mask phase screen ϕ_{pyr} using Equation 3.2. Ψ_{pyr} is then calculated from ϕ_{pyr} as $\Psi_{pyr} = e^{i\phi_{pyr}}$

3.2.1.3 Detector plane and PWFS slopes

The transition from the Pyramid focal plane to the detector plane is made using the Fourier transform $\mathscr{F}$ and in the inverse using the inverse Fourier transform $\mathscr{F}^{-1}$. We can then compute the electromagnetic field of the detector plane Ψ_d from Φ_p and Ψ_{pyr}

$$\Psi_d(\phi) = \mathscr{F}^{-1}(\mathscr{F}(\Psi_p) \times \Psi_{pyr}(\phi)) \tag{3.3}$$

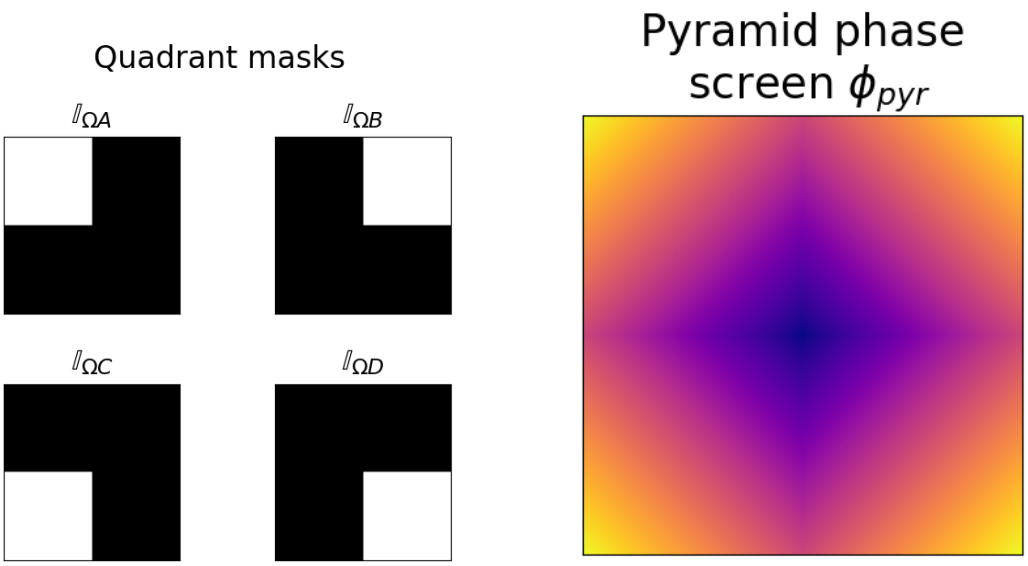

(a) (b)

Figure 3.5: (a) Illustration of the quadrants masks used to compute ϕ_{pyr}. (b) Pyramid mask phase screen example.

We convert this into an intensity in the detector plane used for the wavefront reconstruction using the following equation:

$$I = |\Psi_d|^2 \tag{3.4}$$

It is then this intensity map that is used to compute the slope vector.

Convolution Using the convolution theorem, we can see that equation 3.3 is a convolution product between the plane pupil and the Fourier transform of the pyramid mask.

$$\Psi_d(\phi) = \Psi_p(\phi) \star \mathscr{F}(\Psi_{pyr}) \tag{3.5}$$

where $\star$ represents the convolutional product. This is in line with the formalism developed by Fauvarque et al. (2016), which they used to develop the convolutional model detailed in the last section of this Chapter.

3.2.2 Convolutional model

The convolutional model is a simplified representation of PWFS that enables the calculation of its linear response. This approach computes the impulse response of the system but with some approximations detailed below. Fauvarque et al. (2019) initially introduced this modelling approach, and despite its simplifications, it is advantageous as it significantly reduces computational demands.

Computation of the linear response the PWFS

When studying a physical system, a very generic method of characterising the system is to investigate its response to a Dirac impulse-type excitation. A system is said to be convolutional if its output can be described as a convolution of the input with a quantity called the impulse response, which corresponds to its response to a Dirac delta function. For a phase ϕ at the input, a WFS represented in the convolutional formalism is written as follows :

$$\Delta I(\phi) = \mathbf{IR} \star \mathbb{I}_p \exp(i(\phi) \tag{3.6}$$

where $\Delta I(\phi)$ the linear response of the PWFS to the input phase ϕ and $\mathbf{IR}$ is the impulse response of a PWFS. Figure 3.6 illustrates an example of this model using the impulse response of a four-sided PWFS. The slopes are then measured the same way as the diffractive model with Equation 2.31 and Equation 2.32.

Impulse response

Using as a starting point the equation of the linear intensities Fauvarque et al. (2016), one can find the impulse response of a PWFS a function of the mask ϕ_{pyr} and modulation function w (Fauvarque et al., 2019)

$$\mathrm{IR} = 2\mathrm{Im}(\overline{\mathcal{F}(\phi_{pyr})}(\mathcal{F}(\phi_{pyr}) \star \mathcal{F}(w))) \tag{3.7}$$

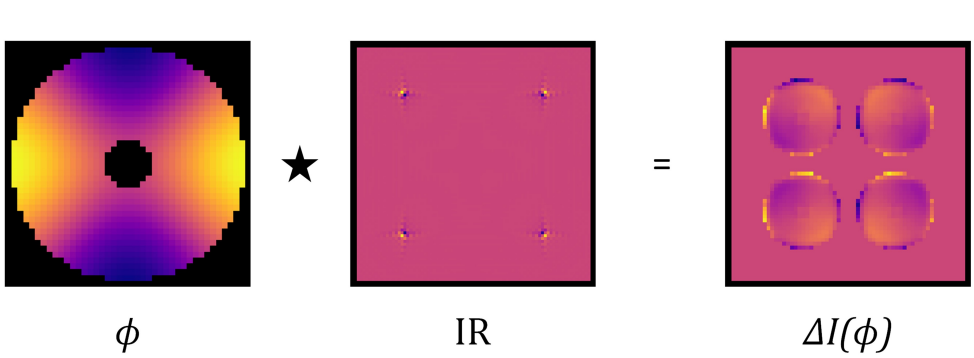

Figure 3.6: Graphical representation of equation 3.6 for a 4-sided pyramid with Equation 3.9 the expression used to compute impulse response (IR)

where $\overline{x}$ is the conjugated of x. This impulse response equation has been defined under the sliding pupil assumption, which is detailed later.

Modulation function w

The modulation function encodes the time spent by the PSF at each modulation step. In the case of our simulation, we consider a circle of a radius corresponding to the modulation amplitude and uniform weighting along the modulation path, as shown Figure 3.8(a).

Sliding pupil approximation

One fundamental characteristic of convolutional systems is that they are invariant under translation. As WFS are limited by the pupil apertures $\mathbb{I}_p$, they cannot be fully convolutional systems. The system is insensitive to phases occurring outside the pupil. Therefore, there is a difference in response depending on the position being considered in the input space i.e. the amplitude phase in the case of the PWFS.

To address this issue, Fauvarque et al. (2016) has defined the sliding pupil approximation. This involves treating the impulse response as the linear response to a Dirac pulse at the centre of the pupil. This approach treats every phase point

within the pupil as though it were located at the centre, ensuring an equal distance from the edges. Consequently, the pupil "slides" along with the impulse response as illustrated Figure 3.7.

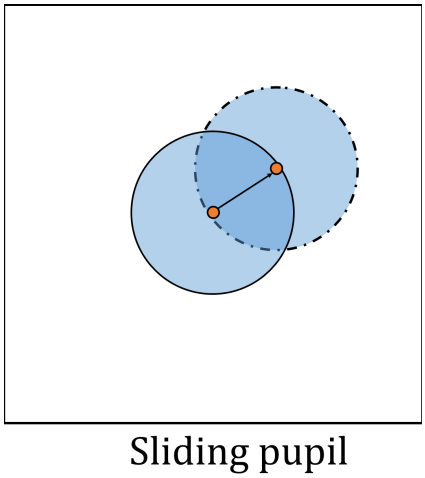

Figure 3.7: Diagram showing the sliding pupil where the Dirac pulse "sees" the edges, but always at the same distance

Evolution of the model for complex pupil shapes

The sliding pupil approximation does not work with central obscuration or more complex pupil shapes. Chambouleyron (2021) developed an updated approach that is used within this thesis. This approach proposed to modify the modulation function w by an energy distribution in the focal plane, which we plot Figure 3.8 operating the following transformation

$$w \leftarrow w \star |\mathcal{F}(\mathbb{I}_p)|^2 \tag{3.8}$$

takes into account the effect of the pupil mask ($\mathbb{I}_p$) in the impulse response. It is modelled through its PSF in the focal plane.

We can now express the impulse response for a PSF of a flat wavefront and the Equation 3.7. After applying the convolution theorem the impulse response becomes

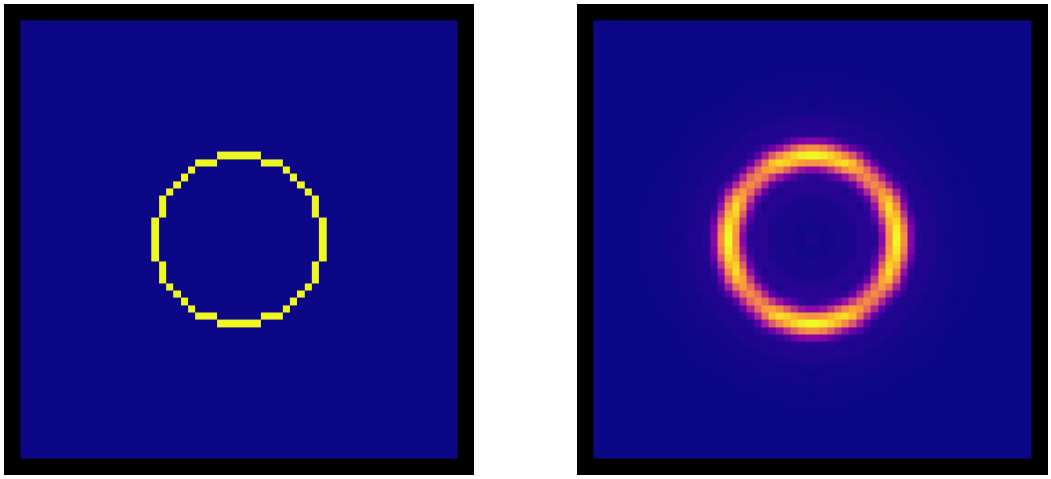

(a) w (b) $w \star |\mathcal{F}(\mathbb{I}_p)|^2$

Figure 3.8: (a) Plot of the modulation function and (b) energy distribution in the focal plane. We note the similarity with Fig. 3.4

$$\text{IR} = 2\text{Im}\left(\overline{\mathcal{F}(\phi_{pyr})} \times \left(\mathcal{F}(\phi_{pyr}) \star \mathcal{F}(w)\mathcal{F}(|\mathcal{F}(\mathbb{I}_p)|^2\right)\right) \tag{3.9}$$

This equation is the expression used to compute the impulse response for the rest of this thesis

Comparison with the diffractive model

From this, it is apparent that the convolutional model exhibits a significant increase in computational efficiency compared to the diffractive model. Once the impulse response has been calculated for a given PWFS, the convolutional model only requires the convolutional product equation 3.6 to be calculated for each new input phase. Unlike the diffractive model, which necessitates computing the light propagation between 3 planes for each modulation step. This decrease in operations is beneficial for heavy computing tasks, such as optical gains computation or parallelization of multiple PWFS computations for every AO loop iteration, as is the case with the model of MKID-based PWFS. Although Chambouleyron et al. (2020) demonstrate that both models have a general agreement, they also show that they differ slightly in sensitivity at low spatial frequencies. This is explained

by the sliding pupil hypothesis used in the development of the convolutional model. References to this discrepancy can be found in Fauvarque et al. (2019).

3.2.3 PWFS$_\lambda$: Chromatic channels

We now look at how to incorporate the MKID properties into these models. Two aspects could be implemented: temporal resolution and wavelength sensitivity.

To implement the photon counting property it is necessary to update ϕ_{atm} at each modulation step within the PWFS module. This increases the simulation computation time considerably but may be required to fully investigate the temporal behaviour of the system, particularly if a time-resolved detector, such as an MKID is used. As the MKID-based PWFS model developed for this thesis concentrates on wavelength dependency and already demands more computational power, the temporal aspect of MKID have not been explored further in this work.

As previously explained, our hyperspectral PWFS model is implemented by parallelizing multiple PWFS$_\lambda$ channels. Each channel represents an iteration of the same PWFS, which is modelled using a PWFS model and shares a set of parameters except the operating wavelength. In this section, we describe how to incorporate the wavelength dependence into a PWFS model and how to choose the set of parameters common to all PWFS$_\lambda$.

There are three major chromatic impacts in the PWFS behaviour and performance: the atmospheric turbulence strength, the chromatic dispersion induced by the prism and the size of the PSF.

Atmospheric turbulence strength We have seen in the previous chapter that the impact of atmospheric turbulence on the PWFS depends on the wavelength at which it is measured. In the Soapy simulation, this effect is handled by an external module to the WFS and is responsible for providing as input the atmospheric phase screen in the correct units, scaled to the WFS operating wavelength.

Chromatic dispersion We make the hypothesis that the chromatic dispersion is within the 0.1-pixel limits for each $PWFS_\lambda$ channel (Tozzi et al., 2008). As a result, there are no chromatic dispersion effects within individual channels, and the spacing between each pupil image on the detector is kept constant across all channels by adjusting ϕ_{pyr}.

PSF size The PSF size in the focal plane depends on the wavelength λ and the diameter of the telescope pupil. In the simulation, the PSF at the top of the prism is the Fourier transform of the electric field of the pupil plane (see section 3.2.1.2). This means the diameter, measured in pixels, in the focal plane of the PSF, depends on the sampling of the pupil. There are therefore two ways to incorporate the wavelength influence in each $PWFS_\lambda$ on the PSF diameter

- Have a different sampling of the pupil for each channel
- Adjust the input phase screen $\phi_{atm} + \phi_{DM}$ and the modulation ϕ_{mod} to the wavelength to preserve all proportions in the focal plane.

As the initial sampling is fixed by Soapy's main simulation module and to avoid any errors due to interpolation, the second solution has been implemented. $\phi_{atm} + \phi_{DM}$ are then converted in optical path difference at the correct wavelength and the modulation radius is adapted.

Physically, every $PWFS_\lambda$ has the same modulation amplitude. This is why the modulation radius r_m is given here in on-sky arcseconds, independent of the wavelength, as opposed to the λ/D unit typically found in the literature (Esposito and Riccardi, 2001; Fauvarque et al., 2017; Bond et al., 2020).

To determine ϕ_{mod}, the value of the modulation radius in pixels in the focal plane needs to be calculated. To do so, a conversion of the pixel size is carried out using the Airy disc size formula and the Fourier transform of the pupil. Measured in

spatial frequency, the size of the PSF is equal to $1/N$ where N is the size of the pupil in spatial sampling, i.e. the number of pixels.

$$r_m^p = \frac{r_m.\mathrm{D}}{1.22\lambda.N} \tag{3.10}$$

where r_m^p is the modulation radius in pixels.

3.3 Optical gain computation

One source of PWFS non-linearity is the impact of residuals on wavefront reconstruction. These result in an underestimation of the reconstructed modes. The quantity measuring this underestimation is called the optical gain. To improve performance, we need to measure the optical gain to compensate for them. Several methods already exist (Korkiakoski et al., 2008; Deo, 2019). Here, we describe a method, developed by Chambouleyron et al. (2021), using a gain scheduling camera to image the modulated PSF at the top of the pyramidal prism during operation on-sky, shown Figure 3.9. Using this residual PSF, we look at the decrease in sensitivity for each mode on the DM basis. To this end, we compute an "on-sky" interaction matrix and compare it with the one measured during the calibration phase.

In this section, we present the method of calculating optical gains curves using an 'on-sky' interaction matrix. To evaluate this method, we also measure the gains by comparing measured modal decomposition by the actual modal decomposition of the input phase screen. Furthermore, we explain how to compute these 'on-sky' matrices using both the convolutional and the diffractive model. Lastly, we conduct a comparative analysis of these methods and engage in a discussion.

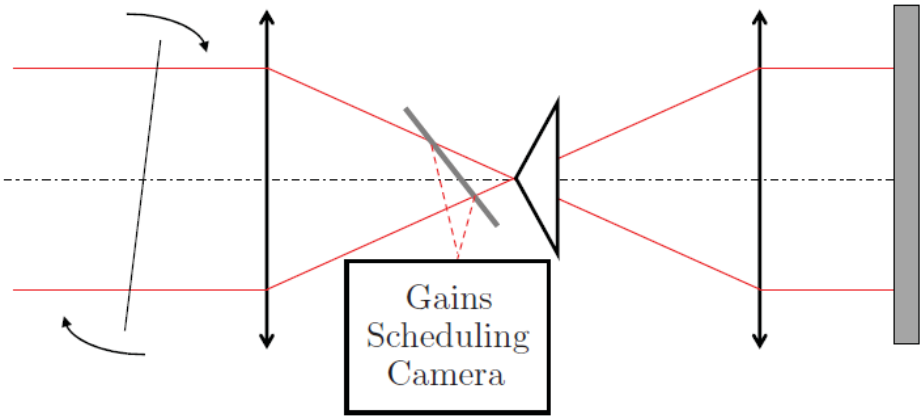

Figure 3.9: Optical diagram of the gain scheduling camera, from Chambouleyron (2021)

3.3.1 Optical gains computation methods

The simulation provides access to the actual input atmospheric phase screen and the coefficients of its modal decomposition. As optical gains are a reduction of the modal decomposition coefficients during on-sky operations, it is possible to determine their values. During operation, we evidently do not have access to the actual wavefront, we therefore need another method.

The on-sky interaction matrix then is measured, enabling comparison with the matrix measured during calibration. Through this comparison, we can determine the attenuation value, mode by mode, caused by residuals and consequently, define the value of optical gains. We outline both procedures to calculate spatial-frequency dependent curves of optical gain in this section.

3.3.1.1 Direct phase comparison

By definition, the optical gain value for a given mode is the ratio of the amplitude of the reconstructed mode to its true amplitude. In a simulation, an alternative method for calculating the optical gain vector involves comparing the true values of the amplitudes of modes describing the atmospheric input phase screen with those

measured by the PWFS. This direct comparison is obviously not possible in a real system, but useful to demonstrate performance here.

By fitting the input and output amplitudes with a linear model, we can then deduce the value of the optical gain for this mode as being the value of the measured slope. This process is demonstrated in Figure 3.10, where a linear fit of the input amplitude of modes 10 and 200, along with the measured amplitudes by a PWFS of a residual phase screen computed by `Soapy`, is presented.

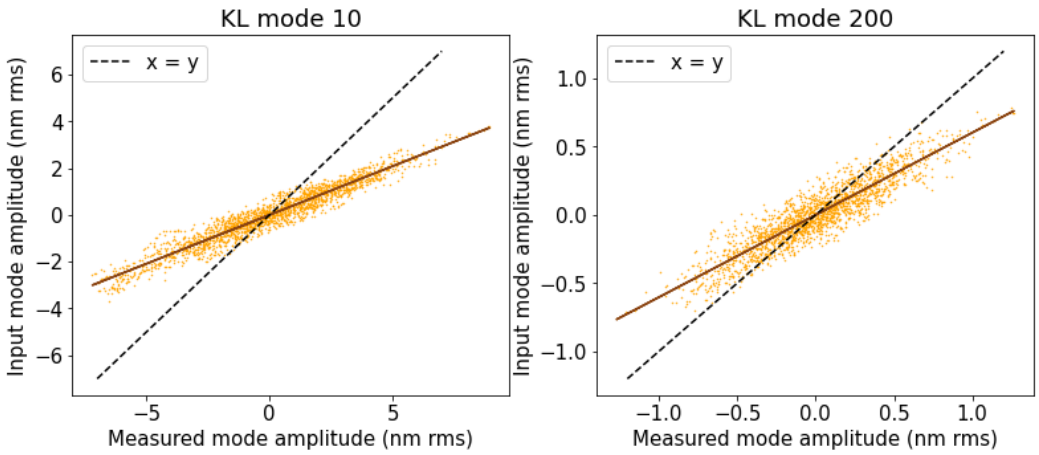

Figure 3.10: Linear fit of the modes 10 and 200 input amplitude and the measured amplitudes modes by a PWFS of a residual phase screen computed by `Soapy`. The slopes of this linear model is the value of the optical gain for these modes.

3.3.1.2 Interaction matrix comparison

The effect of residuals introduces a difference in operating regimes where the calibration is no longer valid. Specifically, when the PWFS is operating around a non-null residual phase, we have the following relationship:

$$I_{res}(\phi) = I_{calib}(\phi + \phi_{res}) \tag{3.11}$$

where I_{res} and I_{calib} are the intensities of a PWFS detector when operating around a non-null residual phase or a flat phase during calibration. Because of the non-linearities of the PWFS, $I_{calib}(\phi_i + \phi_{res}) \neq I_{calib}(\phi_i) + I_{calib}(\phi_{res})$.

As a result, during the computation of the interaction matrix, distinct matrices emerge depending on whether we are in the operation phase or the calibration phase. These are to be referred as the $\mathcal{IM}_{sky}$ and $\mathcal{IM}_{calib}$ respectively. Each row of those matrices is computed from the intensities of the PWFS of a mode ϕ_μ.

We define $\mathcal{OG}$ the transfer matrix between the 'on-sky' interaction matrix $\mathcal{IM}_{on\,sky}$ and the interaction matrix measured during the calibration phase $\mathcal{IM}_{calib}$, and is given by :

$$\mathcal{IM}_{on\,sky} = \mathcal{IM}_{calib}.\mathcal{OG} \tag{3.12}$$

$$\Rightarrow \mathcal{OG} = \mathcal{IM}^{\dagger}_{calib}.\mathcal{IM}_{on\,sky} \tag{3.13}$$

Diagonalisation approximation The assumption of the diagonalisation approximation is that there is no cross-talk between modes during calibration (Deo, 2019). It is valid assuming the PWFS is operating in a linear regime. Under this approximation, $\mathcal{OG}$ is considered diagonal. Optical gains per modes are then calculated by projecting the average over time response, calculated around the turbulence of the mode ϕ_μ, onto the response of the same mode, with the same amplitude, calculated during calibration. The denominator acts as a normalizer (Chambouleyron et al., 2020). For a given mode phi_μ the optical gain og is defined as:

$$og(\phi_\mu) = \frac{\langle \vec{s}_{res}(\phi_\mu) | \vec{s}_{calib}(\phi_\mu) \rangle}{\langle \vec{s}_{calib}(\phi_\mu) | \vec{s}_{calib}(\phi_\mu) \rangle} \tag{3.14}$$

which is the equivalent of

$$\vec{og} = \frac{\mathrm{diag}((\mathcal{IM}_{sky})^T.\mathcal{IM}_{calib})}{\mathrm{diag}((\mathcal{IM}_{calib})^T.\mathcal{IM}_{calib})} \tag{3.15}$$

where $\vec{og}$ is a vector containing all the $og(\phi_\mu)$ for $\mu \in [1, N_{modes}]$.

3.3.2 On-sky interaction matrix

In the simulation, both the diffractive and the convolutional model can be used to calculate $\mathcal{IM}_{sky}$. These two approaches are described below.

3.3.2.1 Convolutional model

The convolutional model, presented section 3.2.2, describes the linear behaviour of a PWFS. It does so by approximating it as a convolutional system and calculating its impulse response which is then convolved with an input phase screen. However, due to residuals during operation, the behaviour of the PWFS changes and a new calibration is required. The change of behaviour impacts the impulse response of the PWFS. A new impulse response is then computed, taking into account the presence of residuals. To compute the optical gain we compare the on-sky and off-sky calibration by calculating the on-sky interaction matrix using the intensities computed with the impulse response with residuals.

Introduction of the residual impact in the impulse response In the presence of residual phases, assuming that they are stationary and isotropic, Fauvarque et al. (2019) shows that the impulse response is modified so that the modulation function becomes, see Fig. 3.11:

$$w \leftarrow w \star |\mathcal{F}(\Psi_{res})|^2 \quad \text{with} \quad \Psi_{res} = \mathbb{I}_p \exp(I.(\phi_{res})) \tag{3.16}$$

with ϕ_{res} a residual phase screen computed beforehand. Outside of simulation, $|\mathcal{F}(\Psi_{res})|^2$ is the residual PSF and is directly given by the gain scheduling camera.

Equation 3.9 is then modified to give the on-sky impulse response

$$\text{IR}_{res} = 2\text{Im}\left(\overline{\mathcal{F}(\phi_{pyr})}(\mathcal{F}(\phi_{pyr}) \star \mathcal{F}(w)\mathcal{F}(|\mathcal{F}(\Psi_{res})|^2))\right) \tag{3.17}$$

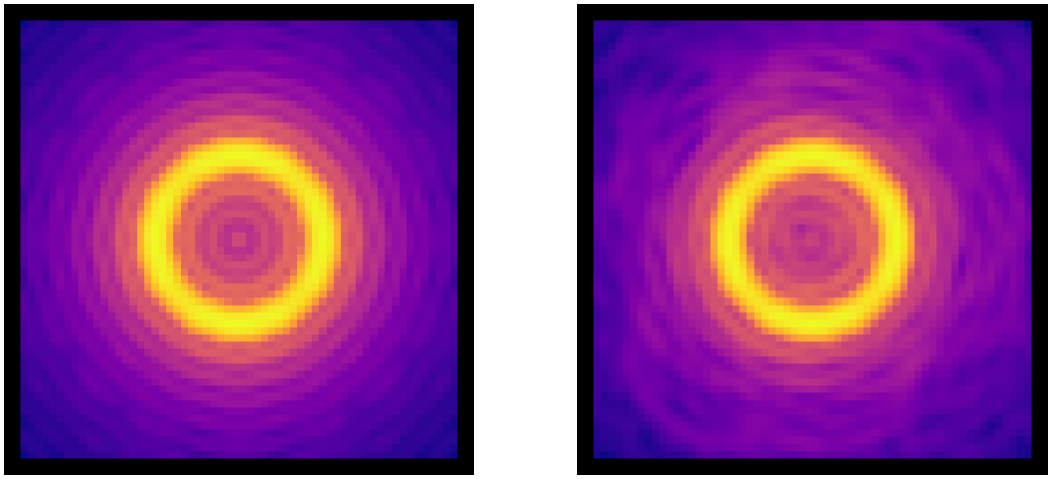

(a) $w \star |\mathcal{F}(\mathbb{I}_p)|^2$ (b) $\log(w \star |w \star |\mathcal{F}(\Psi_{res})|^2)$

Figure 3.11: Plot, in log scale, of the energy distribution in the focal plane for the impulse response (a) for a plane, modulated wavefront and (b) in the presence of residual wavefront error

Computation of $\mathcal{IM}_{on-sky}$ From the on-sky impulse response, it then becomes possible to compute $\Delta I_{res}(\phi_\mu)$ the linear intensity on the detector computed with presence of residuals for a mode ϕ_μ

$$\Delta I_{res}(\phi_\mu) = \mathrm{IR}_{res} \star \mathbb{I}_p \phi_\mu \tag{3.18}$$

We define $\vec{s}_{res}(\phi_\mu)$ the slope vector computed from $\Delta I_{res}(\phi_\mu)$. The expression each row for a mode ϕ_μ of $\mathcal{IM}_{on-sky}$ is then

$$\mathcal{IM}_{on-sky}(\phi_\mu) = \vec{s}_{res}(\phi_\mu) \tag{3.19}$$

For clarity, we introduce the suffix "calib" to denote the impulse response calculated during calibration. This results in the following expression for the linear intensities ΔI_{calib}, for a mode ϕ_μ

$$\Delta I_{calib}(\phi_i) = \mathrm{IR}_{calib} \star \mathbb{I}_p \phi_\mu \tag{3.20}$$

As for $\mathcal{IM}_{on-sky}$, the expression each row for a mode ϕ_μ of $\mathcal{IM}_{calib}$ is then

$$\mathcal{IM}_{on-sky}(\phi_\mu) = \vec{s}_{calib}(\phi_\mu) \tag{3.21}$$

where $\vec{s}_{calib}(\phi_\mu)$ the slope vector computed from $\Delta I_{calib}(\phi_\mu)$

3.3.2.2 Diffractive model

During the calibration stage, the input phase screen is a series of DM modes ϕ_μ and the PSF is computed for the electromagnetic field in the pupil plane $\Psi_p(\phi_\mu)$. As for the convolutional model, to compute the on-sky interaction matrix, we compute the PSF for a residual phase screen ϕ_{res} in addition to the mode phase screen. As in the calibration phase, the rows of the on-sky interaction matrix are the slopes derived from the intensity computed from the electromagnetic field of the detector plane $\Psi_d(\phi_\mu + \phi_{res})$ using the equation 3.3.

3.3.3 Discussion

Comparison with the literature The on-sky interaction matrix is utilized in the process of computing optical gain, as explained in detail by Chambouleyron et al. (2020). In this paper, they compare results obtained with both the convolutional model and a diffractive model Conan and Correia (2014). Some of the optical gain curves presented in Chambouleyron et al. (2020) are shown in Figure 3.12. Optical gain curves exhibit a rapid decrease in the lower modes up to an inflexion point, followed by a slower increase until stabilisation at the higher modes. The optical gains are generated for full atmosphere phase screens using both a diffractive model and a convolutional model. Reproducing the optical gain curves using the convolutional model confirms that our convolutional model matches the original results.

Comparison of methods Figure 3.13 presents optical gain curves for residuals generated with the `Soapy` simulation using the three methods presented in this

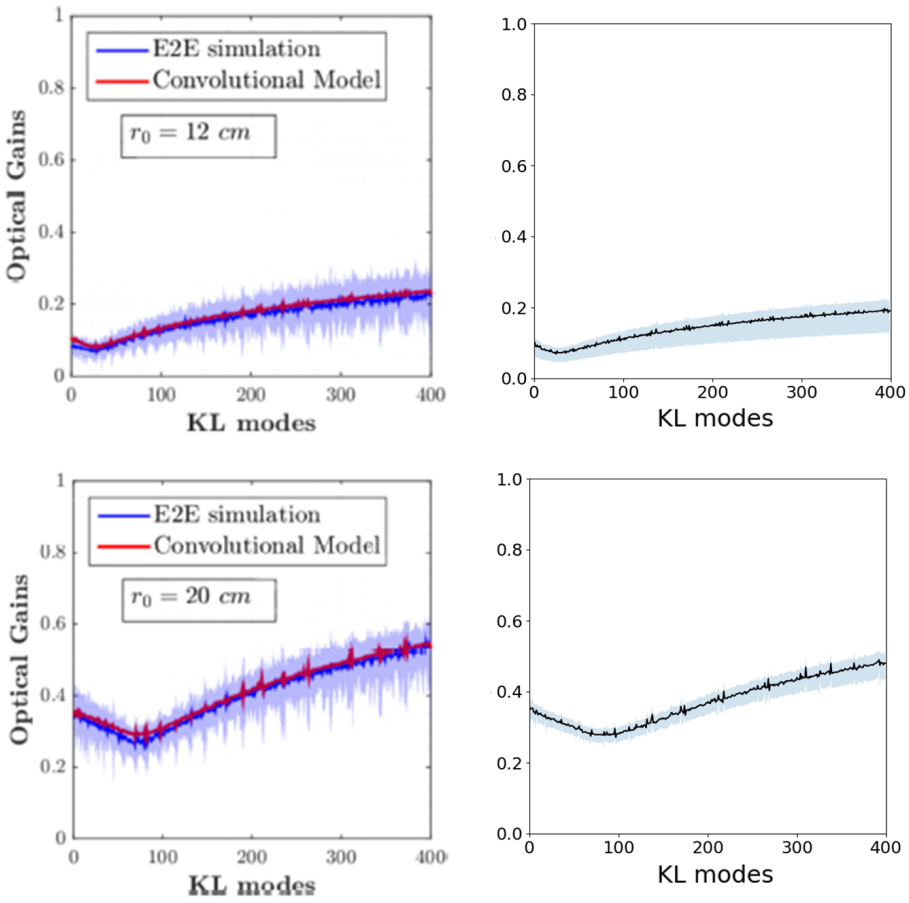

Figure 3.12: Comparison of optical gain curves with results found in Chambouleyron et al. (2020) (left plots) and the convolutional model developed for this work (right plots). The shaded area represents the maximum and minimum values for the OG for 20-phase realisations. Those optical gain curves generated on full turbulence screens for Top: $r_0 = 12cm$ at 550 nm and $r_m = 3\lambda/D$ or 0.02 arcsec, and Bottom: $r_0 = 20cm$ at 550 nm and $r_m = 5\lambda/D$ or 0.06 arcsec

section, and the detail of the legend is

- OG e2e: Optical gain curves obtained using the "Direct phase comparison" method
- OG IM e2e: Optical gain curves obtained using the interaction matrices comparison method computed with the diffractive model

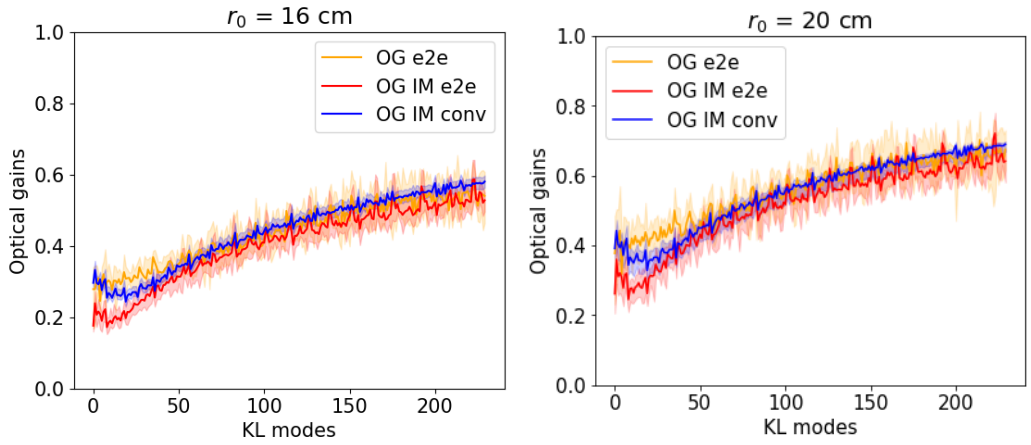

Figure 3.13: Comparison of optical gain calculation methods for 2 values of r_0 at 500 nm for a closed AO loop using `Soapy` over 20 seconds of simulated time. Orange: comparison of input and measured mode amplitudes. Red: $\mathcal{IM}_{calib}$ and $\mathcal{IM}_{sky}$ calculations using the diffraction model, Blue: $\mathcal{IM}_{calib}$ and $\mathcal{IM}_{sky}$ calculations using the convolutional model. Both the red and blue solid lines represent an average of 10 **og** computation using 10 different residual phase screens.

- OG IM conv: Optical gain curves obtained using the interaction matrices comparison method computed with the convolutional model

The results demonstrate agreement among the three methods in the high-order modes. However, there is disagreement in the low-order modes. The difference between "OG IM e2e" and "OG IM conv" can be explained by the fact that the convolutional model does not agree with reality for the low-order modes. Regarding the different"OG e2e" behaviour at low order modes, further investigations are needed.

The two figures presented show the relevance of using the convolutional model for optical gain computation. Due to its computational efficiency over the diffractive model and the fact that the true modal decomposition of the atmospherically perturbed wavefront cannot be known during operation, it is this method that will be used to calculate the optical gain curves for the remainder of this thesis.

3.4 Conclusion

In this chapter, we have described an end-to-end simulation, detailing the different modules outside of the WFS and presenting the parameters to understand what the input and output of the PWFS model are.

We described an MKID-based PWFS model, which consists of simulating energy sensitivity by parallelizing multiple iterations of a PWFS on different channels, denoted PWFS$_\lambda$. Each channel describes a monochromatic PWFS and can be described by a diffractive model, which is accurate but computationally expensive, or a convolutional model, which is an approximation of the former but computationally efficient. Chambouleyron et al. (2020) have shown that both models agree to describe the linear behaviour of the PWFS, but differ slightly in their sensitivity to low spatial frequency. The wavelength dependence is then modelled by scaling both the focal plane and the input phase screen at the wavelength of the channel.

Finally, we present three methods for calculating optical gains, which are recognised as a key limitation in the performance of PWFS. The first approach involves the calculation of an on-sky interaction matrix through gain scheduling, originally implemented for use with the convolutional model. In addition, a parallel evaluation of these interaction matrices was performed using our diffractive model. The third method involves a comparative analysis of the measured modal decomposition with the true modal decomposition to quantify the attenuation in the measurements due to optical gains. As shown in Figure 3.12, our optical gain calculations with the convolutional model agree with those of the original developer, confirming their consistency. Figure 3.13 provides additional evidence, demonstrating the agreement between the three proposed methods. Consequently, both figures underline the reliability of the optical gain calculation using the convolutional model developed in this study. Due to its computational efficiency, this model is selected for all subsequent optical gain calculations throughout the remainder of this research project.

CHAPTER 4

CHROMATIC BEHAVIOUR OF THE PYRAMID WAVEFRONT SENSOR

Whilst sensing at two wavelengths is achievable using dichroic and two independent cameras, extending this beyond two wavelengths quickly becomes optically and mechanically complex and costly. If equipped with a MKID, a PWFS can distinguish several wavebands across a broad passband using the same detector. At this point, it is possible to separate the detected spectrum into several colours. The natural question then arises as to what interesting properties this chromatic discrimination might bring.

In this chapter we look at the operation of the MKID-based PWFS. Initially, we analyse the impact of wavelength on the behaviour of a PWFS. Subsequently, we apply a polychromatic reconstruction method to evaluate the performance of a hyperspectral PWFS. We focus on three aspects. Firstly, we examine the dynamic range and the effect of PSF size for each PWFS_λ channels as well as for the hyperspectral PWFS. Secondly, we investigate the effect of wavelength on optical gain. We look at the performance for different photon levels and how broadening the spectra used improves the performance by increasing the SNR for a given start magnitude. Lastly, we consider the integration on an MKID array in an XAO PWFS, discussing the photon detection, and mode specifically the requirements on the recombination time to manage saturation and the photon distribution within the PCS instrument.

4.1 Simulation set up

In this section we describe the properties of an MKID assumed throughout this chapter and describe a first approach to integrate all chromatic wavefront reconstructions in the AO loop. We also list the values of the parameters used to model an XAO system for an exoplanet imaging instrument. The characteristics of our systems are based on the properties of MEC for the MKID array (Walter, 2019) and SAXO/SPHERE for the rest of the AO system (Sauvage et al., 2016).

4.1.1 MKID spectral resolution: Colour distribution

In the previous chapter, we explained how we simulated an AO system with an MKID-based PWFS by paralleling several iterations of a single PWFS changing the operating wavelength, creating PWFS_λ channels. However, it is yet to be determined how many of those channels could be used for a given MKID device. We outline here an empirical method to determine the optimal number of colours the MKID-based PWFS could have for a given spectral resolution R. We give here the definition of the spectral resolution :

$$R_0 = \frac{\lambda_0}{\Delta\lambda_0} \tag{4.1}$$

where λ_0 is the wavelength at which the spectral resolution is measured and $\Delta\lambda_0$ is the wavelength interval of the full width at half maximum of a calibration band. In other words, $\Delta\lambda_0$ is the smallest difference in wavelengths that can be distinguished at λ_0. The conversion between R_{ref} and R_i, the spectral resolution at λ_i is given by

$$R_i = R_{ref} \times \frac{\lambda_{ref}}{\lambda_i} \tag{4.2}$$

For a photon, the measure of its energy by the MKID detector is a Gaussian around its true energy (Dodkins et al., 2020). Assuming no bias in the energy measurement, the probability of measuring the photon at a given energy $P(E_\gamma = E)$ is the same as the probability of receiving a photon at that same energy $P(E_\gamma \text{ meas. at } E)$. Using Bayes' theorem (Hughes and Hase, 2010), we can consider the distribution of photons at the measured energy to be a Gaussian distribution determined by the spectral resolution around that wavelength. For each colour j in our bandwidth, the bands are then defined by the full width at half maximum of the Gaussian distribution around a wavelength λ_j. The value of R_j is approximated to be close to R_{j-1}. The list of colours is computed using the following algorithm.

Algorithm 1 Empirical algorithm to get a list of colours detected by an MKID for a spectral resolution R_{ref} at wavelength λ_{ref} for the considered bandwidth $[\lambda_{min}, \lambda_{max}]$

$R_{min} \leftarrow R_{ref} \times \lambda_{ref}/\lambda_{min}$
$\lambda_0 \leftarrow \lambda_{min}(1 + 0.5\, R_{min})$
$R_0 \leftarrow R_{ref} \times \lambda_{ref}/\lambda_1$
$Colour_0 \leftarrow [\lambda_{min},\ \lambda_0(1 + 0.5/R_0]$
while $\lambda_j < \lambda_{max}$ **do**
    $\lambda_j \leftarrow \lambda_{j-1}(1 + 1/R_{j-1})$ ▷ Separation of 1 FWHM
    $R_j \leftarrow R_{ref} \times \lambda_{ref}/\lambda_j$
    $Colour_j \leftarrow [\lambda_j - 0.5\lambda_{i-1}/R_{j-1}),\ \lambda_j + 0.5\lambda_j/R_j]$
end while

Figure 4.1 shows the number of colours we can then expect for a given R at 400 nm using that Algorithm 1. If we take the example of MEC (Walter, 2019) and its $R = 5$ at 980 nm, which means $R = 12$ at 400 nm, we can count 8 colours for a bandwidth between 500 nm and 1700 nm as illustrated Figure 4.2. We therefore use this value for the number of colours detected when simulating an end-to-end AO system with a MKID-based PWFS.

The measurement accuracy of the wavelength of a photon depends on the spectral resolution of the detector. Figure 4.14 shows the spectral distributions for wavelengths of 730 nm and 1190 nm, with spectral resolutions of 5, 12, and 20.

It is evident that a low spectral resolution could induce errors in the attribution of

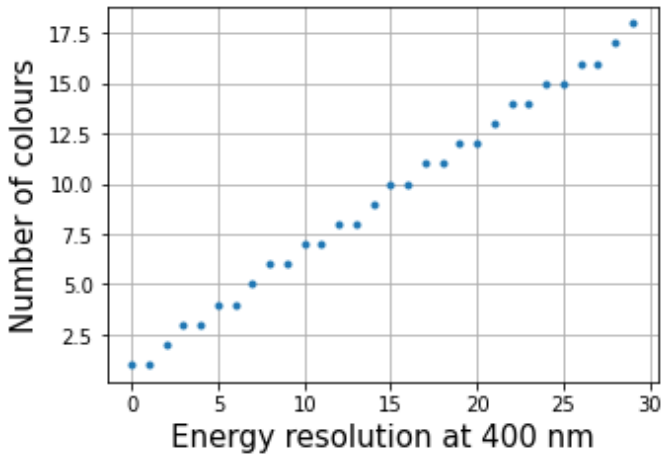

Figure 4.1: Optimized number of PWFS$_\lambda$ channels as a function of the spectral resolution at 400 nm for a bandwidth between 500 nm and 1700 nm

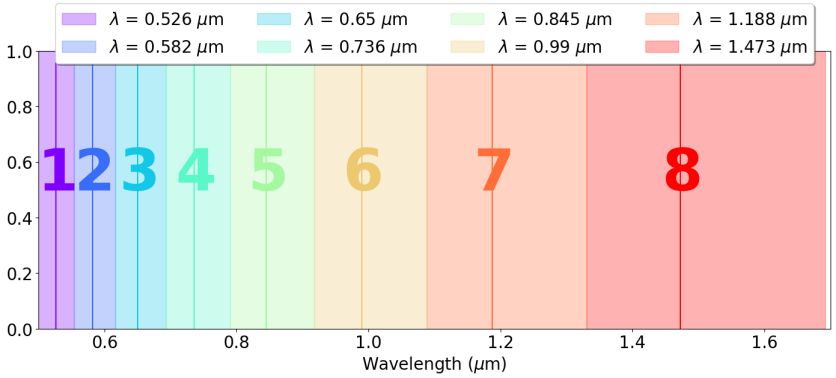

Figure 4.2: Colour decomposition using Algorithm 1 for a spectral resolution of 12 at 400 nm for a bandwidth between 500 nm and 1700 nm.

a photon to a waveband. Examining figure 4.2, the photons at 730 nm and 1190 nm should be assigned to bands 5 and 7, respectively. With a spectral resolution of 5, both photons could be measured at the same wavelength and attributed to the same waveband (5, 6, or 7). When the spectral resolution is 12, as considered in this study, both photons are distinguishable from each other but could still be attributed to band 6. At a spectral resolution of 20, the photon at 1190 nm could still be attributed to band 6. This phenomenon is referred to as colour confusion, which occurs when a photon is incorrectly attributed to a band.

To facilitate our study, this phenomenon is not taken into account and all measurements are made at a single wavelength, the central wavelength of the band.

4.1.2 Polychromatic reconstruction algorithm

Figure 4.3 is a diagram showing the method of polychromatic reconstruction implemented in Soapy and studied in this chapter. The method involves concatenating the slopes measured by PWFS$_\lambda$ channel to create a larger interaction matrix. This matrix is then inverted using the Monro-Penrose pseudo-inverse (Campbell and Meyer, 1991) to produce the control matrix for the MKID-based PWFS system. This approach was developed to incorporate all the chromatic measurements in the reconstruction process.

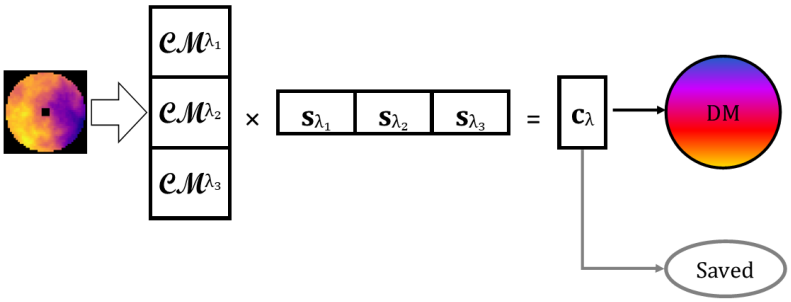

Figure 4.3: Diagram of reconstruction algorithm integrated into Soapy. All the PWFS$_\lambda$ signals are concatenated, increasing the size of the slope vectors. We then have a single $\mathcal{CM}$ and a single reconstruction taking all the signals into account.

4.1.3 Simulation parameters

Throughout this chapter, we plot the different behaviour of different PWFS$_\lambda$ channels. We define in table 4.1 the parameters common to all of the simulations used to generate these curves. We note that we are using a "perfect" deformable mirror capable of exactly reproducing each phase screen applied and the modal decomposition used here are the KL modes (see section 2.1.3.2).

We note here that thanks to the MKID superconducting properties, the energy of the incoming photons is significantly higher than the noise in the detector. The result is a zero read noise detection of each photon. Furthermore, we assume that we are only considering faint targets. We thus ignore any MKID saturation

phenomenon due to the number of photons incident on an individual MKID pixel (as described in section 2.4.2). Each incident photon is therefore considered to be detected individually.

Parameter	value
Telescope Diameter	8 m
Frame rate	1 kHz
Imaging wavelength	1.65 μm
PWFS pupil sampling	40 pixels
KL modes	500
Closed-loop gain	0.6
Latency	1 frame
Read noise	0
Spectral resolution at 400nm	12

Table 4.1: List of the parameters used by the PWFS model throughout this chapter. This system is based on the SAXO/SPHERE AO system (Sauvage et al., 2016).

Table 4.2 shows the two parameter values expressed as a function of the wavelength

The Fried parameter r_0 : This parameter is dependent on the wavelength (Fried, 1966). As the AOtools package generates the atmospheric phase screens for a r_0 at 500 nm, we use the following expression to transpose its value at a given wavelength λ using equation 2.10:

$$r_0(\lambda) = \left(\frac{\lambda}{500 \text{ nm}}\right)^{(6/5)} \times r_0(500 \text{ nm}) \tag{4.3}$$

Modulation radius : The PWFS modulation radius is often expressed in λ/D unit in the literature since the impact of the modulation is related to the operation wavelength (Vérinaud, 2004). As the MKID-based PWFS has several PWFS$_\lambda$ channels operating with the same physical modulation, we here express the modulation radius in arcseconds. Table 4.2 is presented here for ease of the conversion between the two units.

Parameter	Fixed values	500 nm	1000 nm	1700 nm
Fried Parameter r_0		0.12 m 0.16 m 0.20 m	0.21 m 0.29 m 0.36 m	0.33 m 0.44 m 0.55 m
Modulation radius	0.04 arcsec 0.08 arcsec	6λ/D 12λ/D	3 λ/D 6 λ/D	2λ/D 4λ/D

Table 4.2: List of the wavelength dependent parameters used by PWFS_{500}, PWFS_{1000} and PWFS_{1700} and their r_0 relative values and modulation radius conversion in λ/D unit.

4.2 Linearity and sensitivity and wavelength

While the PWFS is highly sensitive, it is also affected by non-linear behaviour. One of the causes of this non-linearity is measurement saturation due to a limited dynamic range. To compensate for this, a PSF modulation is added at the top of the pyramid prism, increasing the dynamic range at the expense of sensitivity. In this section, we first discuss the effects of wavelength on linearity by comparing the behaviour of two PWFS_λ. In the second step, we look at the linear behaviour of a PWFS with two PWFS_λ channels.

4.2.1 Chromatic dependence of the linearity-sensitivity trade-off

We start by investigating the behaviour of the PWFS at two wavelengths, 500 nm and 1000 nm, independently. First, we study the evolution of the dynamic range as shown in Figure 4.5. KL modes 0, 10, 50 and 160, shown in Figure 4.4 have been reconstructed at two different modulation amplitudes for the two PWFS_λ channels. The modes have been selected as a variety of spatial frequencies. To obtain the linearity curves in Figure 4.5, we give as input phase screen the modes shown in Figure 4.4 with increasing amplitude to the input of each PWFS_λ. We

then measure the reconstructed amplitude of that given mode.

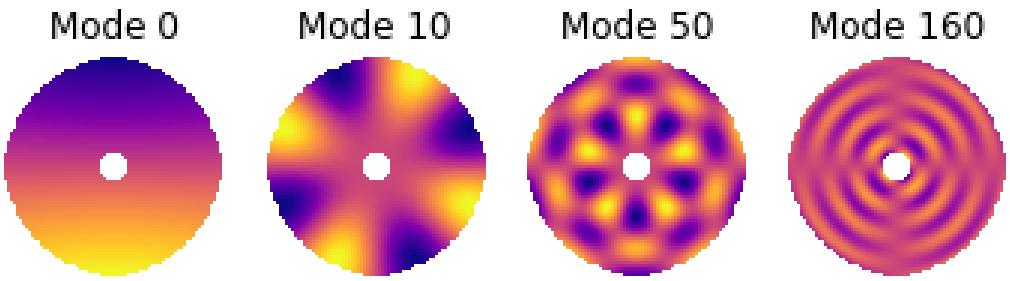

Figure 4.4: KL modes used for the linearity study presented in this section

As expected, saturation is observed when the amplitude reaches a critical value. For mode 0, tilt aberration, this value is equivalent to the modulation radius expressed in λ/D unit. For the same modulation radius, PWFS_{1000} offers a wider dynamic range. But when expressed in λ/D unit, when the modulation radius has the same value, PWFS_{1000} and PWFS_{500} have the same dynamic range. The results are coherent with those shown in the literature (see section 2.3.2.1), where we demonstrate that the impact of modulation is linked to the ratio between the modulation amplitude and the size of the PSF. As the spatial frequency increases, the impact of modulation decreases, with only the wavelength maintaining an impact for high-order modes.

Alternatively, we can look at the sensitivity value to characterise the performance of the PWFS. To do this, we look at the sensitivity curve expressed as a function of the slope vector $\vec{s}$, using the following equation (Deo et al. (2018)), for each mode ϕ_μ we have:

$$\xi(\phi_\mu) = ||\vec{(}s)(\phi_\mu)||_2 = \sqrt{< \vec{(}s)(\phi_\mu)|\vec{(}s)(\phi_\mu) >} \tag{4.4}$$

where $||.||_2$ represents an average and $\xi(\phi_\mu)$ describes the sensitivity of the mode μ, with higher values indicating a higher sensitivity. Figure 4.6 shows the sensitivity curves for PWFS, at the given modulation radius. As expected, we note the inverse trend in linearity, with PWFS_{1000} more sensitive than PWFS_{500}.

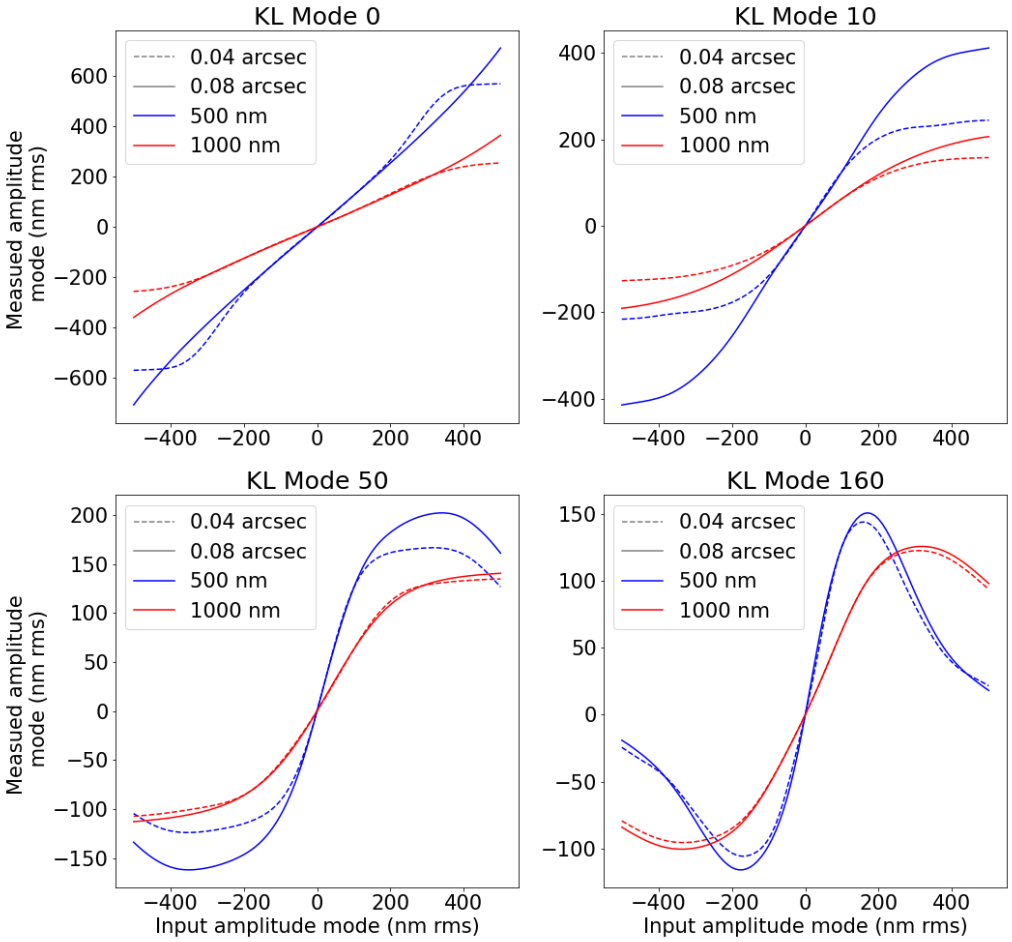

Figure 4.5: Linearity curve for PWFS_{500} and PWFS_{1000} with modulation radius 0.019 and 0.0386 arcseconds for KL modes 0, 10, 50 and 160. These curves were produced by applying a mode with different amplitudes to the input of each PWFS_{λ} and measuring the reconstructed amplitude of that given mode.

We can see that both PWFS_{λ} channels have complementary sensitivities and linearity ranges. Whilst the PWFS_{500} is more sensitive than PWFS_{1000}, the latter has a wider dynamic range. The capacity of the MKID-based PWFS to measure several chromatic channels therefore has the potential to bypass the linearity-sensitivity trade-off if the wavelength-dependent wavefront measurements can be combined.

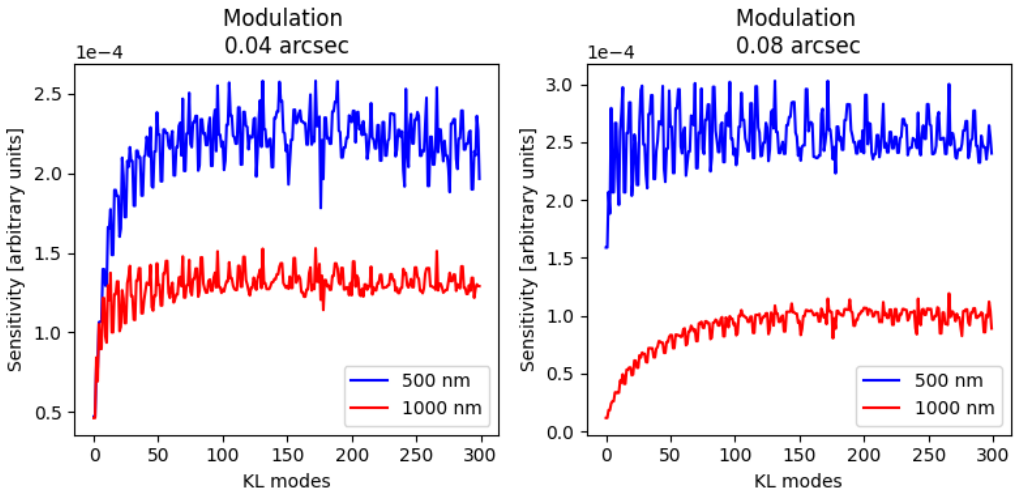

Figure 4.6: Sensitivity curves for PWFS_{500} and PWFS_{1000} with modulation radius 0.019 and 0.0386 arcsec for 200 KL modes. Curves were produced using equation 4.4

4.2.2 Polychromatic reconstruction

In this section, we analyse the impact of the reconstruction method on the dynamic range of the WFS presented in section 4.1.2 concatenating the two interaction matrices measured at each wavelength. To simplify the study we simulate only two PWFS_λ channels at 500 nm and 1000 nm. To match the physical modulation radius for the PWFS at each wavelength, we here have different radii in λ/D unit for each channel. We expect a different impact on the PWFS response due to the modulation than the ones for the PWFS_{500} and PWFS_{1000} individually. The results are compared with an average of the performance of each channel by averaging the curves presented in the previous section.

4.2.2.1 Linearity

Figure 4.7 displays the linearity curves for the polychromatic reconstruction and the averaging of the performance of the individual channels for modes 0, 10, 50 and 160. It is worth noting that at lower spatial frequencies, the linear range is smaller when both channels are simply taken into account in the reconstruction, compared

to the average performance of the individual channels. However, at lower spatial frequencies, there is no difference. Furthermore, the linear slopes around 0 overlap, indicating similar sensitivity in the presence of small aberrations.

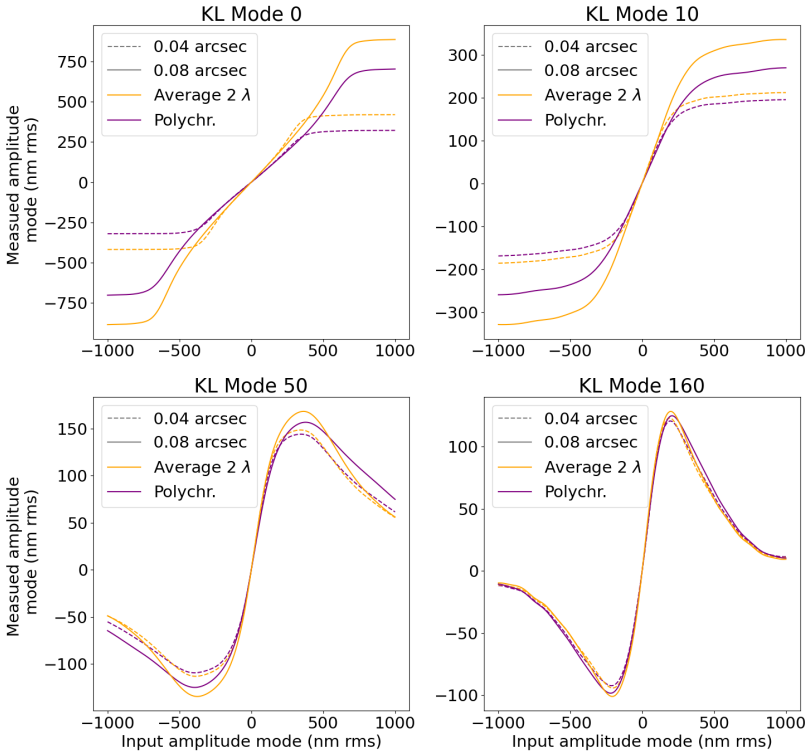

Figure 4.7: Linearity curves using a polychromatic reconstruction with $PWFS_{500}$ and $PWFS_{1000}$ channels and an average of the linearity curves presented in the previous section.

4.2.2.2 Sensitivity

Figure 4.8 shows the sensitivity curves for both the polychromatic reconstruction and the averaging of the performance of the individual channels. We can see similar sensitivity on a global comparison. There is a slight improvement in sensitivity for the polychromatic reconstruction in the lower modes. This shows that the trade-off between sensitivity and linearity, although less obvious, is still there and combining both measurements increases the sensitivity of the WFS.

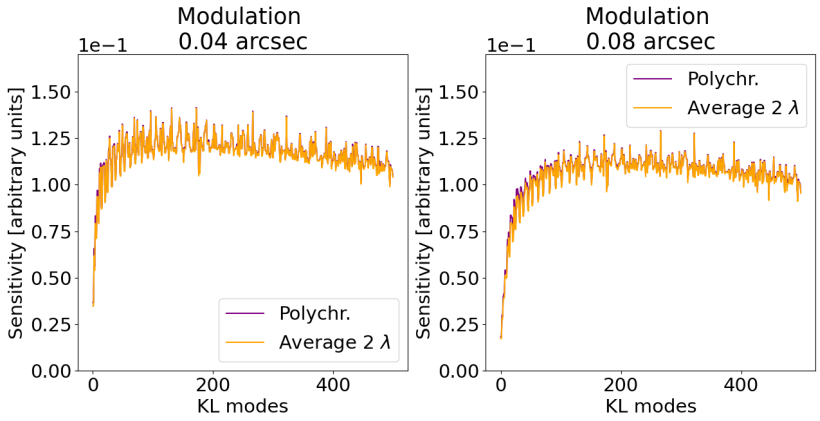

Figure 4.8: Sensitivity curves using a polychromatic reconstruction with PWFS_{500} and PWFS_{1000} channels and an average of the Sensitivity curves presented in the previous section.

4.2.3 Discussion

The performance of the PWFS is impacted by a trade-off between measurement accuracy, sensitivity, and the range of amplitude it can measure, the linearity range. This trade-off is evident in the performance of individual PWFS_λ channels. While the PWFS is more sensitive when operating at shorter wavelengths, it has a larger dynamic range at longer wavelengths.

We tested a reconstruction method that involves two PWFS_λ channels in the wavefront reconstruction. This method has a similar sensitivity and linear range than in average performance of both channels at higher modes, with slightly higher sensitivity and a smaller linear range at lower modes. This suggests that the measurement of the wavefront at a longer wavelength dominates the modal reconstruction of the wavefront. However, this reconstruction method does not overcome the trade-off, and further investigation is required to develop a more optimized reconstruction method.

4.3 Chromatic behaviour of the optical gain

To enhance the performance of the global MKID-based PWFS, we can improve the performance of the individual PWFS$_\lambda$ channels. As a first step towards compensation, we aim to understand the variations of the optical gains within these channels. In this section, we examine the optical gain variations for different atmospheric conditions in one channel (i.e. a single wavelength) and then generalise to multiple channels.

4.3.1 Optical gain r_0 dependence

We start by describing the optical gain variation under different atmospheric conditions. We fix our wavelength at 500 nm and the modulation radius at 0.08 arcseconds. We first calculate the optical gain, using the convolutional model, using full atmospheric phase screen. We then look at the improved AO performance by calculating optical gain curves using the fitting error PSF, and then residuals PSF generated with Soapy.

4.3.1.1 Optical gains for non corrected atmosphere PSF

Figure 4.9 shows the variation of the optical gain curves at different wavelengths. It can be seen that as the seeing conditions improve, the optical gains increase. This is to be expected, as the gains are directly related to the amplitude of atmospheric wavefront perturbations (Korkiakoski et al., 2008).

4.3.1.2 Fitting error and residuals PSF

The goal of an adaptive optics system is to flatten the wavefront, thereby reducing the residual RMS wavefront error to be as close to zero as physically achievable. Chambouleyron et al. (2020) shows that a system similar to the one described by

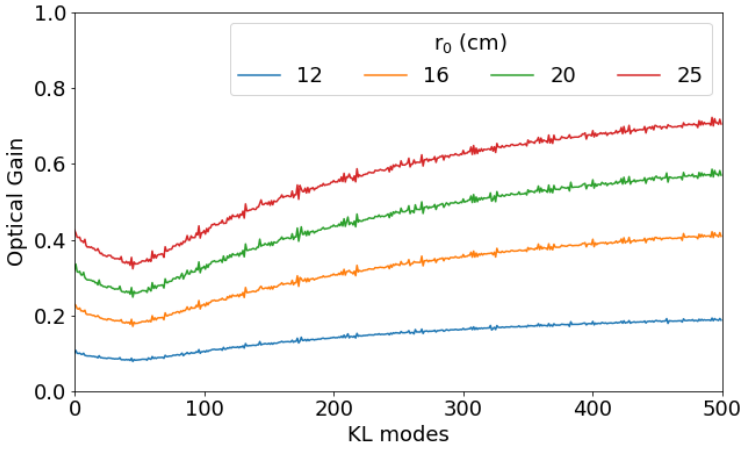

Figure 4.9: Optical gain curves computed using the convolutional model for different atmospheric conditions using atmospheric phase screens generated by the `AOtools` package. Each curve is a mean of 5 optical gains computations using the parameters described in Table 4.1

the parameters presented Table 4.1 tends to be dominated by the fitting error. To be complete, by considering only the fitting error will be better than in the real system, so the expected optical gains will be slightly lower. During high-performance AO operation, eg. with an XAO system, it is expected to reach a wavefront error close to the DM fitting error. For this reason, we describe here the optical gain in 2 regimes both the residual and the fitting error only.

Obtaining the fitting error PSF To generate the fitting error PSF we need to eliminate any other source of error. To this end, we need to generate perfect residuals in the DM modal base. We first generate an interaction matrix made up of the modes themselves as slope vectors, here the KL modes. This "perfect" interaction matrix represents exactly the modal decomposition of an input phase screen in the DM space. An atmospheric phase screen with the given atmospheric conditions (or r_0) is then generated. We subtract this atmospheric phase screen from its "perfect" reconstruction to obtain the fitting error residual.

Obtaining the residual PSF The generation of corrected wavefront residuals requires running the end-to-end simulation using the diffractive model. This means calibrating each PWFS_λ channel, calculating an interaction matrix for each wavelength. The end-to-end simulation must then be run in closed loop with enough iterations for performance to stabilise. Although this method is more physically accurate, it requires significantly more computing operations than generating the fitting error-only PSF.

Figure 4.10 shows the optical gains curves computed for both the wavefront residuals and the fitting error-only PSF. For comparison, we have also added the optical gains curve computed for a full uncorrected atmosphere PSF. We can see that for SAXO/SPHERE-like AO system, both the fitting error optical gains curve and residual optical gains curves match within less than 0.5% for all 4 r_0 values. We confirm that optical gains increase as atmospheric conditions improve or by closing the loop and reducing residuals. This shows that there is a direct relationship between the level residual AO correction and the optical gains value. The results are consistent with Chambouleyron et al. (2020). We can then use the fitting error PSF to reduce computation time.

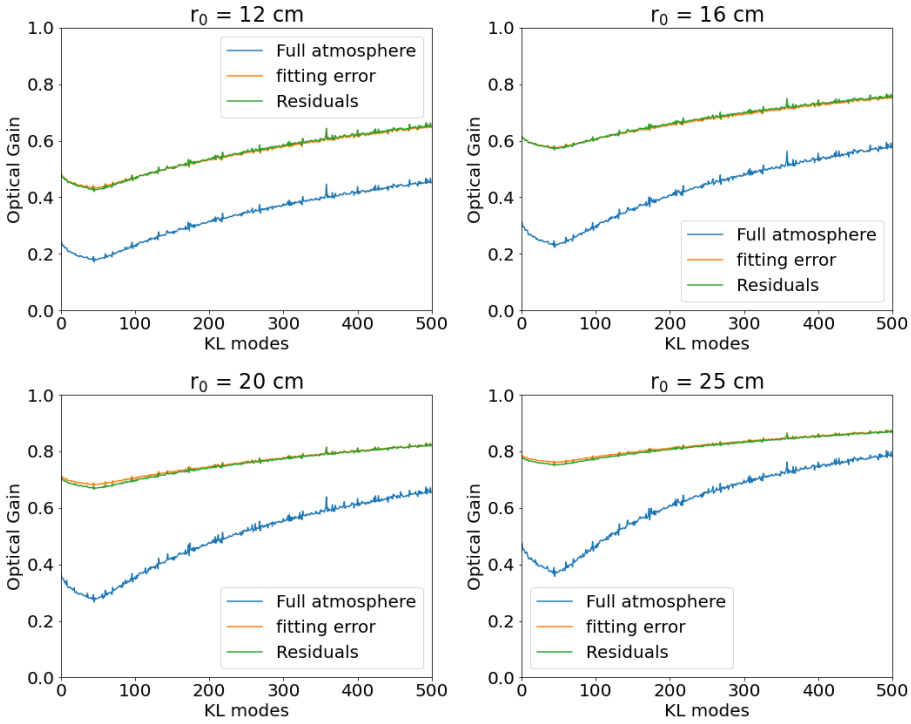

Figure 4.10: Optical gain curves computed using the convolutional model using AO residual, fitting error only and full atmospheric perturbation PSF at different r_0 values. Each curve is an average of 5 optical gain computations using the parameters described in Table 4.1.

4.3.2 Chromatic optical gain variation

We now look at the chromatic dependence of the optical gains. Figure 4.11 shows the PSF optical gain curves within each PWFS_λ channel. For each plot, the curves are computed using the convolutional model for a given atmospheric condition and a fixed (in physical units of arcseconds) modulation radius. We can see that both parameters have an impact on the optical gain mean value and spatial frequency variation. First of all, the wavelength changes the height of the optical gains curve as the r_0 changes at different wavelengths. Secondly, for a given wavelength the characteristic optical gains inflection point moves for different modulation amplitude without shifting the overall height of the curves. The inflexion point moves also with the wavelength.

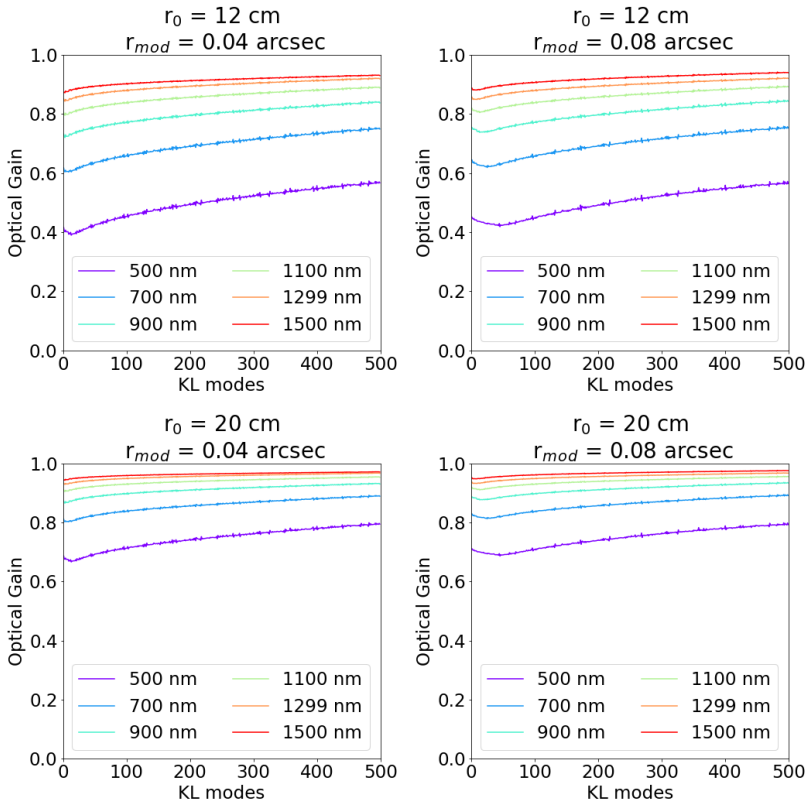

Figure 4.11: Each plot shows optical gain curves computed using the convolutional model using fitting error PSF at different wavelengths for different r_0 of 12 cm and 20 cm at 500 nm and different modulation radii of 0.04 and 0.08 arcseconds Each curve is an average of 5 optical gains computations using the parameters described in Table 4.1.

Figure 4.12 shows the same plots but with the modulation expressed in λ/D unit. This time, the inflexion point shifts from one modulation radius to the other but does not vary with the wavelength. This shows that the impact of the modulation, when expressed in λ/D unit, is similar to the dynamic range as studied in section 4.2.

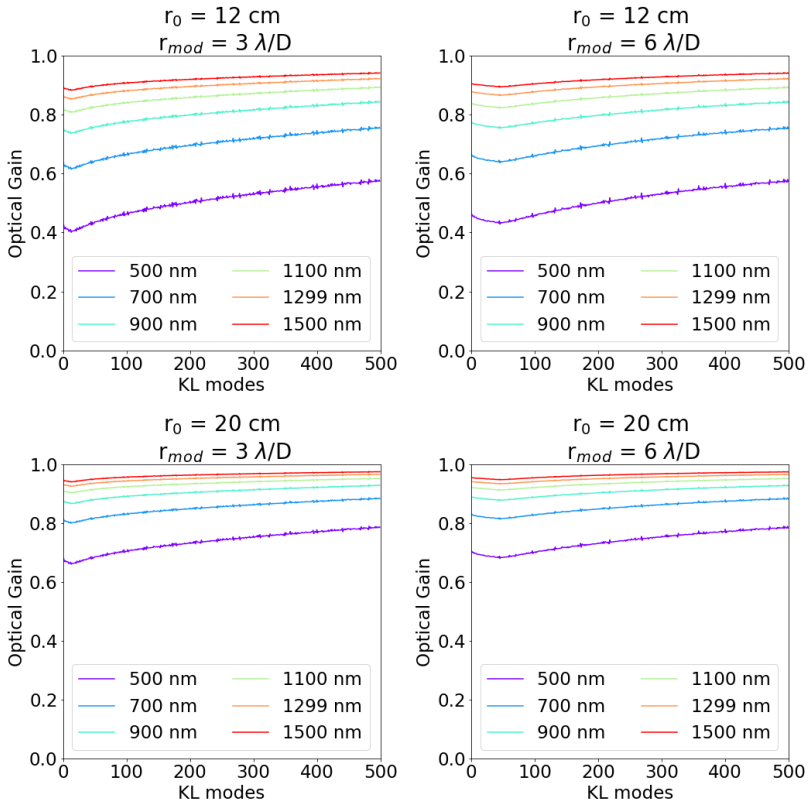

Figure 4.12: Each plot shows optical gain curves computed using the convolutional model using fitting error only PSF at different wavelengths for different r_0 of 12 cm and 20 cm at 500 nm and different modulation radii of 3 and 6 λ/D. Each curve is an average of 5 optical gains computations using the parameters described in table 4.1.

It is also interesting to note that, for a given spatial frequency, the chromatic variation of the optical gains varies with the value of r_0. To illustrate this, we plot figure 4.13 the optical gains variation with the wavelength for four modes, showing how this variation changes with spatial frequencies. We notice that the chromatic behaviour is different depending on both the atmospheric condition and the spatial frequency. The ratio between the gains at $r_0 = 12$ cm and $r_0 = 20$ cm at shorter wavelengths is greater than the ratio at longer wavelengths. From this, we can conclude that the optical gains are function of the spatial frequency, the wavelength, the atmospheric conditions and modulation amplitude.

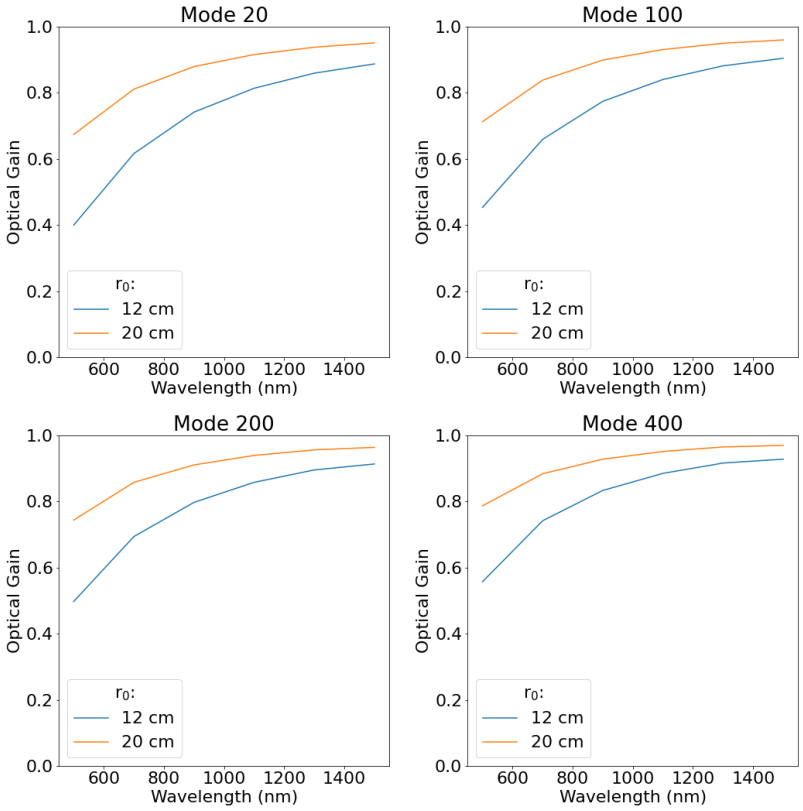

Figure 4.13: Each plot represents, for a given KL mode, the optical gain variation at a different wavelength for r_0 of 12 cm and 20 cm at 500 nm and different modulation radius 0.04 and 0.08 arcseconds. Each curve is an average of 5 optical gains computations using the convolutional model and the input parameters described in Table 4.1

4.3.3 Impact of the energy resolution

To simplify our model, we consider the channels as wavelengths rather than wavebands, ignoring any uncertainty in the measurement of the photon's energy. This section discusses an initial quantification of uncertainty in optical gain measurement.

Section 4.1.1 showed that the spectral resolution of the detector determines the uncertainty in the measurement of the wavelength of a photon. However, it is unclear how this impacts the measurement of optical gains. To investigate, we examined the optical gain dispersion around the optical gain curves at the real wavelength, shown in Figure 4.14, for spectral resolutions of 5, 12 and 20, using two photons at

730 nm and 1190 nm. As expected, the figure illustrates a decrease in dispersion around the real curves as the spectral resolution improves. As mentioned in section 4.1.1, the probability of measuring a photon at a given energy is equivalent to the probability of receiving a photon at that same energy. Therefore, we can assume that the distribution shown in Figure 4.14 is realistic.

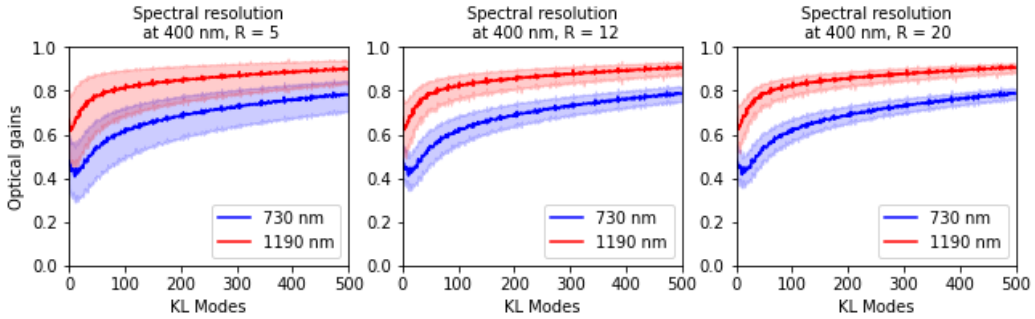

Figure 4.14: Optical gain curves computed with the convolutional model around a fitting error PSF for wavelength 730 nm and 1190 nm, and averaged over 50 independent phase screens. The bands around the curves correspond to the optical gain amplitude for the wavelength determined by the full-width half maximum shown in Figure **??** for spectral resolution of 5, 12 and 20.

To quantify the uncertainty of the optical gain measurement, we compare the optical gains for the central wavelength of the band with those at the edges of the band, considering the worst-case scenario. Figure 4.15 shows the uncertainties found as a function of the spectral resolution R. We can see that for R = 12, the uncertainty of the optical gain due to the uncertainty of the measure of the photon energy has a maximum of 10 percent.

For comparison, we take the example of HARMONI, an ELT instrument. Its requirements in terms of contrast are a flux ratio between the planet and the host start of 10^{-6} located at 0.2" from it (Jocou et al., 2022), while PCS requires to be able to detect a planet with a flux ratio of 10^{-9} at 0.1" from its host star (Kasper et al., 2010).

The HARMONIPWFS takes a waveband from 700 nm to 1000 nm (Schwartz et al., 2020). If it was a band of our system, it would mean a spectral resolution of 6.02 using the equations 4.1 and 4.2. We plot its value on the graph presented in

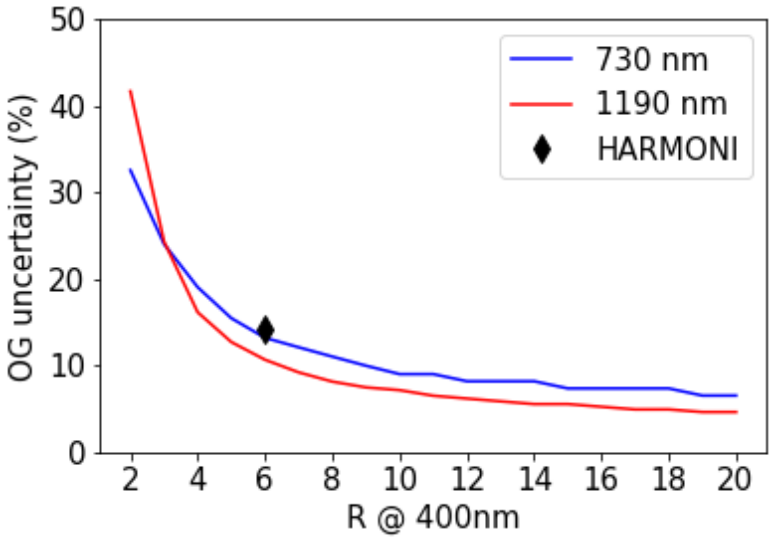

Figure 4.15: Evolution of the error on optical gain for photon at two given wavelength. The "HARMONI" value is computed considering the PWFS form the HAMONI instrument and the waveband considered of 700-1000 nm

Figure 4.15. We can see that the distribution of optical gain within the waveband considered by HARMONI is 15 percent and the MKID energy resolution considered here performs better.

4.3.4 Discussion

The optical gains are the quantity that represents the underestimation of the amplitude of modes during the modal decomposition of the wavefront performed by the AO system. This section has studied the variation of these gains as a function of 3 parameters: spatial frequency, atmospheric conditions and wavelength. The integration of an MKID within a PWFS-based AO system allows chromatic information to be added to the wavefront measurement, making the study of the chromatic behaviour of the optical gains highly relevant.

It has been observed that, for a given mode, the optical gain value varies chromatically, and this variation is dependent on atmospheric conditions. MKIDs have an energy resolution capable of having as many $PWFS_\lambda$ channels as were present throughout this section. Although the photon energy measurement error is not

integrated into the simulation, we have determined a maximum uncertainty of 10 percent in the optical gain measurement with the spectral resolution of 12. Moreover, this can be improved by increasing the number of photons attributed to the channel. It is possible to track this variation in the wavefront measurement through all channels.

4.4 Photon level and polychromatic reconstruction

This section aims to understand the impact of SNR on each channel by measuring the quality of the reconstruction as a function of photon level. To better understand the response of the PWFS as a function of wavelength, we will focus on studying the behaviour of two wavelengths: 500 nm and 1700 nm. Note that the work presented in this section has been previously presented in Magniez et al. (2022).

The choice of these wavelengths covers the expected wavelength range possible with an MKID-based PWFS. At shorter wavelengths, the light would start to be absorbed by the atmosphere and at longer wavelengths the sky background would begin to dominate the photon incident flux. It is also worth noting that due to the intrinsic sensitivity of the detector material (typically silicon or HgCdTe) observation across this passband would not be optimal or even possible using a single CCD. The wide wavelength sensitivity of the MKID allows us to take advantage of the possibility of measure the wavefront in the infrared and the visible simultaneously.

We have seen in the previous section that the impact of the modulation amplitude on the PWFS behaviour depends on its ratio to the full width half maximum of the PSF. It is therefore necessary to choose the modulation amplitude so that both PWFS_{500} and PWFS_{1700} can achieve good performance. Here, the amplitude modulation is selected according to the trade-off between sensitivity using small modulation, and linearity using large modulation. Bond et al. (2020) have shown that modulation radii of 2 to $4\lambda/D$ allow to reach good performance for a PWFS operating in the H-band. Choosing those values for 1700 nm corresponds

to modulation radii of 6 and $12\lambda/D$ at 500 nm, therefore we use those values in our simulations. The wavelength-dependent value of the Fried parameter at 500 nm and 1700 nm is shown in Table 4.2 along with the modulation radii in λ/D and on-sky angular units.

One of the goals of using an MKID is to take advantage of the wider possible passband to have the possibility to use fainter natural guide stars. We are therefore interested in the performance of the PWFS as a function of the incoming photon flux or stellar magnitude. For the calculation of the magnitude, we do not consider any particular stellar spectrum but set the photon flux on the $PWFS_{500}$ and $PWFS_{1700}$ to be equal. However, we have seen in Section 2.3.2.2 that the passband around 500 nm where dispersion remains below ± 0.1 pixels can be considered narrower than the one around 1700 nm. We accept this method of calculating magnitude as a simplification, knowing that for a stellar spectrum, the photon flux is typically lower in the infrared than in the visible for most bright guide stars. Figure 4.16 shows the conversion between the magnitude and the photon flux used for this section for reference.

4.4.1 Comparison of $PWFS_{500}$ and $PWFS_{1700}$ performance

To understand how to take advantage of wavefront information measured in different wavebands, it is first necessary to examine the performance of the PWFS at each wavelength. In Figure 4.17, we look at the Strehl ratio of $PWFS_{500}$ and $PWFS_{1700}$ with an AO-corrected science image at 1650 nm as a function of magnitude. There are two distinct performance zones. There is a high plateau of the Strehl ratio at bright magnitudes, i.e. high photon flux, where the photon noise is negligible. A reduction in performance is observed for stellar magnitudes above 11 as WFS noise starts to dominate AO system performance.

We observe that in the high flux regime, increasing the modulation amplitude and therefore the linear range improves the performance of the AO system. On the other

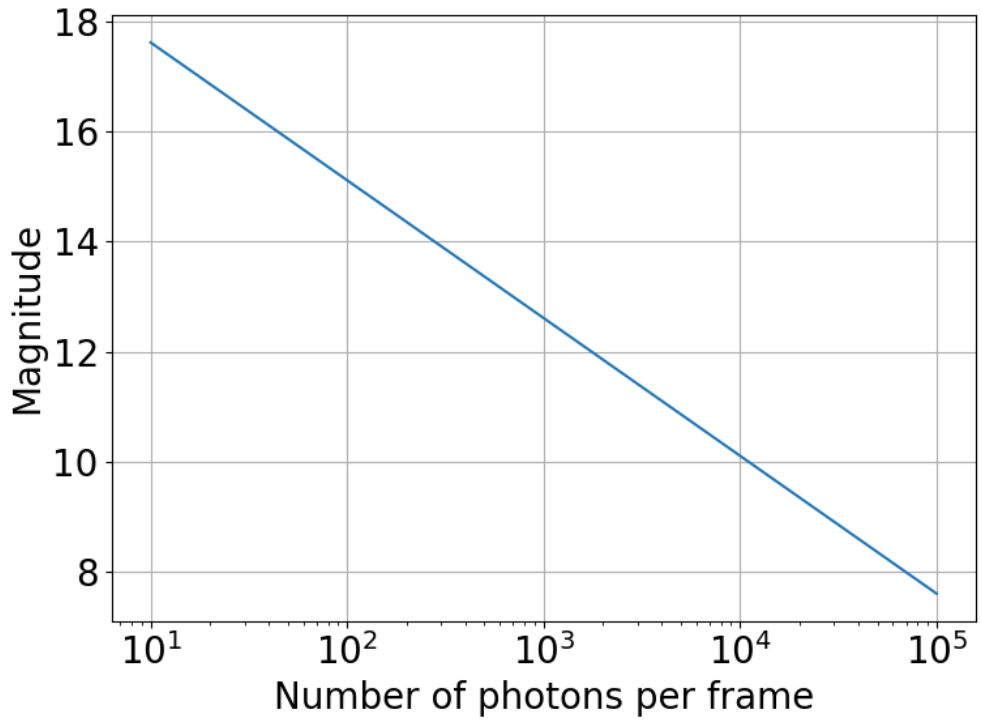

Figure 4.16: Conversion between magnitude and detected photon flux at the PWFS. The spectrum is set to be flat. The photon flux is computed for an 8 meter telescope and a throughput (including device Quantum Efficiency) of 0.2.

hand, in the low-photon regime, it is more advantageous to have a smaller radius of modulation. We also observe that the PWFS performs better at 1700 nm at high flux, whereas, operating at 500 nm allows us to use the PWFS at fainter magnitudes as the Strehl ratio measured for $PWFS_{500}$ decreases at higher magnitudes.

We also note that the PWFS performs better at 1700 nm with a high photon flux. To better understand this, we can refer to the previous section and look at the optical gain behaviour. We have seen that the optical gains improve (i.e. are closer to unity) with increasing wavelength. This explains the performance improvement.

As the magnitude increases, photon noise begins to dominate and a drop in performance is observed. The $PWFS_{500}$ then becomes more efficient. It can be explained by the fact that the amplitudes of atmospheric aberrations expressed in radian are smaller at 1700 nm than at 500 nm, consequently, the PSF is better corrected. The

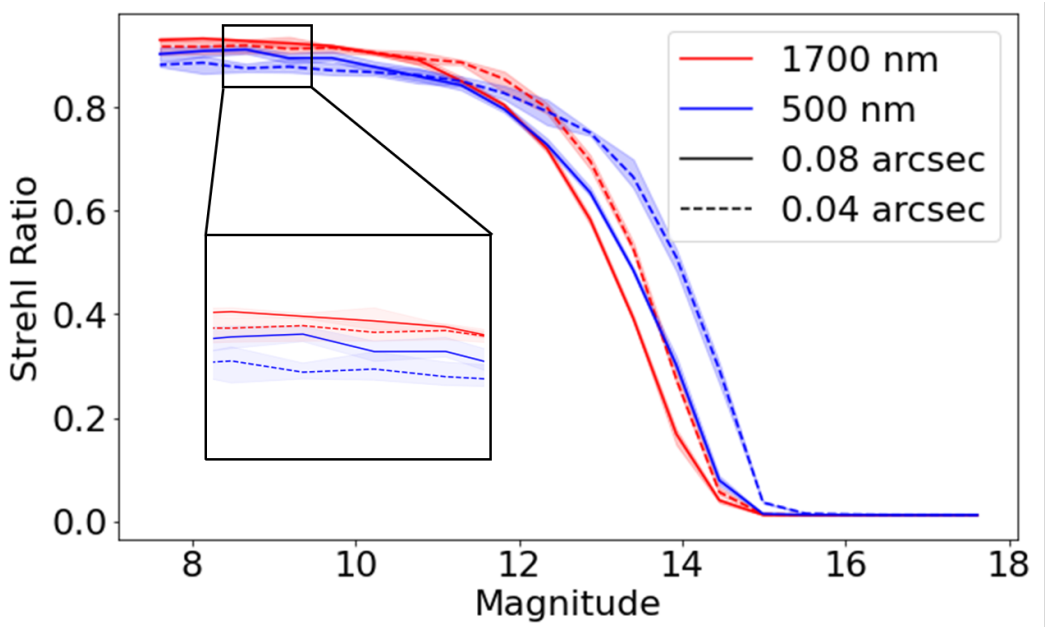

Figure 4.17: Strehl ratio of a PWFS with parameters from Tables 4.1 and 4.2 at 500 nm and 1700 nm for modulation radius of 0.04 and 0.08 arcseconds as a function of guide star magnitude. The curves represent the average of 4 different simulations with 4 atmospheres of the same generation parameters.

signal measured by the PWFS - that is the first derivative of the incoming phase - also has a smaller amplitude at 1700 nm and therefore is more easily hidden in the photon noise, which is constant between the two sensed bands in this simulation.

In the low flux regime, it is also more advantageous to use a smaller radius of modulation. We hypothesise that this is caused by the loss of sensitivity linked to extending the linear range: if the radius of modulation is bigger, a given signal translates into smaller amplitudes on the detector plane which are in turn more easily lost in noise. Further study is necessary to confirm this hypothesis.

Without trying to use both PWFS $_{500}$ and PWFS $_{1700}$ together, it can be seen that if a system was designed with two PWFS, one operating at 500 nm and a second at 1700 nm, we would gain approximately a half magnitude gain if we used the short wavelength PWFS when observing fainter guide stars assuming a number of incident photon identical attributed to each waveband. As we know, the stellar spectrum is not flat and depends on the type of star. In practice, there will be

differences in photon flux within each passband, dependent on guide star spectral type, MKID spectral resolution and instrumental and atmospheric throughputs. The exact magnitude gain would be dependent on each of these factors and would require a dedicated study for a given system. However, the half magnitude gain is indicative of the scale of gain that could be achieved when observing cooler guide stars with a flatter spectrum across the visible to NIR range. We note that all subsequent simulations presented within this thesis work in a high-flux, low-noise regime where the actual photon flux within each waveband does not impact the results or conclusions.

4.4.2 Polychromatic reconstruction

As we have seen in Section 2.3.2.2, a chromatic pupil dispersion of more than 0.2 pixels leads to a decrease in PWFS performance. Over a large waveband, the double pyramid design alone is not enough to verify the maximum 0.2-pixel dispersion. Without an energy-sensitive detector, the solution is to design an AO system with multiple PWFS operating at different wavelengths. This optical system, theoretically feasible for a limited number of wavebands, would be very complex to implement as opposed to the use of a single MKID array. MKIDs would allow us to combine wavelengths to improve performance and observe fainter stars by considering a wider range of wavelengths simultaneously.

Since we are considering the use of an MKID array, we can now consider the measure of the wavefront by both channels simultaneously. The detected stellar spectrum is widened, increasing SNR. In Figure 4.18, we present the channels at 500 nm and 1700 nm and associate them with the polychromatic reconstruction algorithm presented in Section 4.1.2. We plot the performance of both individual channels and the combined polychromatic reconstruction as a function of the stellar magnitude. By combining the two signals, a gain of one magnitude is achieved before the drop in performance due to the lack of photons. In the high photon flux regime, the

polychromatic reconstruction performs between both channels, indicating that the MKID-based PWFS system is impacted by the optical gains.

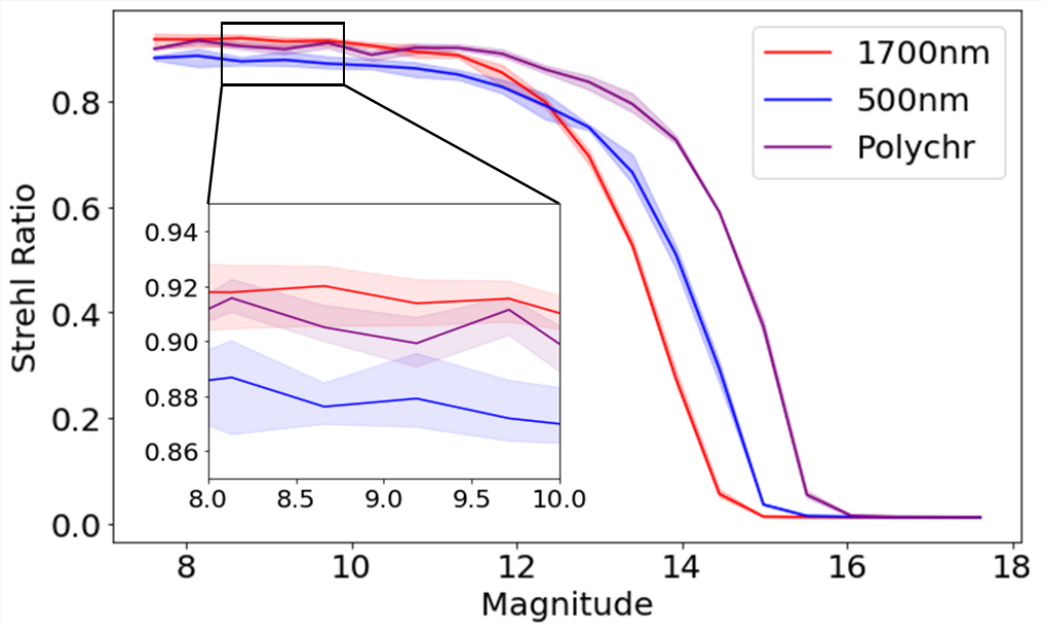

Figure 4.18: Strehl ratio as a function of guide star magnitude for the AO system with parameters shown in Table 4.1 and a PWFS operating at 500 nm and 1700 nm. The curves represent the average of 4 different simulations with 4 atmospheres of the same generation parameter.

4.4.3 Discussion

When using a non-energy sensitive detector for a PWFS detector, the spectral band considered for operation can be limited by the dispersion of the pyramidal prism. However, by integrating an MKID array to the WFS, we can overcome this limit and detect more photons from the same star. We evaluated the performance of two individual channels, 500nm and 1700nm, for varying photon flux. When plotting performance as a function of photon flux, two regimes were observed: high photon flux with stable high performance, and a drop in performance due to a decrease in the number of photons and SNR. In the high flux regime, longer wavelengths exhibit better performance due to being less impacted by the optical gain. Regarding the drop in performance, it happens at higher magnitudes at the

shorter wavelengths because the perturbations are stronger at lower wavelengths and therefore the SNR remains higher when the number of photons drops.

We then combined wavefront information from both channels to evaluate the performance of a simple polychromatic reconstruction. As more photons are detected, the broadening of the spectral band is shifted at higher magnitudes the drop in performance to fainter stellar magnitudes. In the high photon flux regime, the performance of the polychromatic reconstruction is between the performance of both individual channels. This indicates that the optical gain impact at lower wavelengths still affects the polychromatic reconstruction. As the system is aimed at observing fainter targets, the use of more channels is crucial, but to optimise the performance of the MKID-based PWFS, it is necessary to compensate for the optical gains for the channels operating at lower wavelengths.

4.5 Integration with the science instrument

This section examines the implications of integrating an MKID array into an AO system, focusing on two main consequences: detector saturation and the competition for photon resources between the wavefront sensor and the science instrument. From this, we seek to address two questions. First, is the recombination time short enough to enable high-performance wavefront sensing, and if not, what are the requirements? Secondly, it must be determined whether the MKID-based PWFS can operate effectively within the wavelength band ignored by the science instrument. Alternatively, it may be necessary for the science instrument to sacrifice some photons in order to achieve better contrast.

4.5.1 Saturation and decay constant

As previously discussed in Chapter 2 and more precisely Figure 2.7, MKIDs may experience saturation effects due to the recombination time, particularly if two

photons arrive on the same pixel within this recombination time. This section aims to determine the number of photons that can be detected per loop iteration, here fixed for a frame rate of 1kHz, given a specific constant decay rate, and to assess whether this detection rate is sufficient.

The pulses shown in Figure 2.7 have a recombination time of the order of 1 millisecond. If we consider only completely separated photon pulses, this results in one photon being detected per pixel per frame at a sample rate of 1 kHz, as illustrated in Figure 4.19. However, it is possible to detect and measure photons arriving within shorter intervals, although with less accurate energy measurements. It is therefore necessary to compare the number of photons required to meet the performance requirements of the AO system with the tolerances on energy measurement necessary to utilise the chromatic information advantage.

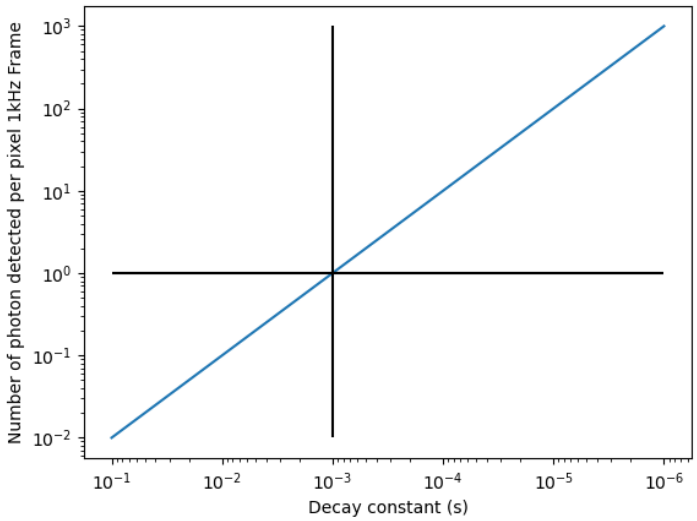

Figure 4.19: Number of photon detectable per pixel for a given recombination time at a frame rate of 1 kHz.

If we take Figure 4.18 and change the x-axis from magnitude to the number of photons per waveband, we obtain Figure 4.20. From Table 4.1, we can compute that the number of illuminated pixels per pupil image on the detector is around 5024. Considering the number of photons with distinctive pulses detected by the current performance of an MKID, we see that we can detect enough photons to

achieve high performance, as shown in the figure. Moreover, this can be further improved through software enhancements, such as implementing pulse detection algorithms that account for multiple photons arriving within the recombination time, although at the expense of energy measurement accuracy.

However, the multiplication of the wavebands under consideration may result in an increase in the number of photons required to be detected, contingent on the requirements of the system and the need to exploit the advantages of polychromatic measurements. As the potential of hyperspectral PWFS is explored, it becomes evident that the requirements for recombination time may vary. The recombination time can be adjusted by modifying the properties of the superconducting material and the temperature of the MKID (Mazin et al., 2002). However, shortening the decay of the pulse has an impact on the pulse analysis with a decrease in energy resolution. We then need to determine the minimum requirements of waveband discrimination to determine the possible decay constant and/or improve the photon analysis process.

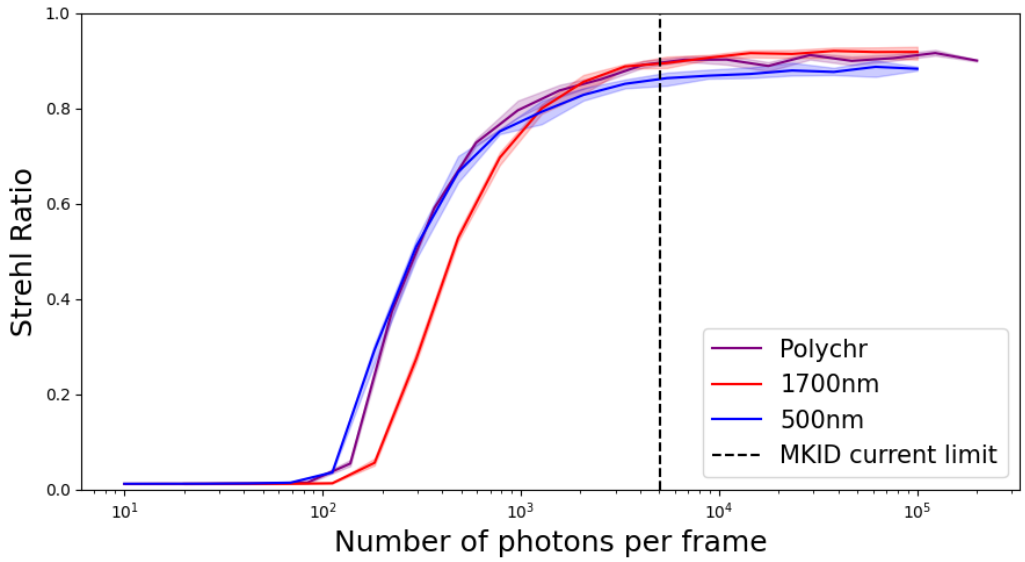

Figure 4.20: Strehl ratio as a function of number of photon per frame for the AO system with parameters shown in Table 4.1 and a PWFS operating at 500 nm and 1700 nm. The curves represent the average of 4 different simulations with 4 atmospheres of the same generation parameter. The MKID limit shown here correspond to a magnitude 11 following Figure 4.16

4.5.2 Photon distribution and waveband

The distribution of photons between the science instrument and the MKID-based PWFS is a crucial consideration when looking at the use of such extensive spectral wavebands for the wavefront sensor, at the expense of an instrument such as a spectrograph. This leads to a number of questions. Firstly, what is left for the wavefront sensor by the science instrument, and is this sufficient? Secondly, what is the energy resolution of the MKID used, and how many distinct bands can be achieved with this spare passband? Finally, it must be determined whether it is feasible for the science camera to share the waveband with the wavefront sensor, and whether this would be beneficial.

Given that the majority of spectral variations occur within the visible region of the electromagnetic spectrum, hyperspectral wavefront sensors are particularly suited to this area. Furthermore, the additional chromatic information provided by the detector enables effective compensation for non-linearities such as optical gains and saturation, which predominantly occur within this range. Additionally, the visible range exhibits a stronger signal, which could ensure the necessary number of photons for each waveband.

However, the PCS XAO WFS is planned to operate in the infrared, specifically in the I, Z, and Y bands (Kasper et al., 2021). The imaging would be conducted in the V, R, and I bands, while the spectrographs would be used in the R and I bands at low resolution and the J and H bands at high resolution. The choice of the wavebands of the WFS was made to be the closest to the science case. From this, we can infer that the B and G bands are free to be used. Moreover, the extensive range of wavebands allows for the flexibility offered by the use of an MKID array to be employed in optimising the correction, in accordance with the science case. Furthermore, previous studies have demonstrated that spare photons of the same waveband between the science instrument and the WFS can be advantageous for fainter targets, as illustrated in Figure 4.21. Ultimately, the photon distribution

can be reconsidered in light of the benefits of utilising a hyperspectral wavefront sensor. Furthermore, the flexibility offered by an MKID-based PWFS can still be utilised by considering only the bands on either side of the bands used by the imager.

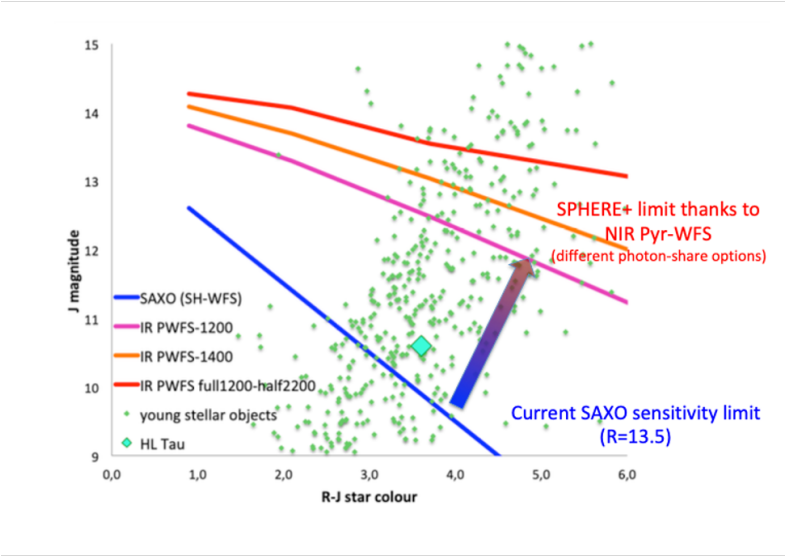

Figure 4.21: AO sensitivity limit gain thanks to an IR Pyramid sensor, as a function of the R - J target colour, for different assumptions of photon share (all NIR photons to the sensor up to 1.2, 1.4 μm or a 50/50 photon share in the 1.2 -2.2 μm range). This gain will enable access to many more faint, red Young Stellar Objects: green dots represent actual targets from nearby star forming regions, among which the well-known example of HL Tau (currently out of reach of SPHERE). From Boccaletti et al. (2020).

4.5.3 Discussion

The integration of an MKID array into an AO system introduces crucial considerations such as detector saturation and the competition for photons between the wavefront sensor and the science instrument. While the recombination time of an MKID is pivotal in this integration, it is important to recognize its adjustability through modifications to MKID properties, aligning it with the requirements of the system. Another crucial question pertains to the photon distribution, which is a prerequisite for utilising an MKID array. This necessitates the sharing of the entire spectrum with a spectrograph. There are two potential avenues for achieving

this: either utilising only the available wavebands or sharing the spectrum with the science over a subset of bands. This sharing could potentially enhance the AO performance, thereby compensating for the loss of photons and improving the science. Furthermore, the flexibility offered by an MKID-based PWFS can be utilised by considering only the bands on either side of the bands used by the imager. In conclusion, integrating an MKID-based PWFS into PCS presents challenges contingent upon photon flux and final photon distribution considerations. Nonetheless, the adaptability of MKID technology offers solutions and will determine the requirements on the detector.

4.6 Conclusion

In this chapter, our main focus has been on exploring the chromatic behaviour of the PWFS. To achieve this, we carried out a detailed examination of individual PWFS_λ behaviours. We then analysed these behaviours using both channels, PWFS_{500} and PWFS_{1700}, for reconstruction. We investigated the effects of chromaticity on two sources of non-linearity and one source of noise, namely the trade-off between linearity and sensitivity due to measurement saturation, optical gains and photon levels.

Measurement saturation: The analysis indicates that the linearity range expands as the wavelength decreases while operating with the same physical modulation radius, as would occur in an MKID-based PWFS system. The effect of modulation on linearity depends on the modulation amplitude-wavelength ratio. Illustrating the well-known sensitivity-dynamic range trade-off of PWFS that sensitivity increases with wavelength. However, simultaneous operation at different wavelengths has the potential to overcome this trade-off. In the case of the polychromatic reconstruction used in this chapter, there has been no evidence of an improvement in the trade-off. Further study is required.

Optical gains: The optical gains are coefficients that express the underestimation of modal amplitudes caused by the atmospheric residuals during operation. The analysis presented in this chapter indicates that optical gains tend to be closer to 1 as the atmospheric conditions improve. Similarly, the optical gains increase with wavelength because the atmospheric perturbations are less impactful for a system operating at longer wavelengths. The optical gain curves as a function of the KL modes have a wavelength-dependent shape; the mode where the inflexion point occurs varies with the ratio between the PSF modulation amplitude and the wavelength. For a given mode, the variation of chromatic optical gains changes with atmospheric conditions. This demonstrates that adding a chromatic dimension to the measurement of the wavefront can improve our knowledge of atmospheric conditions and, by extension, provide information on the optical gains. As a polychromatic measurement of the wavefront has been little explored, this study is unprecedented. It offers new research perspectives such as the new method of optical gain tracking explored in Chapter 5.

Photon level: The objective of this work is to investigate the potential of an MKID-based PWFS in observing fainter targets. As the photon level decreases, the performance of a PWFS decreases as well. To address this issue, the solution is to collect as many photons as possible by widening the stellar spectrum detected. This can be achieved by using a MKID array, which overcomes the constraints imposed on the PWFS by the chromatic dispersion of the prism. This capacity of waveband discrepancy of a hyperspectral wavefront sensor allows for wavefront measurement over an unprecedentedly wide detected wavelength range de facto surpassing the SNRs achieved by PWFS so far. However, when using a polychromatic reconstruction, we have observed that the performance is still affected by the optical gains, which have a greater impact on the channels operating at shorter wavelengths. Therefore, compensation for these gains is necessary.

The potential integration of an MKID array within an XAO system was explored, with particular focus on the challenges posed by the saturation effect. This saturation occurs when multiple photons strike the same sensing element in quick succession. To mitigate this, adjustments can be made to the properties of the MKID, though this may result in a decrease in energy resolution. Alternatively, advanced software solutions can be employed, although this may lead to increased complexity. The optimal approach is likely to involve a combination of both strategies, with the final decision guided by simulation results determining the number of required bands.

Additionally, we discussed the distribution of photons between the WFS and the science instrument, such as the PCS. It is possible to either utilise only the wavebands available or share them with the science instrument across certain bands. This sharing can enhance AO performance, potentially compensating for the loss of photons by improving the overall scientific performance. The final decision will be influenced by the requirements of the instrument and the outcomes of future simulations.

The analysis in this chapter demonstrates that the PWFS performance can be improved by dividing the sensed spectra into several wavebands, increasing the SNR of the WFS. Moreover, it gives also an unprecedented insight into the PWFS behaviour by adding a dimension to the wavefront measurements. This could be achieved by dichroic dividing of the signal by using multiple detectors, multiple WFS or using an energy sensitive detector. However, the first two solutions can quickly become technically challenging and limited to a few wavebands. Thanks to detectors such as MKID arrays, it then becomes possible to consider new techniques involving hyperspectral wavefront sensing to overcome the problems discussed in this chapter.

CHAPTER 5

OPTICAL GAIN TRACKING METHOD

Chapter 4 showed that multi-wavelength wavefront sensing can improve performance, even with a simple reconstruction method by increasing the sensed waveband. However, the performances of the hyperspectral PWFS are impacted by optical gains, particularly for PWFS_λ channels at lower wavelengths. This chapter investigates whether performance can be further improved by tracking optical gains and compensating for them using the chromatic measurements of the wavefront.

Incorporating knowledge of the optical gain within the system control has already been studied (see e.g. (Deo, 2019; Chambouleyron et al., 2020).) However, existing approaches require additional components or are invasive, such as a gain scheduling camera that diverts some of the light away from the PWFS detector. The advantage of using an MKID as PWFS detector is that it provides additional information without requiring additional sensing devices. The dependence of the measured wavefront on wavelength then allows the statistics of atmospheric conditions to be retrieved. This provides the only unknown parameter in the system needed to calculate the expected optical gains using the convolutional model.

In this chapter, we present a technique that allows the estimation of r_0 from the chromatic distribution of the PWFS wavefront measurements. We then explain the methodology for building a dataset and provide details of the dataset used in the subsequent work. The model is then used to determine the value of r_0, which provides the essential statistics required for optical gain retrieval.

5.1 From chromatic wavefront measurement to r_0 fitting model

The objective of this model is to obtain the optical gains through an estimation of r_0. Section 4.3 demonstrates that the chromatic distribution of the optical gain is dependent on the atmospheric conditions quantified by r_0. By using an MKID-based PWFS, we can compute a modal decomposition of the atmospheric wavefront at several different wavelengths across a wide passband. By tracking the influence of the optical gains in those different chromatic modal reconstructions it becomes possible to **track the variation of r_0 without waiting for the modal variances over time using the Noll variances (Noll, 1976). This section outlines the successive steps of the method.**

5.1.1 Ratios distribution at different r_0

During operation, we are unable to access the optical gains directly. Instead, we have a modal decomposition measured by the wavefront sensor. Thanks to the energy sensitivity property of an MKID, we are able to measure the wavefront with multiple chromatic WFS channels, PWFS_λ. We define the true modal coefficient vector of the modal decomposition of the atmospheric wavefront as $\vec{c}$. In the simulation, this can be measured from the direct decomposition of the atmospheric phase into the modal basis, here KL modes. For a PWFS_λ channel operating at the wavelength λ, we define its coefficient vector of the modal decomposition $\vec{c}_\lambda$. By definition :

$$\vec{c}_\lambda = \vec{c} \times \vec{og}_\lambda, \tag{5.1}$$

where $\vec{og}_\lambda$ is the optical gain vector for the channel PWFS_λ.

We then consider two channels, PWFS$_{\lambda_1}$ and PWFS$_{\lambda_2}$, operating respectively at the wavelengths λ_1 and λ_2. By defintion:

$$\vec{c} = \frac{\vec{c}_{\lambda_1}}{\vec{og}_{\lambda_1}} = \frac{\vec{c}_{\lambda_2}}{\vec{og}_{\lambda_2}} \Rightarrow \frac{\vec{c}_{\lambda_1}}{\vec{c}_{\lambda_2}} = \frac{\vec{og}_{\lambda_1}}{\vec{og}_{\lambda_2}}, \tag{5.2}$$

where $\vec{c}_{\lambda_1}$ and $\vec{c}_{\lambda_2}$ are the coefficient vectors of the modal decomposition measured by PWFS$_{\lambda_1}$ and PWFS$_{\lambda_2}$ respectively, and $\vec{og}_{\lambda_1}$ and $\vec{og}_{\lambda_2}$ the optical gain vectors for the channels PWFS$_{\lambda_1}$ and PWFS$_{\lambda_2}$ respectively. This means we have a direct measure of the optical gain ratios within the reconstruction of the different PWFS$_{\lambda}$.

We define $R_{og}(\mu, r_0, \lambda)$, the optical gain ratio of the optical gains at λ over the optical gains measured at λ_0 for a given mode μ and for a given value of r_0. In a real system, we do not have access to $\vec{c}$, therefore we defined a λ_0 to be the wavelength that we can arbitrarily define within the analysis to be used as the denominator for all the optical gain ratios. Typically, we select λ_0 to be the longest wavelength available. This is because the optical gain is less sensitive to changes in r_0, and longer wavelength measurements have a higher optical gain value. We also define $R_{md}(\mu, r_0, \lambda)$ as the modal decomposition ratio of the modal decomposition measured at λ over the modal decomposition measured at λ_0, once again for a given mode μ and r_0. We then define the following quantities:

$$\left.\begin{aligned} R_{og}(\mu, r_0, \lambda) &= \tfrac{og(\mu, r_0, \lambda)}{og(\mu, r_0, \lambda_0)} \\ R_{md}(\mu, r_0, \lambda) &= \tfrac{c(\mu, r_0, \lambda)}{c(\mu, r_0, \lambda_0)} \end{aligned}\right\} \rightarrow R_{og} = R_{md}, \tag{5.3}$$

where $og(\mu, r_0, \lambda)$ is the optical gain values for a given mode μ and at a given value of r_0 for the channel PWFS$_{\lambda}$. $c(\mu, r_0, \lambda)$ is the reconstructed coefficient for the mode μ of an input atmospheric phase screen at a given r_0 value for the channel PWFS$_{\lambda}$.

The measure of $R_{og}(\mu, r_0, \lambda)$ is achievable due to the availability of multiple PWFS$_{\lambda}$ channels. Next, we must express R_{og} as a function of r_0 to get an estimated value

for r_0.

5.1.2 Fitting the chromatic distribution

Figure 5.1 shows the chromatic distribution of R_{og} calculated with the convolutional model for values of r_0 of 12 cm and 20 cm for 6 KL modes, demonstrating the dependence of R_{og} with spatial frequency. The wavelength λ_0 used for the denominator is 1490 nm. The number of wavelengths measured for the optical gains is intentionally high to obtain the most accurate equation for the model. The dashed line shows an empirically fitted model according to the following equation

$$R_{og}(\mu, r_0, \lambda) = 1 - \exp(-\mathrm{A}(\mathrm{r}_0, \mu)\lambda^{\mathrm{B}(\mathrm{r}_0,\mu)}) \tag{5.4}$$

where $A(r_0, \mu))$ and $B(r_0, \mu))$ are the fitting parameters determined for each chromatic distribution of the optical gain ratios for a given mode μ. Figure 5.1 clearly shows that the ratio curves $R_{og}(\mu, r_0, \lambda)$ for KL modes 2 and 10 display discontinuities. This can be attributed to the fact that the convolutional model does not correctly represent the lower modes (see chapter 3).

To prevent any repercussions caused by these discontinuities, we choose to reject the most affected lower modes from the fitting process. To determine which modes to reject, we assess the goodness of the fit by calculating the root mean square error between the fit and the measured R_{og}, shown Figure 5.1, with an example shown in Figure 5.2. For the simulated SPHERE-like system, we would reject all the modes below 60.

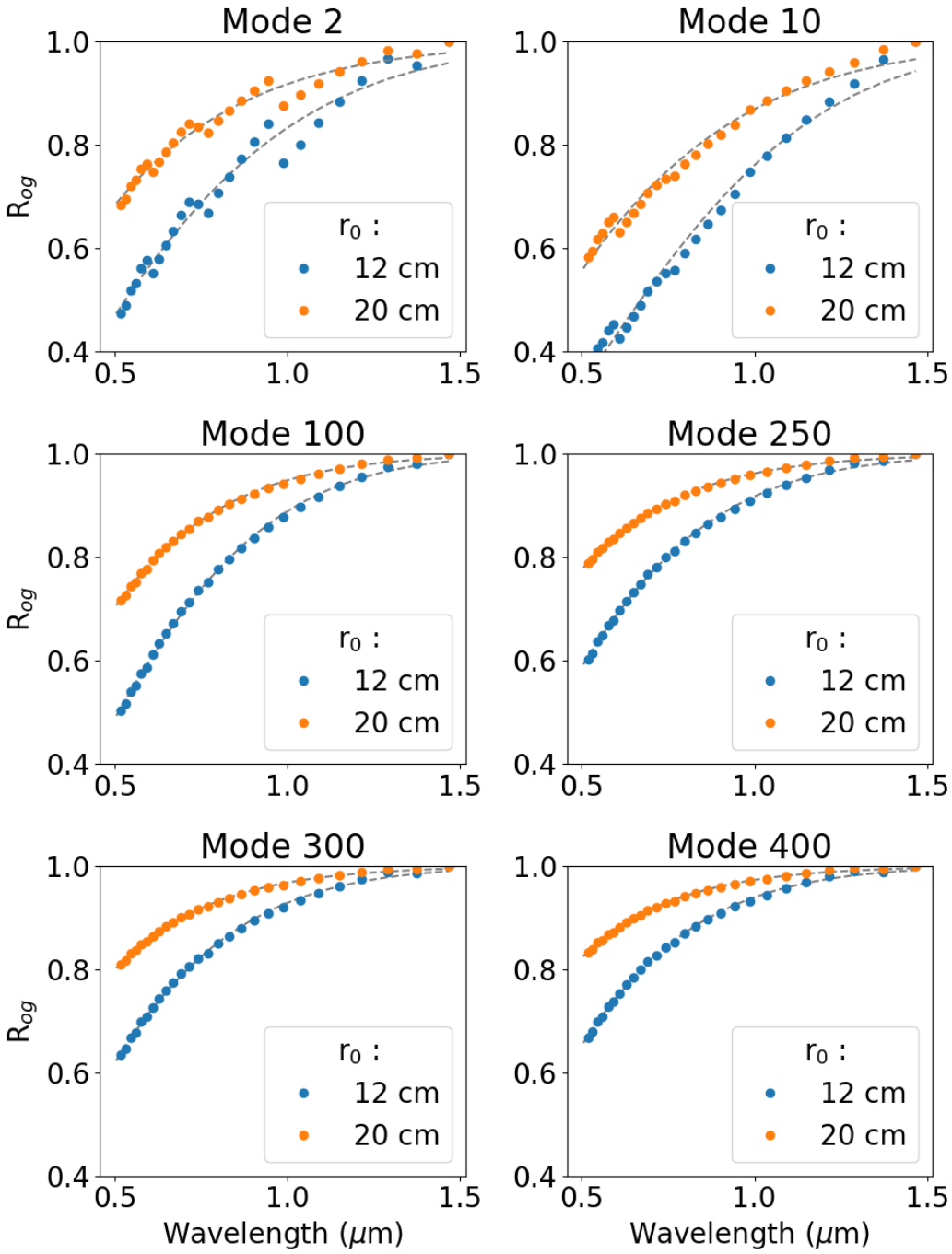

Figure 5.1: Variation of the optical gain ratios for 6 KL modes as a function of the wavelength for two values of r_0: 12 cm and 20 cm as derived from the convolutional model. The grey dashed lines show the empirical best fit to the model curves following the equation 5.4.

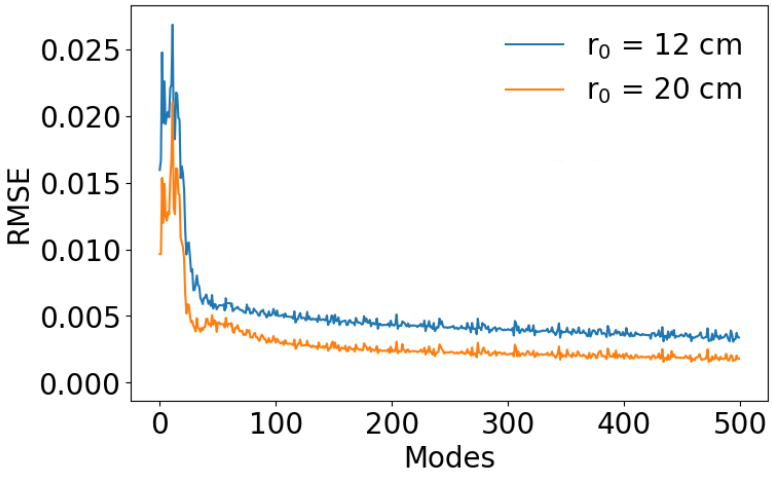

Figure 5.2: Root mean square error (RMSE) between the fit presented equation 5.4 and the optical gain ratios the variation of the optical gain ratios as a function of the wavelength for two values of r_0: 12 cm and 20 cm.

5.1.3 Model dependency to r_0

After fitting the wavelength distribution of R_{og}, we need to determine their dependence on r_0. Figure 5.3 shows a distribution A(r_0, μ) and B(r_0, μ) as a function of r_0 and we observe that they follow a linear law. As a result, we can fit A(r_0, μ) and B(r_0, μ) according to the following equations

$$\begin{aligned} A(r_0, \mu) &= \alpha_A(\mu) \times r_0 + \beta_A(\mu) \\ B(r_0, \mu) &= \alpha_B(\mu) \times r_0 + \beta_B(\mu) \end{aligned} \tag{5.5}$$

where coefficients $\alpha_{(A/B)}(\mu)$ and $\beta_{(A/B)}(\mu)$ are determined for the system studied for a given mode μ. The values of $\alpha_{(A/B)}(\mu)$ and $\beta_{(A/B)}(\mu)$ for all the modes are then stored to obtain a measure of r_0 from the fitting model.

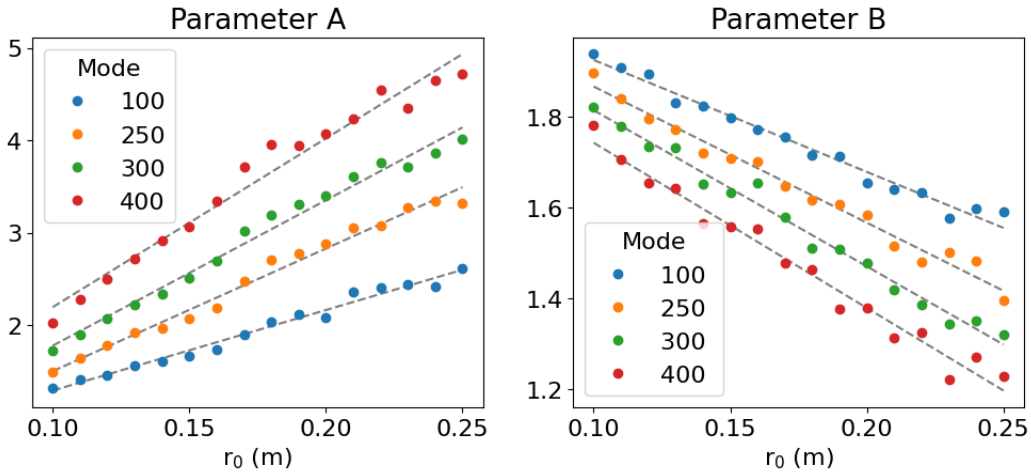

Figure 5.3: r_0 distribution of fitting parameters from Equation 5.4, model of the chromatic distribution of the optical gain ratios, for mode 100, 250, 300 and 400.

5.1.4 Estimation of r_0 from the fitting model

To estimate r_0 using the fitting model and the pre-calculated list of coefficients we follow the following steps:

1. For a given mode, we fit the model of $R_{og}(r_0, \mu, \lambda)$ to retrieve the values of $A(r_0, \mu)$ and $B(r_0, \mu)$

2. We invert the set of equations 5.5

$$r_0 = \frac{A(r_0, \mu) - \beta_A(\mu)}{\alpha_A(\mu)} \tag{5.6}$$

$$r_0 = \frac{B(r_0, \mu) - \beta_B(\mu)}{\alpha_B(\mu)} \tag{5.7}$$

3. A value of r_0 is then computed for each mode twice from the parameter $A(r_0, \mu)$ and $B(r_0, \mu)$

We then repeat the operation for all the modes of the DM basis.

5.2 Simulation implementations

In this section, we describe the method for generating the data set and the simulation setup. We then describe how the data are processed to compensate for instabilities and uncertainties in the measurement. Finally, we describe in detail the modal reconstruction algorithm used to generate the data set and run the AO loop to obtain an estimated value of r_0.

5.2.1 PWFS model

We need to determine the method of generating data sets in our simulation to build a fitting model. We have 2 independent models at our disposal (convolutional or diffractive) and we can use either the ratios of the reconstructed modal decomposition of the residual wavefront, R_{md}, or the optical gain ratios, R_{og}, for the different PWFS_λ channels. Figure 5.4 illustrates three examples of data sets generated using three different usable methods for dataset generation. Each method uses three PWFS_λ channels at 700 nm, 900 nm and 1200 nm and a fixed r_0 of 16 cm. The figure shows the ratios of the data generated for the channels at 700 nm and 900 nm by the data generated for the channel at 1200 nm. To ensure consistency, the residuals used for these methods are the same and are generated by Soapy. Below is a brief description of the datasets:

R_{og} **Conv.** : Optical gain ratio curves generated using the interaction matrices comparison method computed with the convolutional model described section 3.3.1.2

R_{md} **Diff.** : Modal decomposition of the residual wavefront ratios generated with the diffractive model implemented within the Soapy Monte Carlo simulation.

R_{md} **Conv.** : Modal decomposition of the wavefront ratios generated with the convolutional model for different PWFS_λ channels. To incorporate the non-

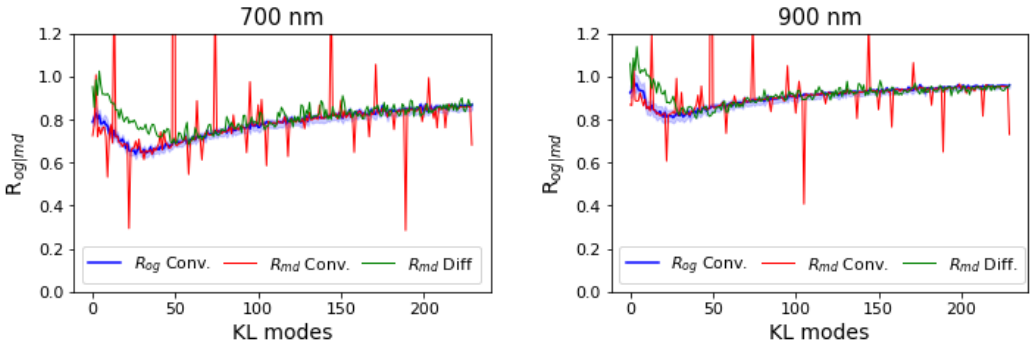

Figure 5.4: Examples of R_{og} spatial frequency distribution using three different generation methods. The wavefront residuals used to calculate the optical gain ratios and the modal decomposition were both generated using Soapy running a SPHERE-like system with 230 modes for a r_0 of 16 cm over 2000 frames. The wavelength used for the denominator is 1200 nm.

linearities due to the optical gains within the convolutional model reconstruction, an impulse response incorporating the residuals of the AO loop is computed for each frame.

It can be seen in the Figure 5.4 that the three datasets are in agreement for the higher-order modes, but not for the lower-order modes. This is expected as the convolutional model does not accurately reproduce the behaviour of the low-order modes (see Section 3.3.3). However, we have already addressed this issue by ignoring these modes within the fitting model. Finally, as they all agree and during operation we only have one measure of the modal decomposition, we decide to use the most computationally efficient method and use the R_{md} Conv. dataset for the rest of the chapter.

5.2.2 Data processing

There is uncertainty in measuring the wavefront, which affects the modal decomposition by introducing noise. To achieve the best possible update rate, it is necessary to average measured ratios over time. Therefore, we need to study two points: the method and the duration of the measurement averaging.

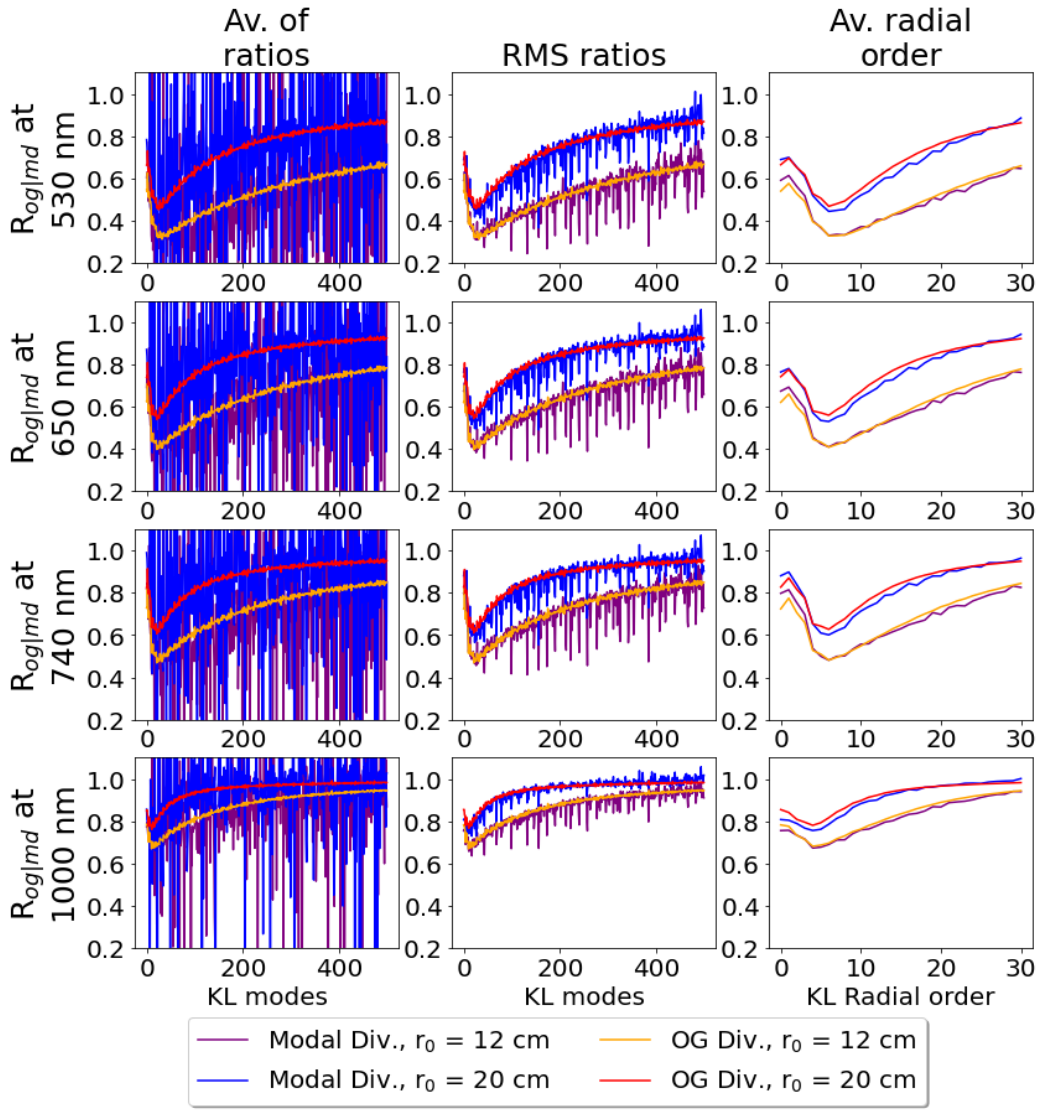

Figure 5.5: Comparison of averaging methods between R_{og} and R_{md} at different wavelengths. The wavelength used for the denominator is 1200 nm. The ratios had been generated using 50 residual atmospheric phase screens with a r_0 value of 12 cm and 20 cm.

5.2.2.1 Averaging method

Figure 5.5 displays the various averaging approaches examined in this section. Each column represents a different approach, and each row represents a measure at different wavelengths. The optical gain ratios and modal decomposition ratios are computed from 50 independent residual atmospheric phase screens.

Mean modal ratio The simplest approach involves calculating the modal ratios R_{md} frame by frame and subsequently averaging them over time. However, this method provides an unreliable measure of the ratio when the instantaneous modal amplitude has a value close to zero.

Modal RMS ratio For each mode of each modal decomposition measured by each PWFS$_\lambda$ channel, we get an RMS value over time and then we calculate the ratios of the modal RMS values. This has the advantage of burying the small denominator values in the ratios.

Average over radial orders For this method, we calculate the ratios of RMS of the modal decompositions but we now also average over several modes. To group the modes we refer to Noll's definition of radial orders for Zernike modes (Noll, 1976). Whilst we do not use Zernike modes, we do expect KL modes of the same radial order to exhibit the same wavefront variance. This additional averaging step can be used to further suppress system noise terms. The nth radial order is defined to be the modes within the following interval.

$$n_{th}\,\text{order} \Rightarrow \text{KL modes} \in \left[\frac{(n-1)n}{2},\ \frac{n(n+1)}{2}\right] \tag{5.8}$$

To quantify the stability of the measurement of modal decomposition we measure the difference with the optical gain ratio by calculating the RMS error between R_{og} and R_{md}. The values of those RMS error corresponding to the plots in Figure 5.5 are given Table 5.1. This table shows that averaging over the radial order of the ratios of the modal decomposition provides a close match to the ratios of optical gains. We will therefore adopt the radial order averaging method for the remainder of the fitting process.

	$r_0 = 12cm$			$r_0 = 20cm$		
	Av. of Ratios	RMS ratios	Av. Radial Order	Av. of Ratios	RMS ratios	Av. Radial Order
530 nm	39.213	0.061	0.019	7.650	0.060	0.026
650 nm	46.231	0.061	0.021	3.436	0.050	0.025
740 nm	48.254	0.062	0.025	2.024	0.048	0.025
1000 nm	34.633	0.030	0.013	1.952	0.021	0.019

Table 5.1: List of RMS error between optical gain ratios and modal decomposition ratios at different wavelengths for different r_0 values, obtained through different averaging methods

5.2.2.2 Temporal averaging

Figure 5.6 displays the RMS error between ratios of optical gain and ratios of modal decomposition as a function of the number of independent residual atmospheric phase screens used for the calculation. We choose arbitrarily a threshold of RMS error of 0.8 at $r_0 = 20$ cm and consider 20 independent residual atmospheric phase screens. The value of the threshold has yet to be determined by requirements and further in-depth simulations. During operations, the time used for averaging to obtain a measure of the ratios will depend on the variation of r_0 over time and the requirement for the estimation of r_0.

5.2.3 Reconstruction algorithm

The diagram presented in Figure 5.7 describes the reconstruction algorithm used to demonstrate the fitting model method for tracking the atmospheric conditions within the chromatic distribution of wavefront reconstruction. The algorithm consists of closing the AO loop using one PWFS_λ channel, and simultaneously reconstructing the wavefront with the rest of the other PWFS_λ channels. We also close AO loop on the longest wavelength possible to ensure the stability of the loop, as wavefront sensing at longer wavelengths is less prone to non-linearities (Bond

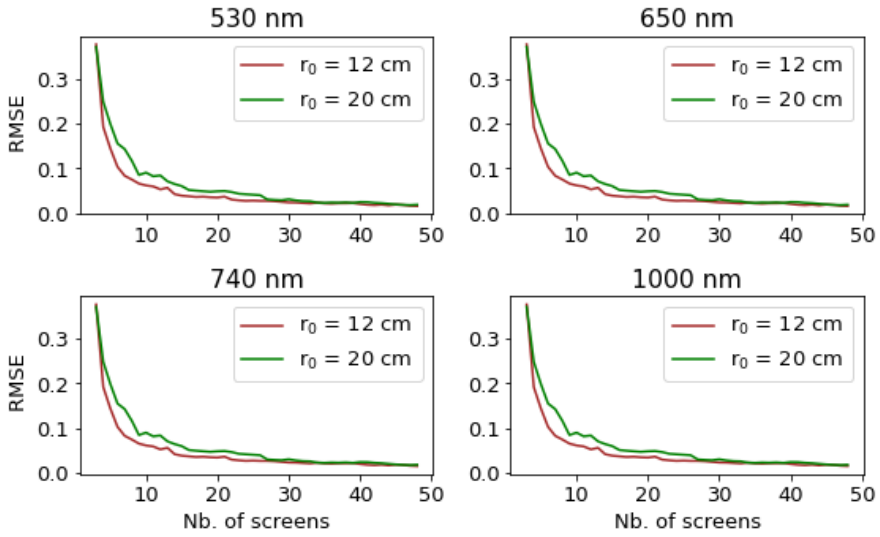

Figure 5.6: RMS error between ratios of optical gain and ratios of modal decomposition as a function of a number of independent residual atmospheric phase screens used for the ratios.

et al., 2020). As we have seen Chapter 4, in the absence of noise sources, the simple polychromatic reconstruction methods we have investigated in this thesis perform less well than using a single PWFS operating at longer wavelengths as the optical gains are closer to 1.

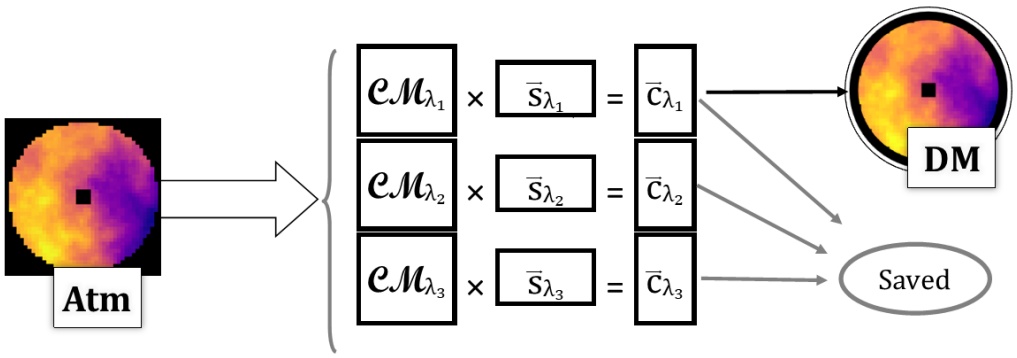

Figure 5.7: Diagram of the polychromatic wavefront reconstruction algorithm integrated within the Soapy Monte Carlo simulation. Each PWFS$_\lambda$ is calibrated independently and has its own $\mathcal{IM}$ and $\mathcal{CM}$. The AO loop is closed using a single PWFS$_\lambda$, while all receive the same input phase screen. All the reconstruction PWFS$_\lambda$ are then saved for post-processing.

5.3 Dataset

This section presents the dataset used for estimating r_0 in the next section. We provide a list of parameters and a plot of the curves used for model fitting. Finally, we discuss the values of the fitting parameters.

5.3.1 Parameters

Table 5.2 lists the parameters used to generate the model-fitting dataset. It should be noted that the number of frames does not include the first 100 frames of the loop, which are ignored. The AO loop is intentionally slowed down to 200 Hz to ensure a strong influence of the optical gains.

Parameter	value
Telescope Diameter	8 m
Frame rate	200 Hz
PWFS pupil sampling	40 x 40 pixels
DM Actuators	500
Closed-loop gain	0.6
Latency	1 frame
Read noise	0
List of channels	521 nm, 575 nm, 641 nm, 723 nm, 928 nm, 965 nm, 1152 nm and 1490 nm
Control wavelength	1490 nm
r_0 range	10 cm to 25 cm in steps of 1 cm
Fitted radial orders	10 to 30
Wind speed	10 m/s
Number of frames	400

Table 5.2: List of the PWFS parameters used to generate the model fitting dataset.

5.3.2 Example of ratio curves

Figure 5.8 shows an example of the ratio curves considered for the example created for this chapter. These curves have been plotted for different r_0 and are used for fitting. The plot demonstrates the influence of atmospheric condition variation on the ratios, similar to what was shown in the previous chapter, section 4.3.

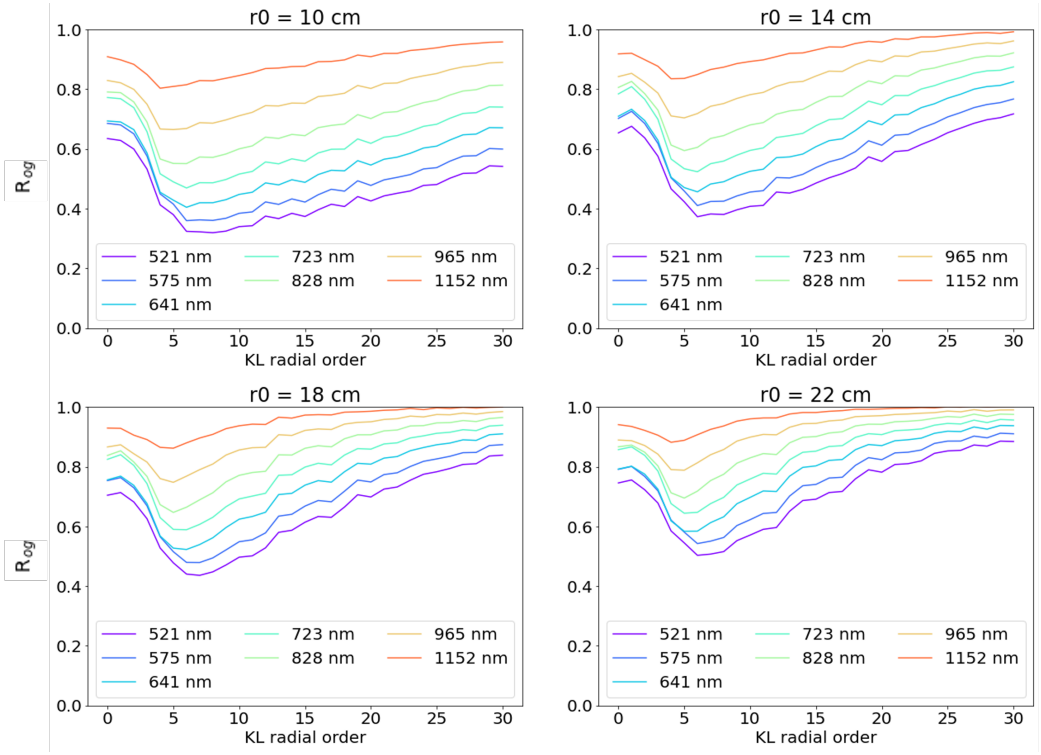

Figure 5.8: KL radial order reconstruction ratios compared to 1490 nm reconstruction for different PWFS$_\lambda$ using the parameters shown in Table 4.1 for different r_0 at 500 nm.

5.3.3 Model fitting coefficients

Figure 5.9 shows the distribution of the $\alpha_{(A/B)}(\mu)$ and $\beta_{(A/B)(\mu)}$ fitting parameters over the radial orders calculated for the generated data set. It can be seen that the distribution of the α_A parameter is less linear than that of the other parameters. This suggests a weaker influence of spatial frequency in the influence of this parameter.

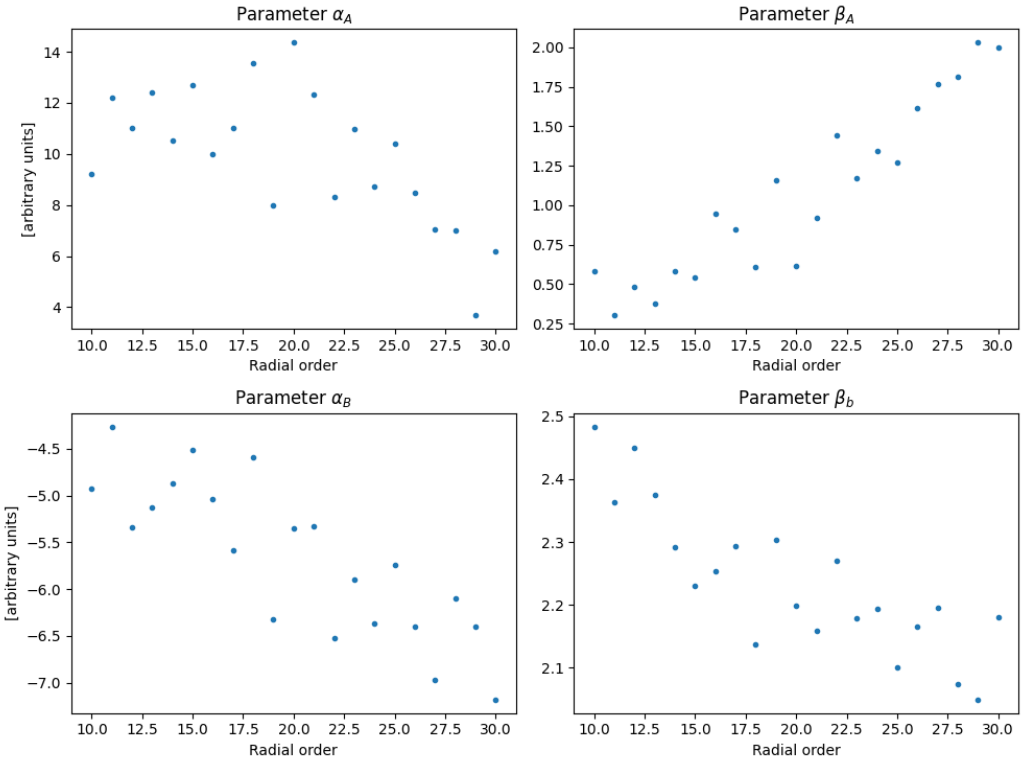

Figure 5.9: Distribution of the parameters of the $\alpha_{(A/B)}(\mu)$ and $\beta_{(A/B)(\mu)}$ fitting model over radial orders for the parameters in Table 4.1.

5.4 r_0 estimation

In this section, we present the estimation of r_0 using the model fitting method that determined the $\alpha_{(A/B)}(\mu)$ and $\beta_{(A/B)}(\mu)$ parameters presented in the previous section. First, we present the estimation for different individual values of r_0. Then, we demonstrate near-real-time estimation of r_0 in the presence of an evolving turbulence strength.

5.4.1 Different atmospheric condition r_0 estimation

Figure 5.10 shows the estimation of the value of r_0 under various atmospheric conditions using the model fitting approach. The figure was generated by running multiple independent iterations of the AO loop with a constant value of r_0 applied to the input atmospheric phase screen, using the parameters described in Table 5.2

The results presented are an average of the six independent iterations. The analysis is restricted to radial orders above 10, and only parameter A or only parameter B is considered.

The plot presented shows that the model estimates r_0 with an error of no more than 20 percent. However, fitting using only parameter B results in an error of less than 10 percent. A clear trend is also observed where increasing the value of r_0 leads to an increase in measurement error and uncertainty. This can be explained due to the increased influence of stronger perturbations on the optical gains, making their effects more visible on R_{og}, thus facilitating its fitting. Although heightened sensitivity is necessary to acquire accurate measures under stronger perturbations, it is important to note that the measurement tends to systematically underestimate r_0. This drawback is significant because overestimating perturbation strength may lead to excessive compensation for optical gains, potentially compromising the stability of the adaptive optics loop.

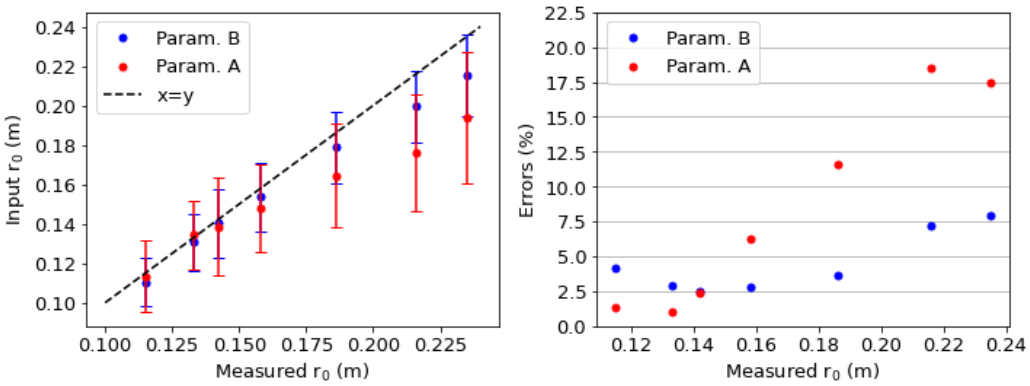

Figure 5.10: Left : r_0 estimation computed using the parameter A or B for different input r_0 values. The error bars are computed using the standard deviation of the r_0 distribution over radial orders. Right: Percentage error in the estimation of r_0.

5.4.2 Tracking r_0 over time

The AO loop is run over 1600 frames with a 200 Hz frame rate, which means we measure the wavefront for 8 seconds. Two variations of r_0 were included during this time, one increase and one decrease. To generate the variation of r_0, an initial

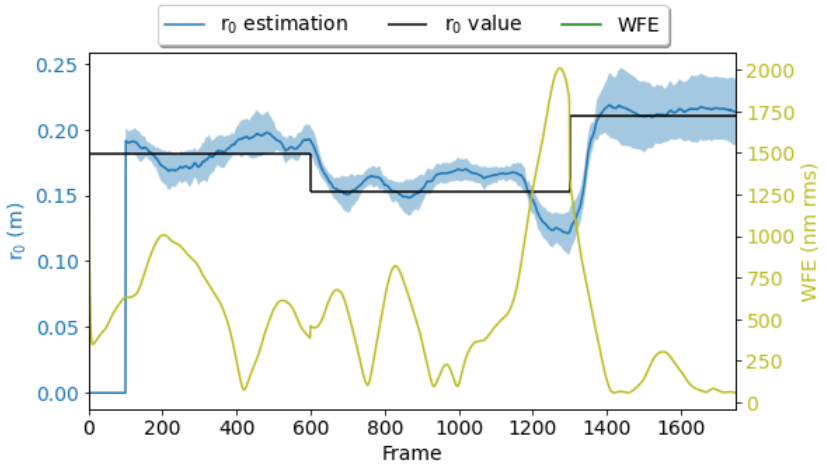

Figure 5.11: Temporal evolution of estimation of r_0 and WFE. r_0 has been estimated using only the parameter B of the model fitting. The area around the curve is a standard deviation of all the individual r_0 estimations.

series of atmospheric phase screens was generated with the AOtools package. As AOtools can not integrate variation of r_0, the phase screens have been adjusted using Equation 4.3 afterwards. Figure 5.11 shows the tracking of r_0 over time, averaging the estimation of r_0 over 50 frames. Only the parameter B was fitted to determine the estimation of r_0.

It is evident that the method accurately tracks changes in r_0 within 50 frames (or 0.25 seconds), whether there is an increase or decrease in turbulence strength. The highest measure for the values of r_0 is stable over time on average, but the standard deviation of r_0 estimation is larger. This is consistent with the fact that the correction by the DM is more stable when the perturbations are weaker, but the fitting distribution of r_0 is larger when the impact of the optical gain is weaker. The inverse effect is observed at lower r_0 values. We also note that the variation in estimation is consistent with the instantaneous WFE, showing that the accuracy of the model depends on the stability of the correction.

5.5 Discussion

The use of an MKID array provides an additional dimension to PWFS measurements. To enhance the performance of the MKID-based PWFS, we need to compensate for the optical gains and therefore require a method to estimate them. The wavelength dependence of the MKID-based PWFS allows us to make this estimate without requiring additional hardware components. In this chapter, we have presented a model to track the variation of r_0 by comparing the wavefront reconstruction at different wavelengths. This model that determines r_o can then subsequently be used as the basis for the recovery of the optical gains.

To calibrate the model we simulate the response of the MKID-based PWFS at different r_0. During operation, we use this calibration to estimate r_0 for each radial order over two fitted model parameters. To implement the method, we used the computationally efficient convolutional model (see section 3.2.2) to obtain the ratio between the modal decomposition of the wavefront as measured by the PWFS at different wavelengths. We showed that these ratios could also be measured using a Monte Carlo diffractive model.

We examined various simple optimisations for model fitting. To mitigate default on individual modes and small values that could spike the ratio values, we averaged R_{md} over spatial frequency. We also averaged R_{md} over time. We selected the optimal estimation parameters which resulted in an r_0 estimation error of 10 percent. It was observed that the estimation improves with stronger perturbations.

Additionally, the method enables tracking of r_0 over time, with the value of r_0 increasing or decreasing. To our knowledge, current technologies are not able to track r_0 within the same magnitude of timeframe. This is why, it is difficult to predict at what rate the atmospheric conditions are changing and how well this could potentially perform. However, the update rate of the estimation of r_0 is directly linked to the integration time of the estimation, and this integration time should be

chosen to balance between error on the measurement and r_0 variation sensitivity. As the real-time tracking of r_0 within the modal wavefront reconstruction would be happening for the first time, this has the potential to open a new area of study in atmospheric tomography.

While these results are promising, there are still several points that need to be studied to better understand and improve the method

- All the results presented in this chapter are based on the estimation or r_0 (and subsequent optical gain compensation) for a SPHERE-like XAO system deployed on an 8m telescope. We can examine time averaging and adjust accordingly for different systems.
- The impact of the system parameter on the fitting parameters can be analysed to extend the model to wider systems and gain a deeper understanding of the fitting process. This will allow us the development of a more precise mathematical formalism.
- The impact of different noise sources, such as photon noise or NCPA, has yet to be studied. To investigate the influence of noise, the method needs to be implemented using the diffractive model.

The finality of this method is to compensate for the optical gains to enhance the performance of the adaptive optics system. This can be achieved by creating a lookup table of optical gains for different values of r_0 in our system and using model fitting to obtain a value of r_0. The table can then be used for optical gain compensation. It should be noted that this step has not yet been implemented. After implementation, the r_0 tracking method needs to be updated to account for compensation. This is because compensation can impact the wavefront measurement, which the current model does not consider.

CHAPTER 6

CONCLUSION

6.1 Synopsis

This thesis presents a project that explores the potential of using an energy resolution detector for a PWFS. The use of detectors such as MKID arrays has made this possible. The focus of this work is on modelling a PWFS and examining the energy sensitivity properties of an MKID that could be used to improve PWFS performance. The initial study was simplified by excluding temporal properties and assuming only monochromatic signals without uncertainty in the measurement of the wavelength.

Chapter 3 presented a model of the system that uses existing PWFS monochromatic models simultaneously. Two models of the PWFS have been prensented : the diffractive and the convolutional model. The diffractive model is a physical description of the PWFS, and is used when needed accuracy is required. The convolutional model is a mathematical approximation of the PWFS initially developed for the rapid computation of optical gains. To simulate the wavelength sensitivity of the MKID each PWFS instance operates as a λ-channel at a specific wavelength, measuring the same input wavefront in the end-to-end AO simulation. The parameters of each channel are identical, except for the wavelength. The modulation radius is given in arcseconds in the focal plane. The traditional unit of λ/D must be computed outside of the model for each channel.

In Chapter 4 we studied the behaviour of individual chromatic channels and compared them with a polychromatic reconstruction. To generate the polychromatic reconstruction, we developed a new algorithm that extends the signal of the wavefront sensor and concatenates the slope vector into a longer slope vector. Then, an interaction matrix is generated as described in section 2.2.2. We explored three aspects of the chromatic behaviour of the PWFS:

- Linearity range/sensitivity: As demonstrated in section 4.2, each channel is subject to the well-known trade-off presented in chapter 2, as the modulation effect is related to the PSF size. Shorter wavelengths have a greater dynamic range, while longer wavelengths are more sensitive. The combination of both wavelengths appears to average the sensitivity and linearity of the individual channels without overcoming the trade-off, as shown in Figures 4.7 and 4.8. However, it may be beneficial to investigate a weighing system adapted to the level of perturbation.

- Optical gains: The first comprehensive study on the wavelength dependence of optical gain for PWFS is presented in section 4.3. It is shown that optical gains are a function of spatial frequency, wavelength, atmospheric conditions and modulation amplitude for a given system. Furthermore, the chromatic variation for a given spatial frequency varies with the atmospheric condition, indicating that the effect of the value of r_0 on the optical gain differs for each channel.

- Photon level: The accuracy of measuring wavefronts depends on the strength of the signal, specifically the number of photons detected per loop iteration. As shown in section 4.4, AO performance decreases with fainter targets. Dividing the overall bandpass of WFS detection into sub-wavebands counters chromatic dispersion and enables the observation of fainter targets. It has been shown that WFS operating at smaller wavelengths perform better with fainter targets. However, smaller wavelengths are more impacted by optical

gain. As the aim is to observe fainter targets, this section highlights the necessity to compensate for optical gains to optimize the AO system with an energy-sensitive detector.

Polychromatic reconstruction has not been studied exhaustively, therefore, it is interesting to see that the wavefront reconstruction at different wavelengths has complementary properties. While shorter wavelengths are more sensitive, they are also more prone to non-linearities such as optical gain or measurement saturation. Conversely, longer wavelengths are more linear but are less sensitive. Having access to both measurements simultaneously therefore has the potential to mitigate the main drawbacks of a PWFS.

These behaviours have been studied considering perfect knowledge of the wavelength. If an MKID array were to be used, effects such as uncertainty in measuring photon energy and saturation effects would have to be taken into account. The energy resolution of an MKID is not infinite, which affects the accuracy of photon energy measurement. This has two impacts on wavefront measurement:

- The width of the waveband of each channel
- Error of attribution of the photon to a given channel or colour confusion

Examining the study on chromatic behaviour, it is important to note that the uncertainty in energy measurement was not accounted for in the models used within this thesis which could affect the chromatic distribution of the optical gain. It should be noted that the energy resolution of an MKID is better at lower wavelengths when the energy of a photon is higher, which is also where the variation in optical gain as a function of atmospheric conditions is strongest.

If the photon flux is too strong, PWFS measurements can become saturated, which may degrade performance when using a bright guide star. To avoid this, optical measures can be taken to reduce the flux per pixel. Figures 4.17 and 4.18 show

that as long as the MKID array can detect enough photons per loop iteration, performance stabilizes below magnitude 12 for the simulated system. To further improve performance, photons can be filtered out using a neutral density filter without degrading performance. To achieve the maximum performance of our system, it is necessary to determine the minimum photon flux required. This value is crucial to know when manufacturing the array, either by decrease the recombination time, at the expense of the energy resolution or by improving the pulse analysis algorithm.

The widening of the bandpass also affects chromatic dispersion. To widen the detected spectra beyond what is enabled by the double pyramid design, the waveband of each channel must be narrow enough to fall within the 0.2-pixel dispersion. Additionally, the chromatic dispersion can cause colour confusion, which may result in photons being associated with the wrong pixel in the pupil image. Depending on the error it produces on the wavefront measurement, it may be necessary to create a custom prism design to mitigate this phenomenon.

Chapter 5 presents a method for tracking optical gains using the additional dimension provided by the chromatic measures of the wavefront. This method solely uses the wavelength dependence modal reconstruction of the wavefront without any additional external hardware or calibration during operation, as opposed to current methods. It involves constructing a model of the chromatic variation of the optical gain based on the atmospheric conditions, represented by the value of r_0. The convolutional model has been used to implement the optical gain tracking model. For the system studied, the method for tracking r_0 is accurate within 15 percent and continues to track r_0 even when it varies. Its accuracy improves as r_0 decreases. This is because a smaller r_0 indicates a stronger perturbation and therefore a stronger signal for the model to fit. Therefore, it is easier to track optical gains at shorter wavelengths. Once the value of r_0 is measured, it is then possible to retrieve an estimation of the optical gains. This is to our knowledge the first real-time r_0 tracking method directly from the wavefront measurements.

While this method provides an initial concept, further study is necessary. To improve the simulation's physical accuracy, the diffractive model should be used, and the MKID properties should be integrated. The diffractive model should integrate error terms non taken into account by the convolutional model. However, we have seen that the noise can be reduced through averaging. The uncertainty in energy measurement also affects the chromatic distribution of the wavefront measurement.

6.2 Future work

Throughout this thesis, we have explored the potential of using an energy-sensitive detector as a PWFS detector. This is now possible thanks to the emergence of MKID arrays. However, this technology is still in development and requires further improvements. By conducting studies such as this thesis, we can guide the manufacturer towards the MKID array required for our application: XAO system for exoplanet imaging.

Our examination of the MKID array focused on its energy sensitivity, particularly in relation to its use in optical gain tracking. To this end, an essential requirement is the determination of the minimum energy resolution required for the method to perform successfully. Although this value is currently undetermined, we outline the methodology for its future determination. We have shown that the resolution of current arrays is sufficient to enable polychromatic wavefront sensing. A higher spectral resolution would allow more data points for the optical gain tracking method, but it would also mean less photon per waveband, decreasing the SNR of each invidual PWFS_λ channel. If the number of waveband was to be conserved, however, it a higher spectral resolution would minimize the impact of colour confusion if required. On the other hand a decrease in spectral resolution would certainly means less wavebands considered. One of the next step is then to determine what has the most impact on the method's performance, the SNR per waveband or the number of waveband.

The optical gain tracking model was shown to be successful for a SPHERE-like system when the spectrum is divided into eight wavebands. Large MKID arrays, such as MEC, already achieve the necessary energy resolution for this number of wavebands. However, for a PCS system at the ELT scale, the required number of PWFS$_\lambda$ channels is still uncertain. Furthermore, Section 4.3.3 discusses the need for further exploration of the impact of energy measurement uncertainty on the noise in wavefront measurements. Our plan is to propagate this uncertainty through the model to determine its contribution to the overall uncertainty in measuring r_0. By characterising the system and specifying the desired precision for measuring r_0, we can determine the necessary energy resolution for the MKID array in our targeted AO system.

In addition to the optical gain method tracking, there are other areas to explore, such as addressing problems encountered by XAO systems, including the island effect (Schwartz et al., 2017). The text also highlights how energy sensitivity can help mitigate chromatic dispersion caused by the pyramidal prism. Instead of countering it, we could try to use it to our advantage by designing a specific prism to artificially increase the wavefront sensor resolution. This can be achieved by using a slight displacement between the pupil images at different wavelengths (Oberti et al., 2022). Another option is to increase the sensitivity, as illustrated in figure 6.1, to obtain the flattened pyramid (Fauvarque et al., 2017).

Finally, the temporal information has yet to be explored. MKIDs have the capacity of measuring photon arrival time. To integrate it in the model, the current model would need to add intermediate steps for each AO loop iteration, with different modulation of the PSF stages. This would multiply the computation needs by the number of intermediate step. However this is another information that could be useful when used by the AO reconstruction. For example, it can ensure a SNR per PWFS$_\lambda$ channel or per AO loop iteration and adapt the AO loop frequency to the magnitude of the guide star.

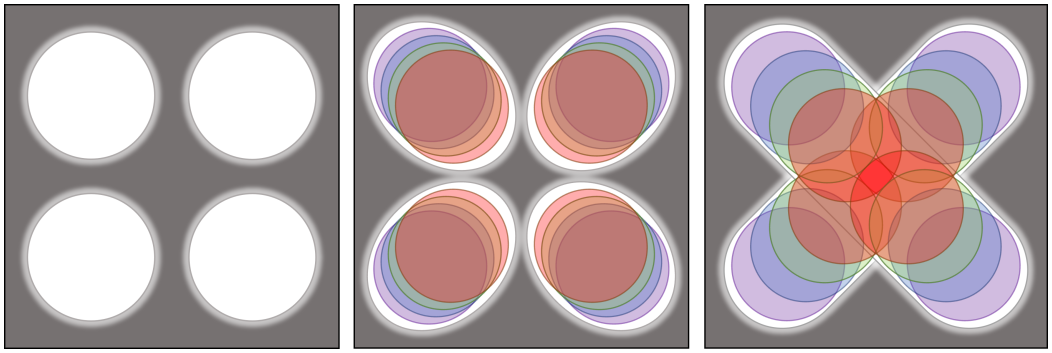

Figure 6.1: Illustration of different intensities read by a PWFS detector from left to right: non-energy sensitive detector detecting a narrow waveband, MKID detecting multiple wavebands diffracted by the pyramidal prism, MKID detecting multiple wavebands with an exaggerated dispersion and a 'flattened pyramid' case for the central pupil images.

BIBLIOGRAPHY

G. Agapito and E. Pinna. Semianalytical error budget for adaptive optics systems with pyramid wavefront sensors. *Journal of Astronomical Telescopes, Instruments, and Systems*, 5(04):1, Oct. 2019. ISSN 2329-4124. doi: 10.1117/1.JATIS.5.4.049001. URL https://www.spiedigitallibrary.org/journals/Journal-of-Astronomical-Telescopes-Instruments-and-Systems/volume-5/issue-04/049001/Semianalytical-error-budget-for-adaptive-optics-systems-with-pyramid-wavefront/10.1117/1.JATIS.5.4.049001.full.

K. Ahn, O. Guyon, J. Lozi, S. Vievard, V. Deo, N. Skaf, R. Belikov, S. P. Bos, M. Bottom, T. Currie, R. Frazin, K. V. Gorkom, T. D. Groff, S. Y. Haffert, N. Jovanovic, H. Kawahara, T. Kotani, J. R. Males, F. Martinache, B. Mazin, K. Miller, B. Norris, A. Rodack, and A. Wong. SCExAO: a testbed for developing high-contrast imaging technologies for ELTs. In *Techniques and Instrumentation for Detection of Exoplanets X*, volume 11823, pages 9–21. SPIE, Sept. 2021. doi: 10.1117/12.2594963. URL https://www.spiedigitallibrary.org/conference-proceedings-of-spie/11823/1182303/SCExAO---a-testbed-for-developing-high-contrast-imaging/10.1117/12.2594963.full.

H. W. Babcock. The possibility of compensating astronomical seeing. *Publications of the Astronomical Society of the Pacific*, 65(386):229–236, 1953. ISSN 0004-6280. URL https://www.jstor.org/stable/40672682.

A. Bertrou-Cantou, E. Gendron, G. Rousset, V. Deo, F. Ferreira, A. Sevin, and

F. Vidal. Confusion in differential piston measurement with the pyramid wavefront sensor. *Astronomy & Astrophysics*, 658:A49, Feb. 2022. ISSN 0004-6361, 1432-0746. doi: 10.1051/0004-6361/202141632. URL https://www.aanda.org/10.1051/0004-6361/202141632.

J.-L. Beuzit, A. Vigan, D. Mouillet, K. Dohlen, R. Gratton, A. Boccaletti, J.-F. Sauvage, H. M. Schmid, M. Langlois, C. Petit, A. Baruffolo, M. Feldt, J. Milli, Z. Wahhaj, L. Abe, U. Anselmi, J. Antichi, R. Barette, J. Baudrand, P. Baudoz, A. Bazzon, P. Bernardi, P. Blanchard, R. Brast, P. Bruno, T. Buey, M. Carbillet, M. Carle, E. Cascone, F. Chapron, J. Charton, G. Chauvin, R. Claudi, A. Costille, V. D. Caprio, J. d. Boer, A. Delboulbé, S. Desidera, C. Dominik, M. Downing, O. Dupuis, C. Fabron, D. Fantinel, G. Farisato, P. Feautrier, E. Fedrigo, T. Fusco, P. Gigan, C. Ginski, J. Girard, E. Giro, D. Gisler, L. Gluck, C. Gry, T. Henning, N. Hubin, E. Hugot, S. Incorvaia, M. Jaquet, M. Kasper, E. Lagadec, A.-M. Lagrange, H. L. Coroller, D. L. Mignant, B. L. Ruyet, G. Lessio, J.-L. Lizon, M. Llored, L. Lundin, F. Madec, Y. Magnard, M. Marteaud, P. Martinez, D. Maurel, F. Ménard, D. Mesa, O. Möller-Nilsson, T. Moulin, C. Moutou, A. Origné, J. Parisot, A. Pavlov, D. Perret, J. Pragt, P. Puget, P. Rabou, J. Ramos, J.-M. Reess, F. Rigal, S. Rochat, R. Roelfsema, G. Rousset, A. Roux, M. Saisse, B. Salasnich, E. Santambrogio, S. Scuderi, D. Segransan, A. Sevin, R. Siebenmorgen, C. Soenke, E. Stadler, M. Suarez, D. Tiphène, M. Turatto, S. Udry, F. Vakili, L. B. F. M. Waters, L. Weber, F. Wildi, G. Zins, and A. Zurlo. SPHERE: the exoplanet imager for the Very Large Telescope. *Astronomy & Astrophysics*, 631:A155, Nov. 2019. ISSN 0004-6361, 1432-0746. doi: 10.1051/0004-6361/201935251. URL https://www.aanda.org/articles/aa/abs/2019/11/aa35251-19/aa35251-19.html. Publisher: EDP Sciences.

A. Boccaletti, G. Chauvin, D. Mouillet, O. Absil, F. Allard, S. Antoniucci, J.-C. Augereau, P. Barge, A. Baruffolo, J.-L. Baudino, P. Baudoz, M. Beaulieu, M. Benisty, J.-L. Beuzit, A. Bianco, B. Biller, B. Bonavita, M. Bonnefoy, S. Bos, J.-C. Bouret, W. Brandner, N. Buchschache, B. Carry, F. Cantalloube, E. Cas-

cone, A. Carlotti, B. Charnay, A. Chiavassa, E. Choquet, Y. Clenet, A. Crida, J. De Boer, V. De Caprio, S. Desidera, J.-M. Desert, J.-B. Delisle, P. Delorme, K. Dohlen, D. Doelman, C. Dominik, V. D. Orazi, C. Dougados, S. Doute, D. Fedele, M. Feldt, F. Ferreira, C. Fontanive, T. Fusco, R. Galicher, A. Garufi, E. Gendron, A. Ghedina, C. Ginski, J.-F. Gonzalez, D. Gratadour, R. Gratton, T. Guillot, S. Haffert, J. Hagelberg, T. Henning, E. Huby, M. Janson, I. Kamp, C. Keller, M. Kenworthy, P. Kervella, Q. Kral, J. Kuhn, E. Lagadec, G. Laibe, M. Langlois, A.-M. Lagrange, R. Launhardt, L. Leboulleux, H. L. Coroller, G. L. Causi, M. Loupias, A. L. Maire, G. Marleau, F. Martinache, P. Martinez, D. Mary, M. Mattioli, J. Mazoyer, H. Meheut, F. Menard, D. Mesa, N. Meunier, Y. Miguel, J. Milli, M. Min, P. Molliere, C. Mordasini, G. Moretto, L. Mugnier, G. M. Arena, N. Nardetto, M. N. Diaye, N. Nesvadba, F. Pedichini, P. Pinilla, E. Por, A. Potier, S. Quanz, J. Rameau, R. Roelfsema, D. Rouan, E. Rigliaco, B. Salasnich, M. Samland, J.-F. Sauvage, H.-M. Schmid, D. Segransan, I. Snellen, F. Snik, F. Soulez, E. Stadler, D. Stam, M. Tallon, P. Thebault, E. Thiebaut, C. Tschudi, S. Udry, R. van Holstein, P. Vernazza, F. Vidal, A. Vigan, R. Waters, F. Wildi, M. Willson, A. Zanutta, A. Zavagno, and A. Zurlo. SPHERE+: Imaging young Jupiters down to the snowline. *arXiv:2003.05714 [astro-ph]*, Mar. 2020. URL http://arxiv.org/abs/2003.05714. arXiv: 2003.05714.

C. Z. Bond, S. Cetre, S. Lilley, P. Wizinowich, D. Mawet, M. Chun, E. Wetherell, S. Jacobson, C. Lockhart, E. Warmbier, S. Ragland, C. Álvarez, O. Guyon, S. Goebel, J.-R. Delorme, N. Jovanovic, D. N. Hall, J. K. Wallace, M. Taheri, and V. Chambouleyron. Adaptive optics with an infrared pyramid wavefront sensor at Keck. *Journal of Astronomical Telescopes, Instruments, and Systems*, 6(03), Sept. 2020. ISSN 2329-4124. doi: 10.1117/1.JATIS.6.3.039003. URL https://www.spiedigitallibrary.org/journals/Journal-of-Astronomical-Telescopes-Instruments-and-Systems/volume-6/issue-03/039003/Adaptive-optics-with-an-infrared-pyramid-wavefront-sensor-at-Keck/10.1117/1.JATIS.6.3.039003.full.

H. Bonnet, F. Biancat-Marchet, M. Dimmler, M. Esselborn, N. Kornweibel, M. L. Louarn, P.-Y. Madec, E. Marchetti, M. Müller, S. Oberti, J. Paufique, L. Pettazzi, B. Sedghi, J. Spyromilio, S. Stroebele, C. Vérinaud, and E. Vernet. Adaptive optics at the ESO ELT. In *Adaptive Optics Systems VI*, volume 10703, pages 327–335. SPIE, July 2018. doi: 10.1117/12.2312407. URL https://www.spiedigitallibrary.org/conference-proceedings-of-spie/10703/1070310/Adaptive-optics-at-the-ESO-ELT/10.1117/12.2312407.full.

S. L. Campbell and C. D. Meyer. *Generalized inverses of linear transformations*. Dover Publications, New York, 1991. ISBN 978-0-486-66693-8.

V. Chambouleyron. *Optimisation de l'analyse de surface d'onde par filtrage de Fourier pour les systèmes d'optique adaptative à hautes performances*. These de doctorat, Aix-Marseille, Dec. 2021. URL https://www.theses.fr/2021AIXM0629.

V. Chambouleyron, O. Fauvarque, P. Janin-Potiron, C. Correia, J.-F. Sauvage, N. Schwartz, B. Neichel, and T. Fusco. Pyramid wavefront sensor optical gains compensation using a convolutional model. *Astronomy & Astrophysics*, 644:A6, Dec. 2020. ISSN 0004-6361, 1432-0746. doi: 10.1051/0004-6361/202037836. URL https://www.aanda.org/articles/aa/abs/2020/12/aa37836-20/aa37836-20.html.

V. Chambouleyron, O. Fauvarque, J.-F. Sauvage, B. Neichel, and T. Fusco. Focal-plane-assisted pyramid wavefront sensor: Enabling frame-by-frame optical gain tracking. *Astronomy & Astrophysics*, 649:A70, May 2021. ISSN 0004-6361, 1432-0746. doi: 10.1051/0004-6361/202140354. URL https://www.aanda.org/10.1051/0004-6361/202140354.

R. Conan and C. Correia. Object-oriented Matlab adaptive optics toolbox. In *Adaptive Optics Systems IV*, volume 9148, page 91486C. International Society for Optics and Photonics, Aug. 2014. doi: 10.1117/12.2054470. URL https://www.spiedigitallibrary.org/conference-proceedings-of-

spie/9148/91486C/Object-oriented-Matlab-adaptive-optics-toolbox/10.1117/12.2054470.short.

J. W. Cooley and J. W. Tukey. An Algorithm for the Machine Calculation of Complex Fourier Series. *Mathematics of Computation*, 1965.

P. K. Day, H. G. LeDuc, B. A. Mazin, A. Vayonakis, and J. Zmuidzinas. A broadband superconducting detector suitable for use in large arrays. *Nature*, 425 (6960):817–821, Oct. 2003. ISSN 1476-4687. doi: 10.1038/nature02037. URL https://www.nature.com/articles/nature02037.

P. J. de Visser, S. A. de Rooij, V. Murugesan, D. J. Thoen, and J. J. Baselmans. Phonon-Trapping-Enhanced Energy Resolution in Superconducting Single-Photon Detectors. *Physical Review Applied*, 16(3):034051, Sept. 2021. ISSN 2331-7019. doi: 10.1103/PhysRevApplied.16.034051. URL https://link.aps.org/doi/10.1103/PhysRevApplied.16.034051.

V. Deo. *Analyse et mise en œuvre de l'analyseur pyramide pour l'optique adaptative à très hauts ordres des ELT*. PhD thesis, Université Paris Cité, Oct. 2019. URL https://tel.archives-ouvertes.fr/tel-03128914.

V. Deo, E. Gendron, G. Rousset, F. Vidal, T. Buey, and M. Cohen. Assessing and mitigating alignment defects of the pyramid wavefront sensor: a translation insensitive control method. *Astronomy and Astrophysics*, page 13, 2018.

R. H. Dodkins, K. Davis, B. Lewis, S. Mahashabde, B. A. Mazin, I. A. Lipartito, N. Fruitwala, K. O'Brien, and N. Thatte. First Principle Simulator of a Stochastically Varying Image Plane for Photon-Counting High Contrast Applications. *arXiv:2007.15274 [astro-ph]*, July 2020. URL http://arxiv.org/abs/2007.15274. arXiv: 2007.15274.

S. Esposito and A. Riccardi. Pyramid Wavefront Sensor behavior in partial correction Adaptive Optic systems. *Astronomy & Astrophysics*, 369(2):L9–L12, Apr.

2001. ISSN 0004-6361, 1432-0746. doi: 10.1051/0004-6361:20010219. URL https://www.aanda.org/articles/aa/abs/2001/14/aacl202/aacl202.html.

S. Esposito, A. Riccardi, L. Fini, A. T. Puglisi, E. Pinna, M. Xompero, R. Briguglio, F. Quirós-Pacheco, P. Stefanini, J. C. Guerra, L. Busoni, A. Tozzi, F. Pieralli, G. Agapito, G. Brusa-Zappellini, R. Demers, J. Brynnel, C. Arcidiacono, and P. Salinari. First light AO (FLAO) system for LBT: final integration, acceptance test in Europe, and preliminary on-sky commissioning results. In *Adaptive Optics Systems II*, volume 7736, page 773609. International Society for Optics and Photonics, July 2010. doi: 10.1117/12.858194. URL https://www.spiedigitallibrary.org/conference-proceedings-of-spie/7736/773609/First-light-AO-FLAO-system-for-LBT--final-integration/10.1117/12.858194.short.

O. Fauvarque, B. Neichel, T. Fusco, J.-F. Sauvage, and O. Girault. General formalism for Fourier-based wave front sensing. *Optica*, 3(12):1440–1452, Dec. 2016. ISSN 2334-2536. doi: 10.1364/OPTICA.3.001440. URL https://www.osapublishing.org/optica/abstract.cfm?uri=optica-3-12-1440.

O. Fauvarque, B. Neichel, T. Fusco, J.-F. Sauvage, and O. Girault. General formalism for Fourier-based wave front sensing: application to the pyramid wave front sensors. *Journal of Astronomical Telescopes, Instruments, and Systems*, 3(1): 019001, Mar. 2017. ISSN 2329-4124. doi: 10.1117/1.JATIS.3.1.019001. URL http://astronomicaltelescopes.spiedigitallibrary.org/article.aspx?doi=10.1117/1.JATIS.3.1.019001.

O. Fauvarque, P. Janin-Potiron, C. Correia, Y. Brûlé, B. Neichel, V. Chambouleyron, J.-F. Sauvage, and T. Fusco. Kernel formalism applied to Fourier-based wave-front sensing in presence of residual phases. *Journal of the Optical Society of America A*, 36:1241, July 2019. doi: 10.1364/JOSAA.36.001241. URL http://adsabs.harvard.edu/abs/2019JOSAA..36.1241F.

P. Feautrier and J.-L. Gach. Last performances improvement of the C-RED One camera using the 320x256 e-APD infrared Saphira detector. In A. Mérand, S. Sallum, and J. Sanchez-Bermudez, editors, *Optical and Infrared Interferometry and Imaging VIII*, page 90, Montréal, Canada, Aug. 2022. SPIE. ISBN 978-1-5106-5347-4 978-1-5106-5348-1. doi: 10.1117/12.2630860. URL https://www.spiedigitallibrary.org/conference-proceedings-of-spie/12183/2630860/Last-performances-improvement-of-the-C-RED-One-camera-using/10.1117/12.2630860.full.

P. Feautrier, J.-L. Gach, P. Balard, C. Guillaume, M. Downing, N. Hubin, E. Stadler, Y. Magnard, M. Skegg, M. Robbins, S. Denney, W. Suske, P. Jorden, P. Wheeler, P. Pool, R. Bell, D. Burt, I. Davies, J. Reyes, M. Meyer, D. Baade, M. Kasper, R. Arsenault, T. Fusco, and J. J. Diaz-Garcia. Characterization of OCam and CCD220: the fastest and most sensitive camera to date for AO wavefront sensing. In *Adaptive Optics Systems II*, volume 7736, pages 375–388. SPIE, July 2010. doi: 10.1117/12.856401. URL https://www.spiedigitallibrary.org/conference-proceedings-of-spie/7736/77360Z/Characterization-of-OCam-and-CCD220--the-fastest-and-most/10.1117/12.856401.full.

D. L. Fried. Statistics of a Geometric Representation of Wavefront Distortion. *Journal of the Optical Society of America*, 55(11):1427, Nov. 1965. ISSN 0030-3941. doi: 10.1364/JOSA.55.001427. URL https://opg.optica.org/abstract.cfm?URI=josa-55-11-1427.

D. L. Fried. Optical Resolution Through a Randomly Inhomogeneous Medium for Very Long and Very Short Exposures. *Journal of the Optical Society of America*, 56(10):1372, Oct. 1966. ISSN 0030-3941. doi: 10.1364/JOSA.56.001372. URL https://opg.optica.org/abstract.cfm?URI=josa-56-10-1372.

J.-L. Gach, P. Feautrier, P. Balard, C. Guillaume, and E. Stadler. OCAM2S: an integral shutter ultrafast and low noise wavefront sensor camera for laser

guide stars adaptive optics systems. In *Adaptive Optics Systems IV*, volume 9148, pages 459–468. SPIE, July 2014. doi: 10.1117/12.2054264. URL https://www.spiedigitallibrary.org/conference-proceedings-of-spie/9148/914819/OCAM2S--an-integral-shutter-ultrafast-and-low-noise-wavefront/10.1117/12.2054264.full.

E. Gendron and P. Lena. Astronomical adaptive optics. I. Modal control optimization. *Astronomy and Astrophysics*, 291:337–347, Nov. 1994. ISSN 0004-6361. URL https://ui.adsabs.harvard.edu/abs/1994A&A...291..337G.

R. A. Gonsalves. Phase Retrieval And Diversity In Adaptive Optics. *Optical Engineering*, 21(5):829–832, Oct. 1982. ISSN 0091-3286, 1560-2303. doi: 10.1117/12.7972989. URL https://www.spiedigitallibrary.org/journals/optical-engineering/volume-21/issue-5/215829/Phase-Retrieval-And-Diversity-In-Adaptive-Optics/10.1117/12.7972989.full. Publisher: SPIE.

O. Guyon. Extreme Adaptive Optics. *Annual Review of Astronomy and Astrophysics*, 56(1):315–355, 2018. doi: 10.1146/annurev-astro-081817-052000. URL https://doi.org/10.1146/annurev-astro-081817-052000.

T. Hardy, E. Zhao, and G. Burley. Instrument development with infrared APD arrays. In A. D. Holland and J. Beletic, editors, *X-Ray, Optical, and Infrared Detectors for Astronomy IX*, page 125, Online Only, United States, Dec. 2020. SPIE. ISBN 978-1-5106-3695-8 978-1-5106-3696-5. doi: 10.1117/12.2563068. URL https://www.spiedigitallibrary.org/conference-proceedings-of-spie/11454/2563068/Instrument-development-with-infrared-APD-arrays/10.1117/12.2563068.full.

I. Hughes and T. P. A. Hase. *Measurements and their uncertainties: a practical guide to modern error analysis*. New York : Oxford University Press, Oxford, 2010. ISBN 978-0-19-956632-7 978-0-19-956633-4. OCLC: ocn559786018.

L. Jocou, P. Rabou, T. Moulin, Y. Magnard, A. Hours, F. Pancher, S. Guieu, A. Carlotti, A. Delboulbé, M. Vérove, E. Stadler, D. Maurel, S. Rochat, F. Hénault, K. Dohlen, N. Thatte, B. Neichel, P. Vola, F. Clarke, D. Melotte, M. Tecza, and H. Schnetler. HARMONI at ELT: development of the high-contrast module. In D. Schmidt, L. Schreiber, and E. Vernet, editors, *Adaptive Optics Systems VIII*, page 171, Montréal, Canada, Aug. 2022. SPIE. ISBN 978-1-5106-5351-1 978-1-5106-5352-8. doi: 10.1117/12.2626984. URL https://www.spiedigitallibrary.org/conference-proceedings-of-spie/12185/2626984/HARMONI-at-ELT-development-of-the-high-contrast-module/10.1117/12.2626984.full.

M. Kasper, J.-L. Beuzit, C. Verinaud, P. Baudoz, A. Boccaletti, R. Gratton, C. Keller, F. Kerber, H. M. Schmid, N. Thatte, L. Venema, and N. Yaitskova. EPICS, the exoplanet imager for the E-ELT. In *1st AO4ELT conference - Adaptive Optics for Extremely Large Telescopes*, page 02009. EDP Sciences, 2010. ISBN 978-2-7598-0496-2 978-2-7598-0495-5. doi: 10.1051/ao4elt/201002009. URL https://ao4elt.edpsciences.org/articles/ao4elt/abs/2010/01/ao4elt_02009/ao4elt_02009.html.

M. Kasper, N. Cerpa Urra, P. Pathak, M. Bonse, J. Nousiainen, B. Engler, C. T. Heritier, J. Kammerer, S. Leveratto, C. Rajani, P. Bristow, M. Le Louarn, P.-Y. Madec, S. Ströbele, C. Verinaud, A. Glauser, S. P. Quanz, T. Helin, C. Keller, F. Snik, A. Boccaletti, G. Chauvin, D. Mouillet, C. Kulcsár, and H.-F. Raynaud. PCS — A Roadmap for Exoearth Imaging with the ELT. *Published in The Messenger vol. 182*, pp. 38-43:6 pages, 2021. ISSN 0722-6691. doi: 10.18727/0722-6691/5221. URL http://doi.eso.org/10.18727/0722-6691/5221.

A. Kolmogorov. The Local Structure of Turbulence in Incompressible Viscous Fluid for Very Large Reynolds' Numbers. *Akademiia Nauk SSSR Doklady*, 30: 301–305, Jan. 1941. ISSN 0002-3264. URL https://ui.adsabs.harvard.edu/abs/1941DoSSR..30..301K.

V. Korkiakoski, C. Vérinaud, and M. L. Louarn. Improving the performance of a pyramid wavefront sensor with modal sensitivity compensation. *Applied Optics*, 47(1):79, Jan. 2008. ISSN 0003-6935, 1539-4522. doi: 10.1364/AO.47.000079. URL https://opg.optica.org/abstract.cfm?URI=ao-47-1-79.

K. Kouwenhoven, I. Elwakil, J. v. Wingerden, V. Murugesan, D. J. Thoen, J. J. A. Baselmans, and P. J. d. Visser. Model and Measurements of an Optical Stack for Broadband Visible to Near-Infrared Absorption in TiN MKIDs. *Journal of Low Temperature Physics*, July 2022. ISSN 0022-2291, 1573-7357. doi: 10.1007/s10909-022-02774-0. URL https://link.springer.com/10.1007/s10909-022-02774-0.

C. Kulcsár, H.-F. Raynaud, C. Petit, J.-M. Conan, and P. V. D. Lesegno. Optimal control, observers and integrators in adaptive optics. *Optics Express*, 14(17): 7464, Aug. 2006. ISSN 1094-4087. doi: 10.1364/OE.14.007464. URL https://opg.optica.org/oe/abstract.cfm?uri=oe-14-17-7464.

H. Ltaief, D. Gratadour, A. Charara, and E. Gendron. Adaptive Optics Simulation for the World's Largest Telescope on Multicore Architectures with Multiple GPUs. In *Proceedings of the Platform for Advanced Scientific Computing Conference*, pages 1–12, Lausanne Switzerland, June 2016. ACM. ISBN 978-1-4503-4126-4. doi: 10.1145/2929908.2929920. URL https://dl.acm.org/doi/10.1145/2929908.2929920.

A. Magniez, L. Bardou, T. J. Morris, and K. O'Brien. MKID: an energy sensitive superconducting detector for the next generation of XAO systems. In D. Schmidt, L. Schreiber, and E. Vernet, editors, *Adaptive Optics Systems VIII*, page 94, Montréal, Canada, Aug. 2022. SPIE. ISBN 978-1-5106-5351-1 978-1-5106-5352-8. doi: 10.1117/12.2627026. URL https://www.spiedigitallibrary.org/conference-proceedings-of-spie/12185/2627026/MKID--an-energy-sensitive-superconducting-detector-for-the-next/10.1117/12.2627026.full.

V. N. Mahajan. Strehl ratio for primary aberrations: some analytical results for circular and annular pupils. *Journal of the Optical Society of America*, 72(9): 1258, Sept. 1982. ISSN 0030-3941. doi: 10.1364/JOSA.72.001258. URL https://opg.optica.org/abstract.cfm?URI=josa-72-9-1258.

B. Mazin, J. Bailey, J. Bartlett, C. Bockstiegel, B. Bumble, G. Coiffard, T. Currie, M. Daal, K. Davis, R. Dodkins, N. Fruitwala, N. Jovanovic, I. Lipartito, J. Lozi, J. Males, D. Mawet, S. Meeker, K. O'Brien, M. Rich, J. Smith, S. Steiger, N. Swimmer, A. Walter, N. Zobrist, and J. Zmuidzinas. MKIDs in the 2020s. *Bulletin of the AAS*, 51(7), Sept. 2019. URL https://baas.aas.org/pub/2020n7i017/release/1.

B. A. Mazin, P. K. Day, H. G. LeDuc, A. Vayonakis, and J. Zmuidzinas. Superconducting kinetic inductance photon detectors. In *Highly Innovative Space Telescope Concepts*, volume 4849, pages 283–293. International Society for Optics and Photonics, Dec. 2002. doi: 10.1117/12.460456. URL https://www.spiedigitallibrary.org/conference-proceedings-of-spie/4849/0000/Superconducting-kinetic-inductance-photon-detectors/10.1117/12.460456.short.

B. A. Mazin, B. Bumble, S. R. Meeker, K. O'Brien, S. McHugh, and E. Langman. A superconducting focal plane array for ultraviolet, optical, and near-infrared astrophysics. *Optics Express*, 20(2):1503, Jan. 2012. ISSN 1094-4087. doi: 10.1364/OE.20.001503. URL https://opg.optica.org/oe/abstract.cfm?uri=oe-20-2-1503.

B. A. Mazin, S. R. Meeker, M. J. Strader, B. Bumble, K. O'Brien, P. Szypryt, D. Marsden, J. C. van Eyken, G. E. Duggan, G. Ulbricht, C. Stoughton, and M. Johnson. ARCONS: A 2024 Pixel Optical through Near-IR Cryogenic Imaging Spectrophotometer. *Astronomical Society of the Pacific*, 125(933):1348–1361, Nov. 2013. ISSN 00046280, 15383873. doi: 10.1086/674013. URL http://arxiv.org/abs/1306.4674.

S. McHugh, B. A. Mazin, B. Serfass, S. Meeker, K. O'Brien, R. Duan, R. Raffanti, and D. Werthimer. A readout for large arrays of microwave kinetic inductance detectors. *Review of Scientific Instruments*, 83:044702–044702, Apr. 2012. ISSN 0034-6748. doi: 10.1063/1.3700812. URL https://ui.adsabs.harvard.edu/abs/2012RScI...83d4702M.

K. M. Morzinski, M. Montoya, C. Fellows, O. Durney, J. Ford, G. West, A. Gardner, A. Vaz, N. Anugu, E. Mailhot, J. Carlson, L. Harrison, F. Gacon, E. Downey, P. M. Hinz, T. Jones, J. Patience, S. Sivanandam, S. Chen, M. P. Lamb, A. Butko, S. Liu, T. Hardy, and B. Jannuzi. Development and status of MAPS, the MMT AO exoPlanet characterization system. In D. Schmidt, L. Schreiber, and E. Vernet, editors, *Adaptive Optics Systems VII*, page 61, Online Only, United States, Dec. 2020. SPIE. ISBN 978-1-5106-3683-5 978-1-5106-3684-2. doi: 10.1117/12.2563178. URL https://www.spiedigitallibrary.org/conference-proceedings-of-spie/11448/2563178/Development-and-status-of-MAPS-the-MMT-AO-exoPlanet-characterization/10.1117/12.2563178.full.

A. Müller, M. Keppler, T. Henning, M. Samland, G. Chauvin, H. Beust, A.-L. Maire, K. Molaverdikhani, R. Van Boekel, M. Benisty, A. Boccaletti, M. Bonnefoy, F. Cantalloube, B. Charnay, J.-L. Baudino, M. Gennaro, Z. C. Long, A. Cheetham, S. Desidera, M. Feldt, T. Fusco, J. Girard, R. Gratton, J. Hagelberg, M. Janson, A.-M. Lagrange, M. Langlois, C. Lazzoni, R. Ligi, F. Ménard, D. Mesa, M. Meyer, P. Mollière, C. Mordasini, T. Moulin, A. Pavlov, N. Pawellek, S. P. Quanz, J. Ramos, D. Rouan, E. Sissa, E. Stadler, A. Vigan, Z. Wahhaj, L. Weber, and A. Zurlo. Orbital and atmospheric characterization of the planet within the gap of the PDS 70 transition disk. *Astronomy & Astrophysics*, 617: L2, Sept. 2018. ISSN 0004-6361, 1432-0746. doi: 10.1051/0004-6361/201833584. URL https://www.aanda.org/10.1051/0004-6361/201833584.

R. J. Noll. Zernike polynomials and atmospheric turbulence*. *Journal of the*

Optical Society of America, 66(3):207, Mar. 1976. ISSN 0030-3941. doi: 10.1364/JOSA.66.000207. URL https://www.osapublishing.org/abstract.cfm?URI=josa-66-3-207.

Numpy Community. NumPy Reference — NumPy v1.17 Manual, 2020. URL https://numpy.org/doc/1.17/reference/index.html.

S. Oberti, C. Correia, T. Fusco, B. Neichel, and P. Guiraud. Super-resolution wavefront reconstruction. *Astronomy & Astrophysics*, 667:A48, Nov. 2022. ISSN 0004-6361, 1432-0746. doi: 10.1051/0004-6361/202243954. URL http://arxiv.org/abs/2208.12052. arXiv:2208.12052 [astro-ph, physics:physics].

D. Owton, I. Baker, C. Maxey, A. Malik, J. Ash, J. Gordon, R. Mistry, and M. Hicks. Current infra-red developments within Leonardo. In *Infrared Sensors, Devices, and Applications XIII*, volume 12687, pages 47–64. SPIE, Oct. 2023. doi: 10.1117/12.2677446. URL https://www.spiedigitallibrary.org/conference-proceedings-of-spie/12687/1268706/Current-infra-red-developments-within-Leonardo/10.1117/12.2677446.full.

E. G. P. O'Connor, A. Shearer, and K. O'Brien. Energy-sensitive detectors for astronomy: Past, present and future. *New Astronomy Reviews*, 87:101526, Dec. 2019. ISSN 1387-6473. doi: 10.1016/j.newar.2020.101526. URL http://www.sciencedirect.com/science/article/pii/S1387647320300038.

R. Penrose. On best approximate solutions of linear matrix equations. *Mathematical Proceedings of the Cambridge Philosophical Society*, 52(1):17–19, Jan. 1956. ISSN 0305-0041, 1469-8064. doi: 10.1017/S0305004100030929. URL https://www.cambridge.org/core/product/identifier/S0305004100030929/type/journal_article.

E. Pinna, G. Agapito, F. Quirós-Pacheco, J. Antichi, L. Carbonaro, R. Briguglio, M. Bonaglia, A. Riccardi, A. Puglisi, V. Biliotti, C. Arcidiacono, M. Xompero, G. D. Rico, A. Valentini, A. Bouchez, F. Santoro, G. Trancho, and S. Esposito.

Design and numerical simulations of the GMT Natural Guide star WFS. In *Adaptive Optics Systems IV*, volume 9148, pages 898–912. SPIE, Aug. 2014. doi: 10.1117/12.2057059. URL https://www.spiedigitallibrary.org/conference-proceedings-of-spie/9148/91482M/Design-and-numerical-simulations-of-the-GMT-Natural-Guide-star/10.1117/12.2057059.full.

C. Plantet, G. Agapito, C. Giordano, C. Z. Bond, S. Esposito, P. L. Wizinowich, and M. Taheri. Keck II adaptive optics upgrade: simulations of the near-infrared pyramid sensor. In D. Schmidt, L. Schreiber, and L. M. Close, editors, *Adaptive Optics Systems VI*, page 115, Austin, United States, July 2018. SPIE. ISBN 978-1-5106-1959-3 978-1-5106-1960-9. doi: 10.1117/12.2313190. URL https://www.spiedigitallibrary.org/conference-proceedings-of-spie/10703/2313190/Keck-II-adaptive-optics-upgrade--simulations-of-the-near/10.1117/12.2313190.full.

B. C. Platt and R. Shack. History and Principles of Shack-Hartmann Wavefront Sensing. *Journal of Refractive Surgery*, 17(5), Sept. 2001. ISSN 1081-597X. doi: 10.3928/1081-597X-20010901-13. URL https://journals.healio.com/doi/10.3928/1081-597X-20010901-13.

R. Ragazzoni. Pupil plane wavefront sensing with an oscillating prism. *Journal of Modern Optics*, 43(2):289–293, Feb. 1996. ISSN 0950-0340, 1362-3044. doi: 10.1080/09500349608232742. URL http://www.tandfonline.com/doi/abs/10.1080/09500349608232742.

R. Ragazzoni, E. Diolaiti, and E. Vernet. A pyramid wavefront sensor with no dynamic modulation. *Optics Communications*, 208(1):51–60, July 2002. ISSN 0030-4018. doi: 10.1016/S0030-4018(02)01580-8.

A. Reeves. Soapy: an adaptive optics simulation written purely in Python for rapid concept development. In *Adaptive Optics Systems V*, volume 9909, pages 2173–2183. SPIE, July 2016. doi: 10.1117/12.2232438. URL https://www.spiedigitallibrary.org/conference-proceedings-of-spie/

9909/99097F/Soapy--an-adaptive-optics-simulation-written-purely-in-Python/10.1117/12.2232438.full.

M. Robbins and B. Hadwen. The noise performance of electron multiplying charge-coupled devices. *IEEE Transactions on Electron Devices*, 50(5):1227–1232, May 2003. ISSN 0018-9383. doi: 10.1109/TED.2003.813462. URL http://ieeexplore.ieee.org/document/1210766/.

F. Roddier. V The Effects of Atmospheric Turbulence in Optical Astronomy. In *Progress in Optics*, volume 19, pages 281–376. Elsevier, 1981. ISBN 978-0-444-85444-5. doi: 10.1016/S0079-6638(08)70204-X. URL https://linkinghub.elsevier.com/retrieve/pii/S007966380870204X.

F. Roddier, editor. *Adaptive optics in astronomy*. Cambridge University Press, Cambridge, U.K. ; New York, 1999. ISBN 978-0-521-55375-9.

J.-F. Sauvage, T. Fusco, C. Petit, A. Costille, D. Mouillet, J.-L. Beuzit, K. Dohlen, M. Kasper, M. Suarez, C. Soenke, A. Baruffolo, B. Salasnich, S. Rochat, E. Fedrigo, P. Baudoz, E. Hugot, A. Sevin, D. Perret, F. Wildi, M. Downing, P. Feautrier, P. Puget, A. Vigan, J. O'Neal, J. Girard, D. Mawet, H. M. Schmid, and R. Roelfsema. SAXO: the extreme adaptive optics system of SPHERE (I) system overview and global laboratory performance. *Journal of Astronomical Telescopes, Instruments, and Systems*, 2(2):025003, May 2016. ISSN 2329-4124. doi: 10.1117/1.JATIS.2.2.025003. URL http://astronomicaltelescopes.spiedigitallibrary.org/article.aspx?doi=10.1117/1.JATIS.2.2.025003.

J. D. Schmidt. *Numerical Simulation of Optical Wave Propagation with Examples in MATLAB*. SPIE, July 2010. ISBN 978-0-8194-8327-0. doi: 10.1117/3.866274. URL https://spiedigitallibrary.org/ebooks/PM/Numerical-Simulation-of-Optical-Wave-Propagation-with-Examples-in-MATLAB/eISBN-9780819483270/10.1117/3.866274.

N. Schwartz, J.-F. Sauvage, C. Correia, C. Petit, F. Quiros-Pacheco, T. Fusco, K. Dohlen, K. El Hadi, N. Thatte, F. Clarke, J. Paufique, and J. Vernet. Sensing and control of segmented mirrors with a pyramid wavefront sensor in the presence of spiders. In *Proceedings of the Adaptive Optics for Extremely Large Telescopes 5*. Instituto de Astrofísica de Canarias (IAC), 2017. doi: 10.26698/AO4ELT5.0015. URL http://research.iac.es/congreso/AO4ELT5/pages/proceeding0015.html.

N. Schwartz, J.-F. Sauvage, E. Renault, C. Correia, B. Neichel, T. Fusco, K. Dohlen, K. E. Hadi, C. Petit, E. Choquet, V. Chambouleyron, J. Paufique, F. Clarke, N. Thatte, and I. Bryson. Design of the HARMONI Pyramid WFS module. In *Proceedings of the Adaptive Optics for Extremely Large Telescopes 6*, Québec city, Canada, 2020. doi: 10.48550/ARXIV.2003.07228. URL https://arxiv.org/abs/2003.07228.

S. Seager and R. Dotson. *Exoplanets*. The University of Arizona space science series. University of Arizona press, Tucson, 2010. ISBN 978-0-8165-2945-2.

V. I. Tatarskii. *The effects of the turbulent atmosphere on wave propagation*. Jan. 1971. URL https://ui.adsabs.harvard.edu/abs/1971etaw.book.....T.

A. Tozzi, P. Stefanini, E. Pinna, and S. Esposito. The double pyramid wavefront sensor for LBT. In *Adaptive Optics Systems*, volume 7015, pages 1454–1462. SPIE, July 2008. doi: 10.1117/12.789311. URL https://www.spiedigitallibrary.org/conference-proceedings-of-spie/7015/701558/The-double-pyramid-wavefront-sensor-for-LBT/10.1117/12.789311.full.

F. Vidal, C. Goulas, R. Galicher, A. Boccaletti, F. Cantalloube, E. Gendron, A. Sevin, F. Ferreira, G. Chauvin, M. Langlois, and J. Milli. SAXO+ upgrade: system choices & numerical simulations. In D. Schmidt, L. Schreiber, and E. Vernet, editors, *Adaptive Optics Systems VIII*, page 164, Montréal, Canada, Aug. 2022. SPIE. ISBN 978-1-5106-5351-1 978-1-5106-5352-8.

doi: 10.1117/12.2629325. URL https://www.spiedigitallibrary.org/conference-proceedings-of-spie/12185/2629325/SAXO-upgrade-system-choices--numerical-simulations/10.1117/12.2629325.full.

C. Vérinaud. On the nature of the measurements provided by a pyramid wave-front sensor. *Optics Communications*, 233(1):27–38, Mar. 2004. ISSN 0030-4018. doi: 10.1016/j.optcom.2004.01.038. URL http://www.sciencedirect.com/science/article/pii/S0030401804000628.

A. B. Walter. *MEC: The MKID Exoplanet Camera for High Speed Focal Plane Control at the Subaru Telescope*. PhD thesis, UC Santa Barbara, 2019. URL https://escholarship.org/uc/item/73t506w9.

A. B. Walter, N. Fruitwala, S. Steiger, J. I. Bailey, N. Zobrist, N. Swimmer, I. Lipartito, J. P. Smith, S. R. Meeker, C. Bockstiegel, G. Coiffard, R. Dodkins, P. Szypryt, K. K. Davis, M. Daal, B. Bumble, G. Collura, O. Guyon, J. Lozi, S. Vievard, N. Jovanovic, F. Martinache, T. Currie, and B. A. Mazin. The MKID Exoplanet Camera for Subaru SCExAO. *Publications of the Astronomical Society of the Pacific*, 132(1018):125005, Nov. 2020. ISSN 1538-3873. doi: 10.1088/1538-3873/abc60f. URL https://dx.doi.org/10.1088/1538-3873/abc60f.

Wells, D.C, Greisen, E. W., and Harten, R. H. FITS - a Flexible Image Transport System. *Astronomy and Astrophysics Supplement*, 44:363, 1981.

v. F. Zernike. Beugungstheorie des schneidenver-fahrens und seiner verbesserten form, der phasenkontrastmethode. *Physica*, 1(7):689–704, May 1934. ISSN 0031-8914. doi: 10.1016/S0031-8914(34)80259-5. URL http://www.sciencedirect.com/science/article/pii/S0031891434802595.

A. Ziad, M. Schöck, G. A. Chanan, M. Troy, R. Dekany, B. F. Lane, J. Borgnino, and F. Martin. Comparison of measurements of the outer scale of turbulence by three different techniques. *Applied Optics*, 43(11):2316, Apr. 2004. ISSN 0003-

6935, 1539-4522. doi: 10.1364/AO.43.002316. URL https://opg.optica.org/abstract.cfm?URI=ao-43-11-2316.

N. Zobrist, W. H. Clay, G. Coiffard, M. Daal, N. Swimmer, P. Day, and B. A. Mazin. Membraneless Phonon Trapping and Resolution Enhancement in Optical Microwave Kinetic Inductance Detectors. *Physical Review Letters*, 129(1):017701, July 2022. ISSN 0031-9007, 1079-7114. doi: 10.1103/PhysRevLett.129.017701. URL https://link.aps.org/doi/10.1103/PhysRevLett.129.017701.